Photoinduced Electron and Proton Transfer with Ruthenium Complexes and Organic Donors and Acceptors

Inauguraldissertation

zur Erlangung der Würde eines Doktors der Philosophie

vorgelegt der
Philosophisch-Naturwissenschaftlichen Fakultät
der Universität Basel

von

Andrea Pannwitz

aus Jena, Deutschland

Basel, 2017

Genehmigt von der Philosophisch-Naturwissenschaftlichen Fakultät auf Antrag von

Fakultätsverantwortlicher/ Dissertationsleiter: Prof. Dr. Oliver S. Wenger

Korreferentin: Prof. Dr. Katja Heinze

Basel, den 23.05.2017

_____

Prof. Dr. Martin Spiess

Learn and create. Transform the future.

T. J. Young

Contents

Abstract

Proton-coupled electron transfer (PCET) plays a crucial role in photosynthesis and catalytic conversions such as water oxidation and carbon dioxide reduction. It can formally be split into proton and electron transfer. In photosynthesis, light is used as principal energy resource, which is also desirable for artificial conversions. Therefore, PCET and individual proton and electron transfers from the long-living triplet excited state of ruthenium polyimine complexes were investigated in this thesis.

In the first project, photoinduced PCET from the excited state of $[Ru(bpy)_2(pyimH)]^{2+}$ (bpy = 2,2'-bipyridine, pyimH = (2-pyridyl)imidazole) was investigated with electrochemical and time-resolved spectroscopic techniques. Depending on the pH, simple ET or PCET to a suitable organic substrate is favored. Simple excited state ET is facilitated significantly upon deprotonation of the ruthenium photosensitizer. The reducing power of this type of complex was further tuned by electron donating and electron withdrawing substituents on the bpy-spectator-ligands. Formal hydrogen atom donation is facilitated by approximately 50 kcal mol^{-1} in the photochemically generated ^{3}MLCT, making these complexes strong formal hydrogen atom donors, even when compared to metal hydride complexes.

In the second project, a molecular triad was investigated which is inspired by photosystem II. This triad combines long-range photoinduced charge transfer with two PCETs. The investigated donor-photosensitizer-acceptor assembly is based on a phenol as combined electron and proton donor, a $[Ru(bpy)_3]^{2+}$-type photosensitizer and a 4,4'-bipyridinium proton and electron acceptor. The photochemically generated radicals are separated by 20 Å. They are formed via two PCETs which mimics enzymatic long-range charge transfer more closely than any previously reported molecular model system.

In the third project, the influence of a hydrogen bonded carboxylate on the luminescent excited state of acidic $[Ru(bpy)_2(biimH_2)]^{2+}$ (biimH$_2$ = 2,2'-biimidazole) type complexes was examined. Luminescence of monocrystalline samples was characterized by DFT calculations and monitored in the solid state at variable temperature and pressure. A pressure-induced red-shift in luminescence was observed in complexes with electron donating *tert*-butyl substituents on the bpy ligands whereas the more acidic complex with CF$_3$-substituents showed only small pressure dependent luminescence. The origin of the difference in luminescence is either due to pressure induced proton transfer or secondary coordination sphere interactions via the hydrogen bonds.

1   Introduction

1.1   Motivation

Nowadays, main energy resources are based on fossil fuels, such as coal, natural gas and raw oil. The heat that is generated by burning or combustion of fossil fuels is for example used for transportation, adjusting temperature in household areas, manufacturing, construction and generation of electricity. This concept is functioning for now, but unfortunately it is accompanied by environmental pollution due to the emission of detrimental gases such as NO_x, and SO_2 and the greenhouse gas CO_2. Furthermore, energy demand will increase in the next decades because world's population is growing rapidly, reaching 9 billion in 2050,[1] and harvesting fossil fuels gets more and more difficult and expensive, since mankind has to reach out for the last resources available. Thus, new harvesting methods such as fracking, raw oil extraction from oil sand and harvesting from deep sea reservoirs have to be considered. The environmental impact for these new methods, cannot be estimated yet. It is therefore important to reduce the average energy consumption per person and establish alternative energy resources. This long-term goal is supported by political agendas and guidelines on the national and international level.[1] A changeover to alternative energy resources is desired by the United Nations.[2] Examples for national programs are the Swiss 2000-Watt program,[3] and the Energiewende in Germany.[4]

Among others, one alternative energy resource is sun light. Its incident energy on the earth exceeds human's energy demands by orders of magnitude.[5] In order to benefit from it, nature can be used as an inspiration. Plants and some bacteria absorb light energy to convert CO_2 into hydrocarbons via photosynthesis. Mankind's technologies for light energy conversion are based on solar heat and photovoltaics. These technologies are established, but lack one important feature: the converted energy is stored by secondary conversions, limiting the yield of the entire processes. To solve this problem, it would be beneficial to convert solar energy directly into storable energy carriers. One could imagine to produce hydrocarbons from CO_2 and hydrogen from water.[6]

Such conversions are performed by photosynthetic organisms and the mechanism for their valorization of light energy are briefly described in the next section.

1.2 Light Energy Conversion in Photosynthesis

Photosynthesis takes place in autotrophic organisms, such as plants, algae and cyanobacteria. They absorb energy from sunlight to produce the cellular reducing agents ATP and NADPH, which are further used for the reduction of atmospheric carbon dioxide to a variety of hydrocarbons, such as carbohydrates and fatty acids. The electrons needed for this process are abstracted from water or other reductants like hydrogen sulfide. The light-driven net redox process is summarized in the following equation:

$$nCO_2 + nH_2O \rightarrow [CH_2O]_n + nO_2 \qquad (1\text{-}1)$$

The mechanism of this reaction was profoundly investigated in the past decades. Advances in protein crystallography, time resolved spectroscopy and high resolution magnetic spectroscopy crucially contributed to the understanding of natural photosynthesis and paved the way for applying its concepts in artificial systems. Natural photosynthesis comprises of light-dependent and light-independent reactions. In the light-dependent reaction, water is oxidized to provide electrons for the production of NADPH and ATP. In turn, the latter are consumed in the light-independent reaction, i.e. the Calvin-cycle, to reduce CO_2 to hydrocarbons such as glucose.[7]
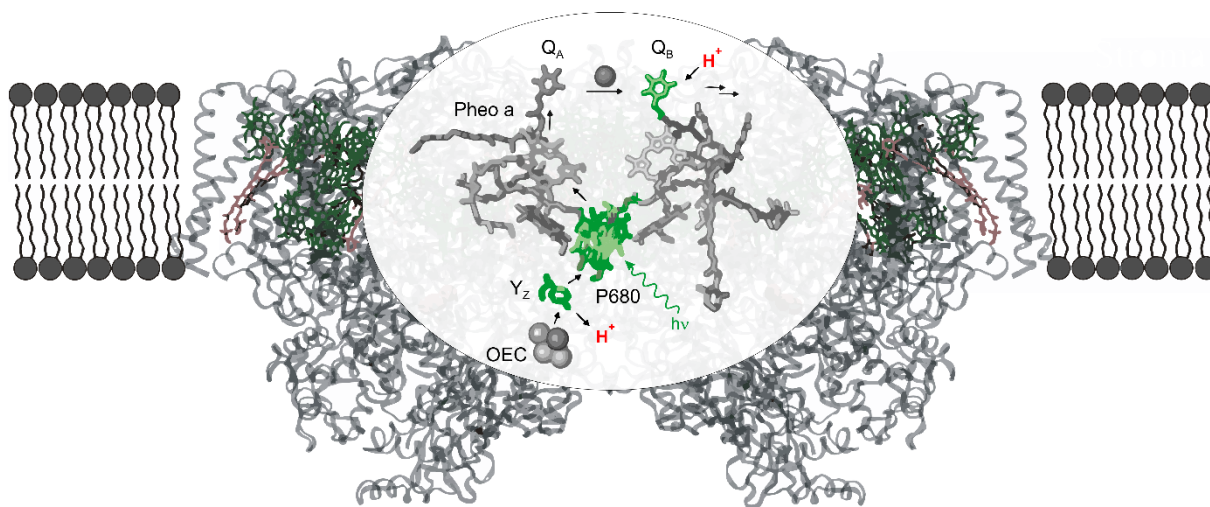
Figure 1-1 Electron transfer chain in photosystem II (PS II) embedded in the thylakoid membrane, with water oxidizing complex (OEC), tyrosine Z (Y_Z), the light-absorbing chlorophyll pair P680, Pheophytin a (Pheo a), plastoquinone A (Q_A), plastoquinone B (Q_B). (picture is adapted from reference [8])

The light-involving reactions are important for the context of this thesis and summarized in the following. They mainly take place in the thylakoid membrane that separates the oxidation and reduction compartment from one another. Electrons are transferred across the membrane via the protein complexes photosystem I and II (PS I, PS II). The central unit of each of these

proteins is a chlorophyll-based dimeric chromophore. In PS I, the chromophore absorbs at 700 nm and is called P700, and in PS II it absorbs at 680 nm and is called P680. Both chromophores can be excited either by absorption of incident light or via energy transfer from light-harvesting chromophores in the protein complex. Upon excitation of P700 and P680, charge separated states are achieved. Charge recombination is in direct competition to long-rang electron transfer across the membrane. Charge recombination is inhibited by subsequent transport of the electrons from one acceptor to the next, away from the chromophores. The conditions for these subsequent electron transfers are a suitable spatial arrangement of donors and acceptors and matching redox potentials, so that each electron transfer is energetically downhill.
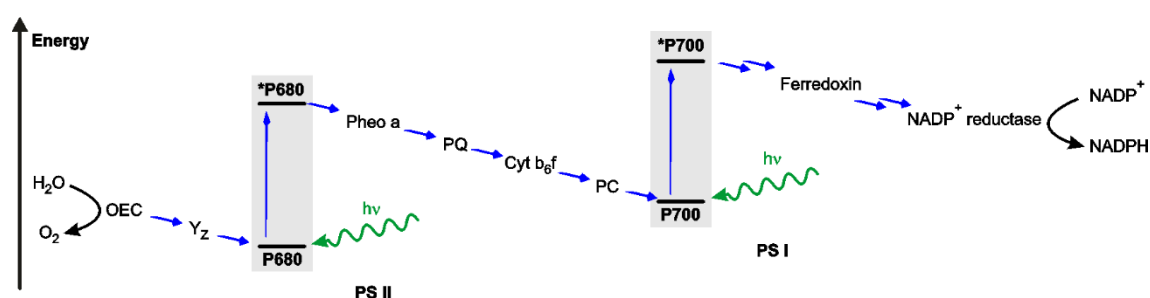
Figure 1-2 Simplified Z-scheme for plant photosynthesis with water oxidizing complex (OEC), tyrosine Z (Y_Z), the chromophores P680 and P700, Pheophytin a (Pheo a), plastoquinones (PQ), cytochrome b_6f (Cyt b_6f) and plastocyanin (PC).

The entire cascade of plant-photosynthesis is schematically summarized in the so-called Z-scheme in Figure 1-2. The electrons originate from water, which is oxidized to oxygen by the water oxidizing complex (OEC) in PS II, as depicted in Figure 1-1. The OEC donates electrons to the nearby tyrosine Z (Y_Z) which donates electrons to the oxidized P680. Oxidation of Y_Z is coupled to deprotonation by a nearby histidine. Photoexcited P680 is oxidized by the nearby Pheophytin a (Pheo a) that subsequently reduces the plastoquinones (PQ), first plastoquinone A (Q_A), which in turn reduces plastoquinone B (Q_B). After twofold reduction and protonation, Q_B diffuses into the thylakoid membrane and then further to cytochrome b_6f (Cyt b_6f). This in turn reduces plastocyanin (PC) that reduces the central chromophore in PS I, P700 after photoexcitation. P700 is oxidized by PS I-associated acceptors that deliver electrons to ferredoxin which in turn reduces $NADP^+$-reductase for the reduction of $NADP^+$ to NADPH.

For water oxidation catalysis, four holes per turn-over need to be accumulated on the OEC. Hence, four photons need to be absorbed by the central P680 and its antenna-chromophores, because one electron-hole-pair is generated per absorbed photon. This is in agreement with the Kok-cycle and the respective experiment that shows that one equivalent of oxygen is produced

after four pulsed excitations of PS II.[9] Accumulation of holes is competing with charge recombination at the chromophore. The entire process induces a proton gradient across the membrane and generates the so-called proton-motive force that is used to run ATPase to generate ATP from ADP.[7]
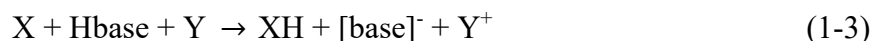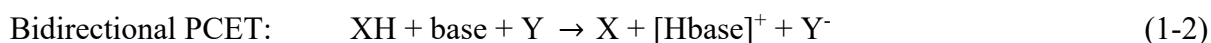
In summary, the light-dependent reaction of photosynthesis is based on excited state redox chemistry, long range charge separation and proton-coupled electron transfer (PCET), which are key subjects of this thesis.

1.3 Proton-Coupled Electron Transfer (PCET)

The major part of this thesis deals with proton coupled electron transfer (PCET). Relevant definitions, formulas and electrochemical methods are therefore summarized in this section.

1.3.1 Definitions

Uptake and release of electrons that involve the transfer of protons are called proton-coupled electron transfer (PCET) reactions. A combined proton and electron donor releases a proton upon oxidation. Similarly, a combined proton and electron acceptor is protonated upon reduction. The overall PCET can formally be split into acid-base chemistry (proton transfer, PT) and redox chemistry (electron transfer, ET). PCET can take place in a single reaction step, so-called concerted proton-coupled electron transfer (CPET), or in a stepwise fashion via a sequence of PT followed by ET, or vice versa. Depending on the relative direction of proton and electron transfer, PCET is defined by bidirectional or unidirectional. For bidirectional transfer of a PCET reagent XH, the proton is transferred to a base, whereas the electron is transferred to an electron acceptor Y, yielding X (eq. 1-2), or vice versa: A PCET reagent X takes up a proton from an acid (Hbase) and the electron from an electron donor (Y) yielding XH (eq. 1-3).

Bidirectional PCET: $\quad XH + base + Y \rightarrow X + [Hbase]^+ + Y^-$ (1-2)

$$X + Hbase + Y \rightarrow XH + [base]^- + Y^+ \qquad (1-3)$$

In unidirectional PCET, the electron donor is also the proton donor and electron and proton are adiabatically transferred to an acceptor that acts as electron acceptor and base (eq. 1-4).

Unidirectional PCET/formal HAT:

$$XH + Y \rightarrow X + YH \qquad (1-4)$$

One electron and one proton formally sum up to a hydrogen atom. When proton and electron originate from the same orbital and are taken up into the same orbital, this special PCET is called hydrogen atom transfer (HAT). Usually, unidirectional PCET is a formal HAT.[10,11]

The most relevant scope of PCET reactions involve the transfer of *one* electron and *one* proton. In a broader view, e.g. two electrons and one proton can be transferred via PCET mechanism. The resulting (formal) hydride transfer is important for a variety of reactions but in the focus of this thesis.[12]

1.3.2 Thermochemistry of PCET

Based on Hess's law, the overall PCET or CPET can be split into individual PT and ET. The formal reaction sequences of PT and ET can be summarized in a so-called square-scheme, as shown in Scheme 1-1 for unidirectional PCET from proton-electron donor (XH) to proton-electron acceptor (Y).
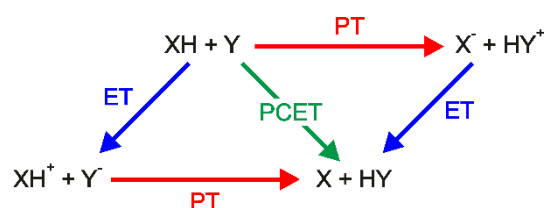
Scheme 1-1 Thermochemical square-scheme for unidirectional PCET from donor XH to acceptor Y with possible individual proton transfer (PT) and electron transfer (ET).

The overall driving force for a PCET reaction (ΔG_{PCET}) is the sum over the driving force for a formal sequence of PT (ΔG_{PT}) and ET (ΔG_{ET}) (eq. 1-5). For this calculation, it is important to follow one route in the square-scheme in Scheme 1-1.

$$\Delta G_{PCET} = \Delta G_{PT} + \Delta G_{ET} \tag{1-5}$$

The driving force for PT (ΔG_{PT}) is calculated with the acidity constant (pK_a) of proton donor and acceptor:

$$\Delta G_{PT} = 0.059 \text{ eV} \left[pK_a(\text{donor})\text{-}pK_a(\text{acceptor})\right] \tag{1-6}$$

Under standard conditions, the driving force for ET ($\Delta G°_{ET}$) is calculated with the amount of electron equivalents (n), Faraday's constant (F) and the standard redox potential (E°) of electron donor and acceptor by the following equation:

$$\Delta G°_{ET} = n\, F\, [E°(\text{donor})\text{-}E°(\text{acceptor})] \tag{1-7}$$

Equation 1-8 additionally takes into account the dielectric constant of the solvent (ε) and the center-to-center distance (a) of the solvated donor and acceptor molecule.[13] The elementary charge e accounts for the unit transition from V to eV and $e^2/\varepsilon a$ ranges usually between zero and 0.15 eV.[13]

$$\Delta G_{ET} = [E°(\text{donor})\text{-}E°(\text{acceptor})]e - e^2/\varepsilon a \tag{1-8}$$

1.3.3 **Pourbaix and Potential-pKa Diagrams**

Redox chemistry is experimentally evaluated by electrochemical methods, such as cyclic voltammetry. An exemplary reaction is the oxidation of an electron-proton donor XH_m donating m protons and z electrons as in the following equation:

$$XH_m \rightarrow X + mH^+ + z\ e^- \tag{1-9}$$

The redox potential E depends on the standard redox potential ($E°$), gas constant (R), Faraday constant (F), temperature (T), number of electrons (z) and ratio of products and reactants as rationalized by the Nernst-equation (eq. 1-10).

$$E = E° + \frac{RT}{zF} \ln\left(\frac{[X^{+(z-m)}]\ [H^+]^m}{[XH_m]} \right) \tag{1-10}$$

The pre-factor $\frac{RT}{F}$ is constant at 25 °C and with transformation of natural to decadic logarithm the pre-factor is $\frac{0.059\ eV}{z}$. At the half wave potential ($E_{1/2}$) the concentration of oxidized and reduced species is equal, yielding the following equation:

$$E_{1/2} = E° + \frac{0.059\ eV}{z} \lg\left([H^+]^m \right) \tag{1-11}$$

In water, eq. 1-11 can be converted into the pH-dependent Pourbaix expression into following equation:

$$E_{1/2} = E° - 0.059\ eV \frac{m}{z} pH \tag{1-12}$$

That means, in the pH range, where redox processes are proton coupled, the redox potential changes linearly as a function of pH with a slope of -0.059 eV multiplied by the ratio of number of protons (m) and number of electrons (z). In the pH range where no pH dependence is observed, product and reactant have the same protonation grade, either protonated or not protonated. The intersections of pH dependent and pH independent redox potential reflect the pKa values of the reduced and oxidized forms.

For a simple one-electron-one-proton process the pH dependence of redox potential is presented schematically in Scheme 1-2. In organic solvents, a dependence on pH is difficult to rationalize. Instead, the same relation applies for the pK_a of the equimolarly added (conjugated) acid.[14]
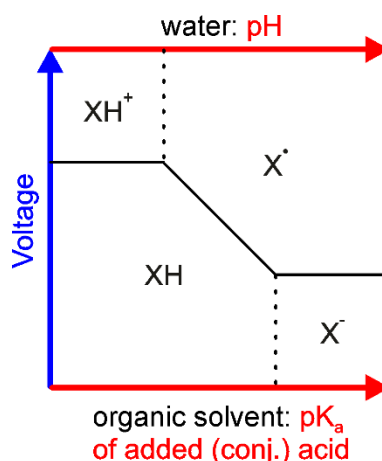
Scheme 1-2 Pourbaix and potential-pKa diagram of a compound XH in a one-electron-one-proton redox process.

1.3.4 Formal Bond Dissociation Free Energies (BDFEs) for X-H bonds

A very useful method to characterize a proton-electron donor in its PCET reactivity is to calculate the formal bond dissociation free energy (BDFE) of the X-H bond. The donor atom X can for example be nitrogen, oxygen or sulfur. BDFEs originally refer to homolytic cleavage of X-H bonds. By splitting up that process in subsequent PT and ET, formal BDFEs can be obtained with the following equation:

$$BDFE = 1.37\ pK_a + 23.06\ E° + C_G \qquad (1\text{-}13)$$

PT is considered with the first pK_a-dependent summand. ET is considered in the second summand with the standard redox potential $E°$. The last summand (C_G) reflects solvation of hydrogen atoms by solvent molecules.

Table 1-1 Summary of C_G and C_H constants and reference electrodes in common solvents. C_G and C_H.[10]

solvent	C_G [kcal mol^{-1}]	C_H [kcal mol^{-1}]	reference
acetonitrile	54.9	59.4	$Cp_2Fe^{+/0}$
DMSO	71.1	75.7	$Cp_2Fe^{+/0}$
DMF	69.7	74.3	$Cp_2Fe^{+/0}$
methanol	65.3	69.1	$Cp_2Fe^{+/0}$
water	57.6	55.8	NHE

For calculating BDFEs in water, $E°$ must be entered in V vs. NHE. In organic solvents, $E°$ must be entered in V vs. ferrocene. C_G values are solvent dependent and summarized in Table 1-1.[10] Acidity constant (pK_a) and standard potential ($E°$) must be entered in the

thermodynamically relevant manner, reflecting the sequence of PT followed by ET or *vice versa*. The square-scheme for a formal hydrogen atom donor X-H is presented in Scheme 1-3.
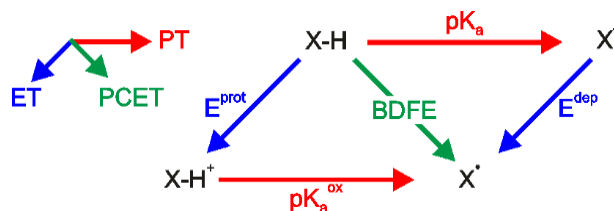
Scheme 1-3 Thermochemical square-scheme combining the acid-base and electrochemical properties and formal BDFE of a PCET reagent and formal hydrogen atom donor X-H.

Formal BDFEs can furthermore be applied to couples of ET and PT reagents, e.g. an electron donor and an acid. This broadens the scope and applicability of formal BDFEs from unidirectional to bidirectional PCET reactions.[15] The driving force for PCET reactions (ΔG_{PCET}) can be calculated from X-H BDFE of the formal hydrogen atom donor and acceptor (eq. 1-14). The formal X-H BDFE of the acceptor refers to its reduced and protonated form.

$$\Delta G_{PCET} = \Delta BDFE = BDFE(donor) - BDFE(acceptor) \qquad (1\text{-}14)$$

The unit conversion is: 1 kcal mol^{-1} = 0.0433634 eV.

Thermochemically related to the BDFE is the bond dissociation enthalpy (BDE). To obtain BDEs, pK_a and E° are relevant, as well as a solvent dependent summand C_H. The calculation of BDEs by eq. 1-15 is viable, when solvation entropies of X-H and X$^\bullet$ are essentially equal. This is the case for most organic and metalorganic compounds, except for compounds containing high spin metal ions.[10]

$$BDE = 1.37\ pK_a + 23.06\ E° + C_H \qquad (1\text{-}15)$$

Calculated BDEs in organic solvents are usually approximately 4 kcal mol^{-1} higher than their respective BDFEs, due to the difference of the solvation summands C_H and C_G.[10] Because BDFEs reflect free energies, they are more important than BDEs in assessing the PCET reactions and therefore BDFEs are considered in this work.

1.3.5 Hydrogen Bonding and its Consequences for PCET

Hydrogen bonds are most effectively formed between acids and bases when the pK_a values of the involved species are similar.[16] Hydrogen bonds can lead for example to supramolecular architectures but it also effects (proton-coupled) charge transfer reactions.[17–19] Pre-organization of reactants via hydrogen bonds can speed up reaction rates. Furthermore, hydrogen bonds can have an impact on the redox potential of proton-electron donors and accep-tors. When hydrogen bonds are formed to acids that are also the electron donor, the oxidation

potential is decreased, hence oxidation is facilitated. The effect originates from the same reason as the shift of redox potential. Upon deprotonation, electron density at the donor is enhanced, because the positively charged proton is partially removed by the hydrogen bond acceptor. In some charge transfer and PCET reactions, hydrogen bonding of electron donor and acceptor is indispensable.[19,20] Hydrogen bonding is an equilibrium between acid XH and base (eq. 1-16), quantified by the association constant K_{Hbond} (eq. 1-17). Spectroscopic methods such as NMR and UV-vis absorption can be used to evaluate the hydrogen bonding equilibrium.

$$XH + base \leftrightarrows [X\text{-}H\text{-}base] \tag{1-16}$$

$$K_{Hbond} = \frac{[X\text{-}H\text{-}B]}{[XH][B]} \tag{1-17}$$

1.4 The Electronic Excited State

Excited states of molecules or atoms are accessible upon absorption of energy, usually from an external energy resource. Usually, light serves as energy source to access electronic excited states. Upon absorption of a photon, an electron is promoted from the highest occupied molecular orbital (HOMO) to the lowest unoccupied molecular orbital (LUMO). From the energetically higher LUMO it can go back into the HOMO by releasing energy in form of a photon. Opposed to the radiative relaxation, non-radiative pathways, such as internal conversion can lead to depopulation of the LUMO and repopulation of the HOMO by releasing energy in form of heat. Other ways of depopulating the excited state are energy transfer to another molecule or follow-up reactions, such as dissociation, redox chemistry and other radical reactions. For the context of this thesis, luminescence, excited state proton transfer, redox chemistry and PCET are important and treated in the following sections.
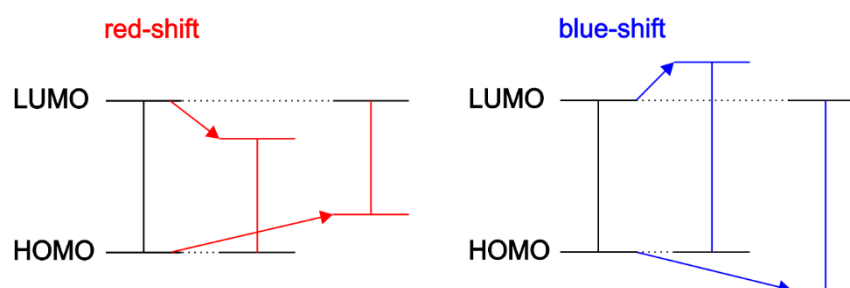

Scheme 1-4 Spectral shift of HOMO-LUMO gap result from energetic changes of LUMO or HOMO.

The energy difference between the lowest vibronic energy levels of HOMO and LUMO is E_{00}. It can be probed at low temperature as described extensively for $Ru(bpy)_3^{2+}$ in the solid

state.[21] Low temperatures are used to avoid band-broadening because of population of higher vibrational levels. To avoid solvent effects, either solid samples can be used, or frozen glasses at 77 K. Above the melting point of the medium, solvent molecules can adjust to the changed geometry and charge distribution of the luminophore, thereby stabilizing the energy of the LUMO. The result of LUMO stabilization is a red-shift of the luminescence spectrum, as depicted in Scheme 1-4. Destabilization of the HOMO energy at constant LUMO energy can have the same red-shift in luminescence as well as a combination of both. Blue shifted luminescence results from an increase of energy difference between LUMO and HOMO. It can be the result of a destabilized LUMO, or stabilized HOMO or a combination of both. Often, both orbitals shift into the same direction. The respective red or blue shift is due to one orbital shifting which is stronger than the other.

One example for destabilizing HOMO *and* LUMO is the deprotonation of luminescent acids, as depicted for a photoacid in Scheme 1-5. Photoacids are easier deprotonated in the excited state compared to the ground state. This manifests in a smaller up-shift of the LUMO compared to the HOMO and therefore in a red-shift of luminescence of the conjugated base, compared to the acid. For a photobase, a blue-shift is expected.
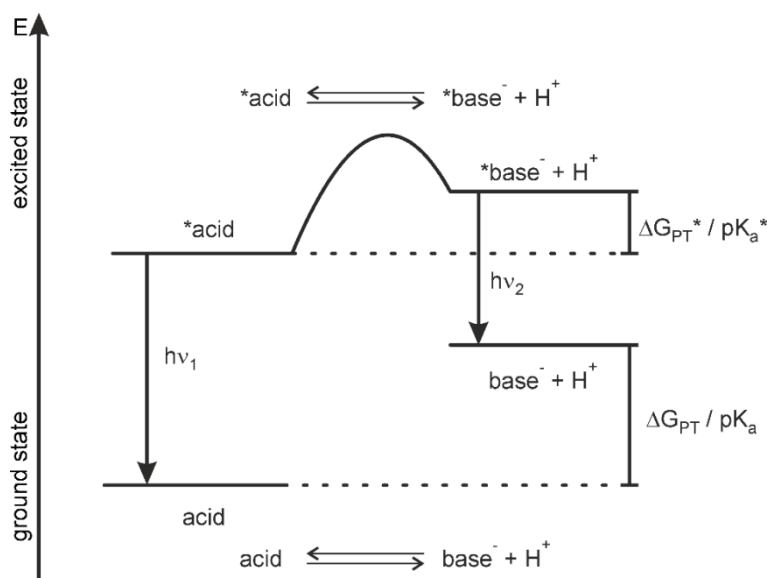
Scheme 1-5 Proton transfer in ground and excited state of a photoacid. Picture adapted from literature.[22]

The excited state acidity constant (pK_a^*) of an acid can be assessed by the Förster equation (eq. 1-18), where h is Planck's constant, R is the gas constant, T the temperature and the wavenumbers ν_1 and ν_2 refer to the excited state energies of acid and conjugated base.[22]

$$pK_a^* = pK_a - \frac{h\nu_1 - h\nu_2}{2.3\,RT} \tag{1-18}$$

The Förster equation is derived from the assumption that the protonation equilibrium in the excited state is achieved within the lifetime of the excited state. A change of acidity in the excited state (ΔG_{PT*}, pK_a^*) compared to the ground state (ΔG_{PT}, pK_a) leads to energetic changes in the excited state.
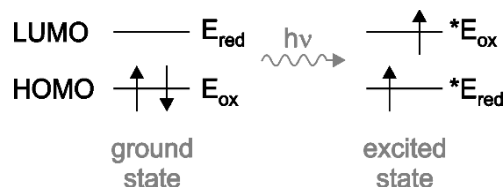

Scheme 1-6 Simplified electronic configuration of ground state and electronically excited state. Ground state: Reduction takes place in the LUMO and oxidation in the HOMO. Excited state: Reduction takes place in the HOMO and oxidation in the LUMO (here shown for triplet excited state).

Oxidation in the ground state takes place in the highest occupied molecular orbital (HOMO) and reduction takes place in the lowest unoccupied molecular orbital (LUMO). In contrast, in the excited state oxidation occurs at the LUMO whereas reduction takes place at the HOMO (see Scheme 5). Oxidation in the excited state is facilitated by the energy difference between HOMO and LUMO (E_{00}) and therefore E_{00} is subtracted from E_{ox} (eq. 1-19). Similarly, the excited state reduction potential is increased by E_{00} as shown in eq. 1-20. The excited state energy (E_{00}) can be determined experimentally by absorption and luminescence spectroscopy.

$$^*E_{ox} = E_{ox} - E_{00} \tag{1-19}$$

$$^*E_{red} = E_{red} + E_{00} \tag{1-20}$$

As described earlier, the two key parameters in PCET chemistry are acidity constants (pK_a) and redox potentials ($E°$). In the electronically excited state, these two parameters differ from the ground state, as described in the previous two sections. Depending on the nature of the PCET reagent, the acidity can be increased or decreased upon excitation. Redox processes are usually facilitated in the excited state.
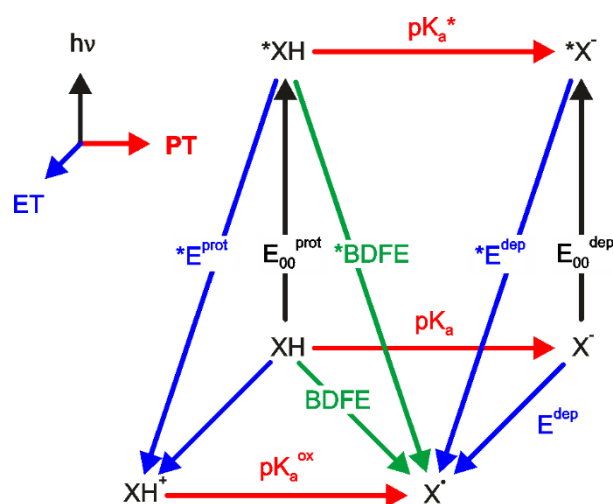
Scheme 1-7 Thermodynamic "cube-scheme" for a proton-electron donor XH. Horizontal in red: pKa values for PT reactivity, vertical in black: excited state energy E_{00}, pointing towards the reader in blue: redox potentials, diagonal in green: BDFEs.

Based on the ground-state PCET square-scheme, an expanded square-scheme can be drawn (Scheme 1-7). It includes excited state thermochemistry in the third coordinate and is therefore called "cube-scheme". The arrows show the relation of each species to another and the respective thermochemical parameter. *BDFE of a proton-electron donor can be calculated with eq. 1-13 and the following value couples: either pK_a^* and $^*E^{dep}$, or $^*E^{prot}$ and pK_a^{ox}.[23–25]

2 Ruthenium(II) Pyridylimidazole Complexes and Their Redox and PCET Reactivity in Ground and Excited State

The use of visible light as principal energy source for chemical transformation is highly attractive for avoiding harsh reaction conditions. Especially photo redox chemistry holds promising perspectives in this field. Usually oxidation or reduction of a substrate goes along with the release or uptake of protons resulting in classical (formal) hydrogen atom transfer (HAT) or (de-) hydrogenation, respectively. Protonation and deprotonation can facilitate redox processes substantially which makes proton-coupled electron transfer (PCET) a very useful method for chemical transformations. The benefits of excited state redox chemistry and PCET chemistry can directly be combined for photosensitizers exhibiting a (de-) protonation site. Suitable photosensitizers in this context are ruthenium polyimine complexes because they have long living and reactive ^{3}MLCT excited states. The most famous complex in this context is $[Ru(bpy)_3]^{2+}$ (bpy = 2,2'-bipyridine). Upon exchange of one bpy ligand to a pyridylimidazole which can be protonated or deprotonated, PCET in ground and excited state becomes possible. $[Ru(bpy)_2(pyimH)]^{2+}$ (pyimH = 2-(2'-pyridyl)imidazole) has one deprotonatable imidazole-unit and therefore provides the basis for PCET chemistry and formal hydrogen atom transfer. The PCET mechanism of the formal hydrogen atom transfer from excited state $[Ru(bpy)_2(pyimH)]^{2+}$ to N-methyl-4,4'-bipyridinium (Monoquat, MQ$^+$) was investigated, as well as the tunability of ground and excited state redox potentials and formal bond dissociation free energies (BDFE) of the family of $[Ru(R_2\text{-bpy})_2(pyimH)]^{2+}$ with R = H, CF$_3$, ^{t}Bu and NMe$_2$.
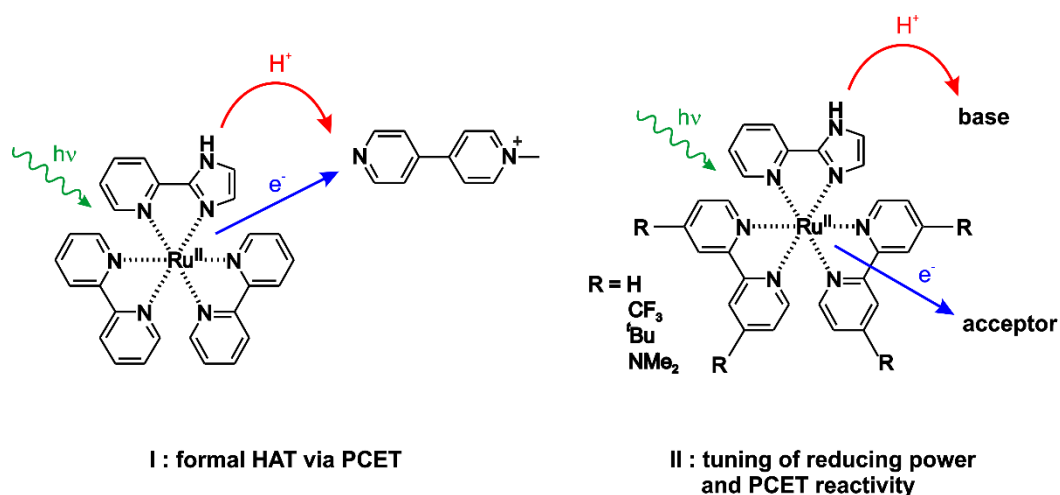

Figure 2-1 The investigated family of $[Ru(R_2\text{-bpy})_2(pyimH)]^{2+}$ complexes.

The following articles were published in this context:

I.   Pannwitz, A.; Wenger, O. S. 'Proton coupled electron transfer from the excited state of a ruthenium(II) pyridylimidazole complex' *Phys. Chem. Chem. Phys.* **2016**, *18*, 11374–11382. (DOI: 10.1039/C6CP00437G)

II.   Pannwitz, A.; Prescimone, A.; Wenger, O. S. 'Ruthenium(II)-Pyridylimidazole Complexes as Photoreductants and PCET Reagents' *Eur. J. Inorg. Chem.* **2017**, *2017*, 609–615. (DOI: 10.1002/ejic.201601403)

It was shown that the formal bond dissociation free energy (BDFE) of the imidazole-N–H bond of $[Ru(bpy)_2(pyimH)]^{2+}$ decreases from (91 ± 1) kcal mol^{-1} in the electronic ground state to (43 ± 5) kcal mol^{-1} in the ^{3}MLCT excited state. This makes the $[Ru(bpy)_2pyimH]^{2+}$ complex a very strong formal hydrogen atom donor in its excited state, even when compared to metal hydride complexes that are used in hydrogenations. MQ$^+$ was chosen as a suitable HAT acceptor to support this hypothesis spectroscopically. Formal HAT between ^{3}MLCT excited $[Ru(bpy)_2pyimH]^{2+}$ and MQ$^+$ in buffered 1:1 (v:v) acetonitrile/water was found to be compatible with excited state deprotonation. It takes place via a PCET mechanism. Electron transfer from Ru(II) to MQ$^+$ is coupled to release of the N–H proton to buffer base, followed by protonation of reduced MQ$^+$ by buffer acid. Simple electron transfer between excited $[Ru(bpy)_2pyimH]^{2+}$ and protonated acceptor at acidic pH is possible, as well as electron transfer between deprotonated ^{3}MLCT excited ruthenium complex and MQ$^+$ at basic pH. In the intermediate pH range around pH 6, formal HAT takes place.

By substituting the bpy spectator ligands with electron withdrawing and donating groups, namely CF$_3$, ^{t}Bu, and NMe$_2$, the excited state BDFE was tuned between 34 and 52 kcal mol^{-1} and the ground state BDFE was tuned between 79 and 96 kcal mol^{-1}. Furthermore, it was shown that the reducing power of these complexes is enhanced by 0.1 - 0.3 eV by simple deprotonation.

In these studies, a family of $[Ru(R_2$-bpy$)_2pyimH]^{2+}$ complexes were shown to be strong reductants and PCET reagents in the excited state. The thermochemistry of the investigated complexes was determined which makes it possible to estimate their redox and PCET reactivity in ground and photo-excited state. This is relevant in the contexts of light-to-chemical energy conversion, especially in the field of photoredox catalysis and photoinduced hydrogenation and dehydrogenations via PCET mechanism.

Author Contributions:

- Andrea Pannwitz carried out synthesis and performed and analyzed all photochemical and photophysical measurements. She contributed equally to data interpretation and the preparation of the manuscripts.

- Alessandro Prescimone measured and solved the single-crystal structure.

- Oliver S. Wenger drafted the main concept of the project, contributed equally to data interpretation and the preparation of the manuscripts.

PCCP

Cite this: *Phys. Chem. Chem. Phys.,* 2016, **18**, 11374

Proton coupled electron transfer from the excited state of a ruthenium(II) pyridylimidazole complex†

Andrea Pannwitz and Oliver S. Wenger*

Proton coupled electron transfer (PCET) from the excited state of $[Ru(bpy)_2pyimH]^{2+}$ (bpy = 2,2′-bipyridine; pyimH = 2-(2′-pyridyl)imidazole) to *N*-methyl-4,4′-bipyridinium (monoquat, MQ^+) was studied. While this complex has been investigated previously, our study is the first to show that the formal bond dissociation free energy (BDFE) of the imidazole-N−H bond decreases from (91 ± 1) kcal mol^{-1} in the electronic ground state to (43 ± 5) kcal mol^{-1} in the lowest-energetic ^{3}MLCT excited state. This makes the $[Ru(bpy)_2pyimH]^{2+}$ complex a very strong (formal) hydrogen atom donor even when compared to metal hydride complexes, and this is interesting for light-driven (formal) hydrogen atom transfer (HAT) reactions with a variety of different substrates. Mechanistically, formal HAT between ^{3}MLCT excited $[Ru(bpy)_2pyimH]^{2+}$ and monoquat in buffered 1 : 1 (v : v) CH_3CN/H_2O was found to occur *via* a sequence of reaction steps involving electron transfer from Ru(II) to MQ^+ coupled to release of the N−H proton to buffer base, followed by protonation of reduced MQ^+ by buffer acid. Our study is relevant in the larger contexts of photoredox catalysis and light-to-chemical energy conversion.

1. Introduction

Hydrogen atom transfer (HAT) is important in enzymes and in synthetic organic chemistry, for example for hydrogenations of unsaturated compounds such as ketones and imines. It would be attractive to use visible light to perform HAT reactions under mild reaction conditions, and therefore we explored the (formal) HAT chemistry of photoexcited $[Ru(bpy)_2pyimH]^{2+}$ (bpy = 2,2′-bipyridine; pyimH = 2-(2′-pyridyl)imidazole). In pure HAT the transferred electron and proton originate from the same donor orbital, whereas in unidirectional proton coupled electron transfer (PCET) the transfer of a net hydrogen atom occurs from different donor orbitals.[1–5] This is in fact the case for excited $[Ru(bpy)_2pyimH]^{2+}$ because the metal center acts as an electron donor, whereas the proton is released from the pyimH ligand. While early PCET studies have focused largely on reactions between molecules in their electronic ground states,[6–11] photoinduced PCET is now receiving increasing attention.[1,12–25] Formal HAT between a transition metal complex in its ^{3}MLCT excited-state and various reaction partners either across a salt bridge,[14,20–23] or *via* hydrogen bonding interactions have been explored.[13,24,25] Even hydride transfer from the excited state of an iridium complex was reported recently.[26] In order to predict the reactivity of an excited state, thermodynamic quantities such

as its redox potential and acidity constant must be known.[27,28] For HAT reactions, the determination of bond dissociation free energies (BDFEs) is useful, while for PCETs the calculation of formal BDFEs has proven meaningful.[28] This is possible for reactions in the ground state as well as for reactions with excited species. Based on this concept, photochemical conversions of ketones to ketyls could be rationalized.[2,16,17]

The $[Ru(bpy)_2pyimH]^{2+}$ complex (Fig. 1) has long been known,[29] in particular Haga and coworkers explored a variety of ruthenium and osmium complexes with pyimH and related (deprotonatable) ligands.[30–35] Later, Gray and coworkers explored the acid–base and redox chemistry of $[Ru(bpy)_2pyimH]^{2+}$ and related complexes in the ground and the lowest ^{3}MLCT excited state.[29,36] However, the formal BDFE of the peripheral N–H bond of $[Ru(bpy)_2pyimH]^{2+}$ and related complexes has never been determined, and the excited-state PCET chemistry remained unexplored, except in the case of an Ir(III) complex with a

Department of Chemistry, University of Basel, St. Johanns-Ring 19, 4056 Basel, Switzerland. E-mail: oliver.wenger@unibas.ch
† Electronic supplementary information (ESI) available: additional optical spectroscopic and electro-chemical data. See DOI: 10.1039/c6cp00437g
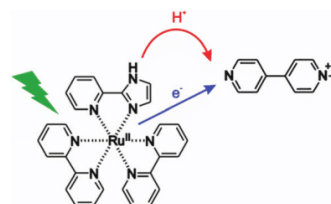

Fig. 1 The investigated process in this work: transfer of one electron and one proton from $[Ru(bpy)_2pyimH]^{2+}$ to monoquat (MQ^+) upon photoexcitation, corresponding to net transfer of a hydrogen atom.

2,2′-biimidazole ligand.[14] In structurally related complexes such as $[Ru(acac)_2pyimH]^{2+}$ (acac = acetylacetonato), formal BDFEs were estimated for the electronic ground state, and values around 62 kcal mol^{-1} were found.[9,37] We anticipated that $[Ru(bpy)_2pyimH]^{2+}$ might exhibit an unusually low N–H BDFE in its long-lived ^{3}MLCT excited state, making it potentially an equally potent (formal) hydrogen atom donor as previously investigated metal hydride complexes in their electronic ground states.[4,38]

In the following we present the thermochemical characterization of ground and ^{3}MLCT excited states of $[Ru(bpy)_2pyimH]^{2+}$ in buffered 1:1 (v:v) CH_3CN/H_2O. In this solvent mixture, well-defined pH values can easily be obtained by a variety of buffers and the solubility of $[Ru(bpy)_2pyimH]^{2+}$ as well as that of a variety of substrates is good. We find an N–H BDFE of only (43 ± 5) kcal mol^{-1} in the emissive ^{3}MLCT excited state based on thermodynamic cycles and on the photoinduced PCET chemistry with monoquat (MQ^+). The acceptor was chosen due to its ability to act as a combined electron–proton acceptor, the favourable spectroscopic properties of its radical form and the importance of pyridyl radicals for the reduction of CO_2.[39–41] The PCET reaction mechanism between photoexcited $[Ru(bpy)_2pyimH]^{2+}$ and MQ^+ was explored in detail.

2 Results and discussion

Spectroscopy and thermodynamics of the ground state

pK_a of $[Ru(bpy)_2pyimH]^{2+}$. For determination of the pK_a value of the electronic ground state, absorption spectra were recorded at different pH values between pH 3.7 and pH 10.2 (ESI,† Fig. S1a) using suitable buffers. By plotting the absorbance at the MLCT absorption maxima at 460 nm (protonated form) and 491 nm (deprotonated form) and sigmoidal fitting, $pK_a = 8.1 \pm 0.1$ was found for 1:1 (v:v) CH_3CN/H_2O (ESI,† Fig. S1b), in agreement with a prior study that reported $pK_a = 7.9 \pm 0.1$ in H_2O containing 5% methanol.[29]

pK_a of $[Ru(bpy)_2pyimH]^{3+}$. Oxidative cyclic voltammetry sweeps probing metal oxidation were performed in the pH range between pH 1 and pH 11. Characteristic voltammograms for three pH regions of interest are shown in Fig. 2a. In the acidic pH range where $[Ru(bpy)_2pyimH]^{2+}$ remains protonated after oxidation of Ru^{II} to Ru^{III}, the voltammograms show one reversible oxidation wave at $E_{ox}^{prot} = (1.00 \pm 0.05)$ V vs. SCE with peak separations between 67 and 80 mV. This behaviour is observed up to pH = 3.6 ± 0.1, corresponding to the acidity constant of $[Ru(bpy)_2pyimH]^{3+}$ (pK_a^{ox}). At higher pH values oxidation is irreversible at a sweep rate of 100 mV s^{-1} (Fig. 2a and Fig. S5 in the ESI†) due to deprotonation of the pyimH ligand of the

Fig. 2 (a) Voltammograms of $[Ru(bpy)_2pyimH]^{2+}$ in 1:1 (v:v) CH_3CN/H_2O with 0.05 M buffer at different pH values, (b) Pourbaix diagram of $[Ru(bpy)_2pyimH]^{2+}$. The slope between pH 3.6 and pH 8.1 is $-(60 \pm 4)$ mV per pH. A comprehensive set of voltammograms is shown in Fig. S5 of the ESI.†

Table 2 Ground and excited state redox potentials (E_{ox}, $*E_{ox}$), ^{3}MLCT energy (E_{0-0}), emission maxima at 25 °C (λ_{max}) and luminescence lifetimes at 25 °C under aerated and deaerated conditions of $[Ru(bpy)_2pyimH]^{2+}$ in 1:1 (v:v) CH_3CN/H_2O with 0.05 M buffer

	$[Ru(bpy)_2pyimH]^{2+}$	$[Ru(bpy)_2pyim]^+$
E_{ox} [V vs. SCE]	1.00 ± 0.05	0.73 ± 0.05
$*E_{ox}$ [V vs. SCE]	-1.1 ± 0.1	-1.2 ± 0.1
E_{0-0} [eV]	$2.1 \pm 0.1^{a,b}$	1.9 ± 0.1^b
λ_{max} [nm] 25 °C	625 ± 5	675 ± 5
τ [ns] aerated	110 ± 10	50 ± 5
τ [ns] deaerated	210 ± 20	70 ± 7

^{a} Taken from references.[29,42] ^{b} Determined from emission in ethanol/methanol 4:1 (v:v) at 77 K.

oxidized complex. Oxidation potentials of the deprotonated complex were estimated by determining the relevant inflection points of the oxidation waves. Plotting the oxidation potentials in volt vs. pH gives the data points for the Pourbaix diagram in Fig. 2b. In the range between $pK_a^{ox} = 3.6$ and $pK_a = 8.1$ the $Ru^{II/III}$ oxidation wave shifts cathodically with a slope of $-(60 \pm 4)$ mV per pH unit, as expected for a 1-electron-1-proton-process. Oxidation of the deprotonated complex, $[Ru(bpy)_2pyim]^+$, occurs at $E_{ox}^{dep} = (0.73 \pm 0.05)$ V vs. SCE (Table 2). Thus, the total cathodic shift between oxidation potentials of $[Ru(bpy)_2pyimH]^{2+}$ and $[Ru(bpy)_2pyim]^+$ is 270 mV, which is smaller than the previously reported shift of 380 mV in neat acetonitrile.[29]

Excited state properties

Excited state pK_a^* of $[Ru(bpy)_2pyimH]^{2+}$. Luminescence spectra of $[Ru(bpy)_2pyimH]^{2+}$ were measured between pH 3 and pH 10 in 1:1 (v:v) CH_3CN/H_2O containing 0.05 M buffer to control the pH (Fig. 3a). All spectra were recorded at identical complex concentration and their intensity was normalized to the intensity of the most acidic sample; excitation occurred into the isosbestic point at 474 nm (Fig. S1a, ESI†). The decrease in intensity is due to different luminescence quantum yields of the protonated and deprotonated complex and due to deprotonation in the excited state. Emission decays were measured at 630 nm to determine the lifetimes of the protonated (τ^{prot}) and deprotonated ^{3}MLCT state (τ^{dep}) in aerated and deaerated solution (Table 2). For these measurements the complex was excited at 532 nm with laser pulses of ca. 10 ns duration.

Table 1 Acidity constants of $[Ru(bpy)_2pyimH]^{2+}$ in 1:1 (v:v) CH_3CN/H_2O in the electronic ground state (pK_a), in the long-lived ^{3}MLCT excited state (pK_a^*) and in the one-electron oxidized form (pK_a^{ox})

pK_a	8.1 ± 0.1
pK_a^*	5.6 ± 0.3
pK_a^{ox}	3.6 ± 0.1
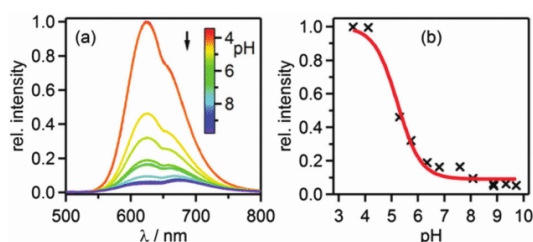
Fig. 3 (a) Luminescence of 40 μM $[Ru(bpy)_2pyimH]^{2+}$ in aerated 1:1 (v:v) CH_3CN/H_2O with 0.05 M buffer at different pH values following excitation into the isosbestic point at 474 nm. (b) Relative luminescence intensity at 625 nm vs. pH.

The acidity constant in the long-lived ^{3}MLCT-state (pK_a^*) was then determined from the inflection point of the steady-state emission titration curve ($pH_i = 5.2 \pm 0.2$) in Fig. 3b and the excited-state lifetimes of protonated (τ^{prot}) and deprotonated complex (τ^{dep}).

$$pK_a^* = pH_i + \log[\tau^{prot}/\tau^{dep}] \qquad (1)$$

With eqn (1) one obtains $pK_a^* = 5.6 \pm 0.3$.[27] Based on the emission maxima of $[Ru(bpy)_2(pyimH)]^{2+}$ and $[Ru(bpy)_2(pyim)]^+$ at 25 °C, the Förster equation yields $pK_a^* = 5.3 \pm 0.6$ (ESI,† page S6). This value is in good agreement with that determined from the luminescence titration, and also with the previously reported pK_a^* in water with 5% methanol.[29] The increase of acidity in the excited state compared to the ground state indicates that the ^{3}MLCT state is localized on the bpy spectator ligands, as noted earlier.[36]

Transient absorption spectra were measured using pulsed laser excitation at 532 nm. Under acidic conditions (Fig. 4a), $[Ru(bpy)_3]^{2+}$-like transient spectra were observed, exhibiting a bleach around 450 nm and increased intensity around 370 nm.[43] At basic pH the MLCT band is red-shifted (ESI,† Fig. S1), and therefore the MLCT-bleach in transient absorption is red-shifted as well (Fig. 4b). Transients that were recorded in the pH range between pH 5.0 and 8.1 exhibit a prominent feature at 500 nm (Fig. 4c) which can be explained by deprotonation in the excited state and the accumulation of deprotonated complex in the ground state. This interpretation is confirmed by a subtraction of the ground-state UV-vis spectra of the protonated and deprotonated complex (Fig. 4d) which also exhibits the prominent positive feature at 500 nm. The temporal evolution of this signal at pH 6.4 in presence of 0.05 M acetic acid/sodium acetate buffer and ca. 10^{-5} M complex concentration is shown below. In the absence of any reaction partner the formation of $[Ru(bpy)_2pyim]^+$, the deprotonated complex in its ground state, occurs with a time constant of $\tau = (60 \pm 10)$ ns. Re-protonation then occurs with a time constant of $\tau = (106 \pm 10)$ ns as discussed later. The kinetics of these deprotonation and protonation events are dictated by the buffer concentration. At pH 6.3 the quenching constant k_q is $(8.3 \pm 0.5) \times 10^8$ L mol^{-1} s^{-1} based on a Stern–Volmer luminescence quenching experiment (ESI,† Fig. S7).

At any given pH and buffer concentration, the amount of accumulated $[Ru(bpy)_2pyim]^+$ in the ground state correlates

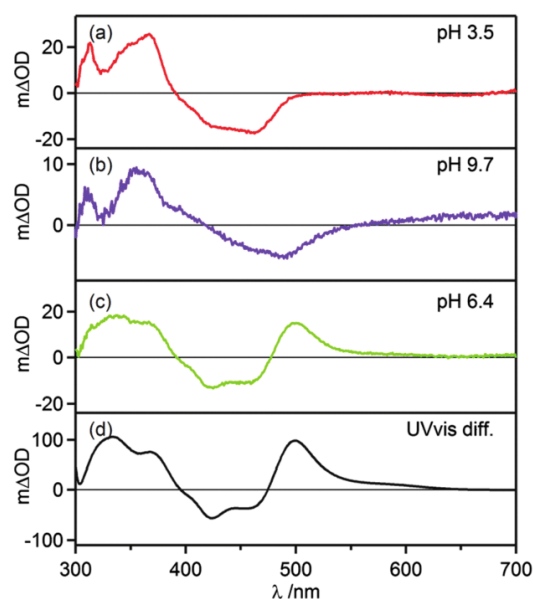Fig. 4 (a–c) Transient absorption spectra of 20 μM $[Ru(bpy)_2pyimH]^{2+}$ in 1:1 (v:v) CH_3CN/H_2O with 0.05 M buffer at different pH values. Excitation occurred at 532 nm with laser pulses of ca. 10 ns duration, the spectra were recorded without time delay over a period of 200 ns. (d) Difference of ground state UV-vis spectra of protonated and deprotonated complex.

with the acid–base equilibration in the ^{3}MLCT excited state, and this reflects directly in the intensity of the transient band at 500 nm. A plot of the change in optical density at 500 nm vs. pH yields an inflection point at pH 5.6 ± 0.2 (ESI,† Fig. S4), in line with the pK_a^* value determined by luminescence titration and the Förster equation.

Thus, at sufficiently high pH, $[Ru(bpy)_2pyimH]^{2+}$ exhibits ordinary photoacid behavior similar to hydroxyarenes such as naphthols and hydroxypyrenetrisulfonate ("pyranine").[44]

Excited state redox chemistry of $[Ru(bpy)_2pyimH]^{2+}$. The excited state oxidation potentials ($^*E_{ox}$) were estimated based on the ground state redox potentials (E_{ox}) and the ^{3}MLCT energy (E_{0-0}) using eqn (2).[42]

$$^*E_{ox} = E_{ox} - E_{0-0} \qquad (2)$$

E_{0-0} was determined from low-temperature luminescence spectroscopy (Fig. S2, ESI†). For $[Ru(bpy)_2pyimH]^{2+}$ we determined $E_{0-0}^{prot} = (2.1 \pm 0.1)$ eV[29,42] and for $[Ru(bpy)_2pyim]^+$ we found $E_{0-0}^{dep} = (1.9 \pm 0.1)$ eV. Based on these E_{0-0} values (see also Table 2), excited state redox potentials of $^*E^{prot} = -(1.1 \pm 0.1)$ V vs. SCE and $^*E^{dep} = -(1.2 \pm 0.1)$ V vs. SCE were estimated for the protonated and deprotonated complex, respectively. Expectedly, oxidation is far easier in the ^{3}MLCT excited state than in the electronic ground state.

BDFEs and "cube" scheme

A graphical summary of all relevant thermodynamic parameters for $[Ru(bpy)_2pyimH]^{2+}$ is provided in Scheme 1. This so-called

11376 | Phys. Chem. Chem. Phys., 2016, **18**, 11374–11382

This journal is © the Owner Societies 2016

31

"cube" scheme is a three dimensional illustration displaying ground state redox potentials (blue) and acidity constants (red) on the bottom and excited state potentials (blue) and pK_a values (red) on the top. ^{3}MLCT excitation energies are represented by vertical black arrows. N–H bond dissociation free energies (BDFEs) can be estimated using eqn (3) and the experimentally determined acidity constants and oxidation potentials.[2,45,46]

$$\text{BDFE (N–H)} = 1.37 \ pK_a + 23.06 \ E^\circ + 57.6 \ \text{kcal mol}^{-1} \tag{3}$$

In eqn (3), E° must be entered in units of V vs. NHE; the last summand is a solvent-characteristic parameter describing solvation of hydrogen atoms. The resulting BDFEs for $[Ru(bpy)_2pyimH]^{2+}$ in the electronic ground and excited states are BDFE = (91 ± 1) kcal mol^{-1} and *BDFE = (43 ± 5) kcal mol^{-1} (green arrows in Scheme 1). The ground-state BDFE is comparable to primary and secondary amines[2,47,48] but somewhat higher than related ruthenium pyridylimidazole complexes which were characterized in acetonitrile.[9,37] Upon photoexcitation, the BDFE drops by 48 kcal mol^{-1}, which is essentially equal to the energy of the absorbed visible photon. Interestingly, the resulting excited-state BDFE is comparable to metal hydride catalysts for hydrogenation reactions for which M–H BDFEs ranging from 50 to 55 kcal mol^{-1} for M = vanadium, 58 kcal mol^{-1} for M = chromium, and 68 kcal mol^{-1} for M = tungsten have been reported.[4,38] In principle this drop in BDFE is expected to occur for other related metal complexes in the course of photoexcitation, but prior studies have not explicitly reported on this effect. Presumably this is due to the fact that in many cases the necessary redox potentials and acidity constants were not always determined in the same solvent, which complicates the application of eqn (3). Estimations based on prior work yields for the first N–H BDFE of $[Ru(bpy)_2(2,2'-biimidazole)]^{2+}$ a decrease from 86 to 40 kcal mol^{-1} between the electronic ground state and the long-lived ^{3}MLCT state.[29,49]

In order to test whether the N–H BDFE is really that low, we set out to react photoexcited $[Ru(bpy)_2pyimH]^{2+}$ in PCET
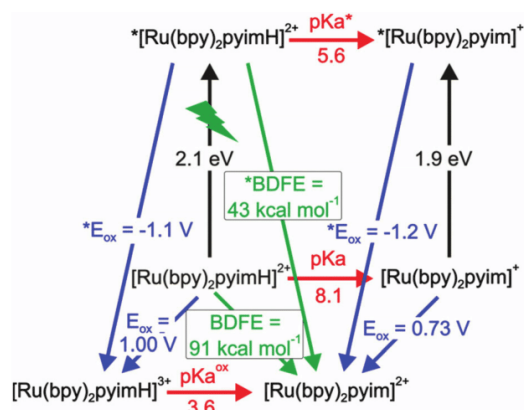
Scheme 1 Thermodynamic "cube" scheme for $[Ru(bpy)_2pyimH]^{2+}$ in 1 : 1 (v : v) CH_3CN/H_2O based on the data in Tables 1 and 2. Horizontal/red: pK_a values, orthogonal in black: triplet energy E_{0-0}, pointing towards the reader in blue: oxidation potentials in V vs. SCE, diagonal in green: BDFEs.
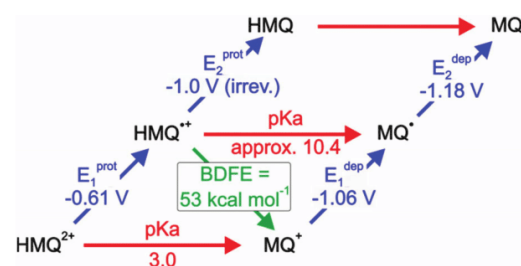
Scheme 2 Thermodynamic "square" scheme of monoquat (MQ$^+$) in 1 : 1 (v : v) CH_3CN/H_2O. Horizontal with red arrows: pK_a values, upward right with blue arrows: redox potentials in V vs. SCE, downward left with green arrow: BDFEs. The pK_a of HMQ$^{\bullet+}$ was taken from the literature.[46]

chemistry with a suitable formal H atom acceptor. We identified N-methyl-4,4'-bipyridinium (monoquat, MQ$^+$) as a promising candidate. Meyer and coworkers already proposed the use of MQ$^+$ for detecting PCET photoproducts because its one-electron reduced and protonated congener (MQH$^{\bullet+}$) exhibits absorption features that can be identified unambiguously.[50]

Before performing actual photochemical experiments between $[Ru(bpy)_2pyimH]^{2+}$ and MQ$^+$, the thermodynamic properties of MQ$^+$ in 1 : 1 (v : v) CH_3CN/H_2O were determined. The results from acid–base titration and electrochemical experiments are in the ESI† (Fig. S8 and S9). Here we merely report the final results in a thermodynamic "square" scheme (Scheme 2).

The key finding is that the HMQ$^{\bullet+}$ radical has an N–H BDFE of (53 ± 1) kcal mol^{-1}. Consequently, photoexcitation of $[Ru(bpy)_2pyimH]^{2+}$ in presence of MQ$^+$ is expected to lead to formal HAT, resulting in $[Ru(bpy)_2pyim]^+$ and HMQ$^{\bullet+}$. Based on an N–H *BDFE of (43 ± 5) kcal mol^{-1} for the photoexcited complex (Scheme 1), the driving-force for this reaction should be $-(10 \pm 6)$ kcal mol^{-1}, which corresponds to $-(0.4 \pm 0.3)$ eV. In the following we report on the photochemistry between $[Ru(bpy)_2pyimH]^{2+}$ and MQ$^+$ as a function of pH.

From simple photoinduced ET to formal HAT

In the electronic ground state, electron transfer (ET) and proton transfer reactions (PT) between $[Ru(bpy)_2pyimH]^{2+}$ and MQ$^+$ are strongly endergonic ($\Delta G_{ET} = +(2.1 \pm 0.1)$ eV, $\Delta G_{PT} = +(0.30 \pm 0.02)$ eV) and therefore no ground-state chemistry occurs. Regarding excited-state chemistry, there are in fact three different pH domains which are discussed individually in the following 3 sub-sections.

Acidic pH – photoinduced electron transfer. In the acidic range, both the complex and the acceptor are protonated in the ground and excited state. Under these conditions, the expected reaction is photoinduced electron transfer (eqn (4)).

$$*[Ru(bpy)_2pyimH]^{2+} + HMQ^{2+} \rightarrow [Ru(bpy)_2pyimH]^{3+} + HMQ^{\bullet+}$$

$$\Delta G_{ET} = -(0.5 \pm 0.2) \ \text{eV} \tag{4}$$
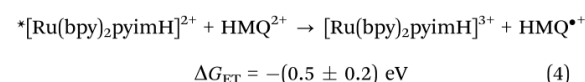
The transient absorption spectrum recorded at pH = 2 (Fig. 5a) confirms this expectation. Directly after the laser pulse one observes a bleach around 450 nm which is compatible with
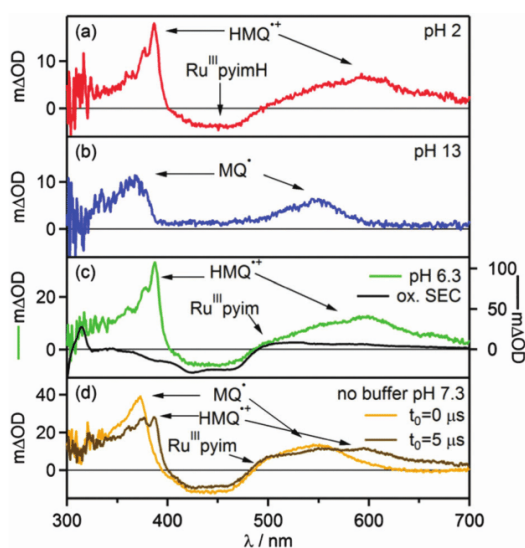
Fig. 5 Transient absorption spectra of $[Ru(bpy)_2pyimH]^{2+}$ in 1 : 1 (v : v) CH_3CN/H_2O recorded in presence of 60 mM MQ^+ following excitation at 532 nm with laser pulses of ca. 10 ns duration. Detection occurred by integration over 200 ns. (a) 30 µM $[Ru(bpy)_2pyimH]^{2+}$ at pH 2 with 0.05 M buffer, data recorded with a delay time (t_0) of 5 µs, (b) 30 µM $[Ru(bpy)_2pyimH]^{2+}$ at pH 13, data recorded with a delay time (t_0) of 5 µs, (c) 50 µM $[Ru(bpy)_2pyimH]^{2+}$ at pH 6.3 with 0.05 M acetate buffer, data recorded with a delay time (t_0) of 1 µs. (d) 50 µM $[Ru(bpy)_2pyimH]^{2+}$ in unbuffered in 1 : 1 (v : v) CH_3CN/H_2O at pH 7.3 recorded without delay time (orange trace) and with a time delay of 5 µs (brown trace).

metal oxidation, and the signatures of the $HMQ^{•+}$ cation radical appear at 387 nm and 610 nm.[46] The latter closely resemble the well-known radical of methyl viologen (MV^{2+}).[51] The photoinduced ET reaction from eqn (4) is associated with $\Delta G_{ET} = -(0.5 \pm 0.2)$ eV. A Stern–Volmer experiment under acidic conditions reveals a quenching constant of $k_q = (6.8 \pm 0.1) \times 10^8$ L mol^{-1} s^{-1} (ESI,† Fig. S14), which is comparable to what was found for the reaction of $*[Ru(bpy)_3]^{2+}$ with MV^{2+} in water ($k_q = 5.9 \times 10^8$ L mol^{-1} s^{-1}).[52,53] The thermal reverse ET from $HMQ^{•+}$ to $[Ru(bpy)_2pyimH]^{3+}$ in the electronic ground state then occurs on a time scale of approximately 100 µs, as determined by monitoring the $HMQ^{•+}$ signal at 610 nm (ESI,† Fig. S10).
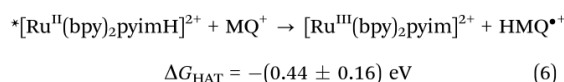
Basic pH – ET. In the basic range, the complex and the acceptor are both deprotonated in the ground and excited state, and consequently they are expected to undergo photoinduced electron transfer according to eqn (5).

$$*[Ru(bpy)_2pyim]^+ + MQ^+ \rightarrow [Ru(bpy)_2pyim]^{2+} + MQ^•$$

$$\Delta G_{ET} = -(0.14 \pm 0.15)\ \text{eV} \tag{5}$$
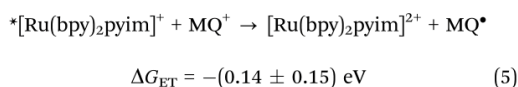
In transient absorption spectroscopy, the neutral monoquat radical $(MQ^•)$ with characteristic absorptions at 365 nm and 545 nm is observed.[51] The expected MLCT bleach of the ruthenium complex overlaps with a positive contribution of $MQ^•$ hence the flat region in the spectrum between 390 and 480 nm.

The Stern–Volmer luminescence quenching experiment yields a quenching constant of $k_q = (20.7 \pm 0.3) \times 10^8$ L mol^{-1} s^{-1} (ESI,† Fig. S15), which is close to the diffusion limit. The thermal reverse ET from $MQ^•$ to $[Ru(bpy)_2pyim]^{2+}$ takes place on a time scale of 10 µs (ESI,† Fig. S11).

Middle pH range – formal HAT. In the middle pH range the most interesting photochemistry is expected. At pH 6.3 the complex is protonated in its ground state but becomes deprotonated upon excitation to the ^{3}MLCT state as well as upon oxidation of Ru^{II} to Ru^{III} (Scheme 1). On the other hand, MQ^+ is not protonated, but it is expected to be protonated upon one-electron reduction (Scheme 2). According to the formal N–H BDFEs determined above for photoexcited $[Ru(bpy)_2pyimH]^{2+}$ ((43 ± 5) kcal mol^{-1}, Scheme 1) and for $HMQ^{•+}$ ((53 ± 1) kcal mol^{-1}, Scheme 2) the formal hydrogen atom transfer reaction in eqn (6) should be associated with a reaction free energy of $-(10 \pm 6)$ kcal mol^{-1}.

$$*[Ru^{II}(bpy)_2pyimH]^{2+} + MQ^+ \rightarrow [Ru^{III}(bpy)_2pyim]^{2+} + HMQ^{•+}$$

$$\Delta G_{HAT} = -(0.44 \pm 0.16)\ \text{eV} \tag{6}$$

In transient absorption spectroscopy the two photoproducts from eqn (6) are indeed observed (Fig. 5c). When recording transient absorption spectra with a time delay (t_0) of 1 µs there is clear evidence for $HMQ^{•+}$ (signals at 387 and 610 nm) and for $[Ru^{III}(bpy)_2pyim]^{2+}$ (bleach around 450 nm), as confirmed by spectro-electrochemical (SEC) studies (black trace in Fig. 5c). However, mechanistically direct HAT between $*[Ru^{II}(bpy)_2pyimH]^{2+}$ and MQ^+ in presence of aqueous buffer is highly improbable, particularly in view of the positive charges on both reactants. Moreover, the lowest-energetic MLCT excitation in $[Ru^{II}(bpy)_2pyimH]^{2+}$ involves promotion of an electron into a bpy-localized orbital rather than a pyimH orbital (see above).[36] Consequently, formal HAT between photoexcited $[Ru^{II}(bpy)_2pyimH]^{2+}$ and MQ^+ most likely involves a sequence of electron and proton transfer steps as illustrated in Scheme 3: following excitation of $[Ru^{II}(bpy)_2pyimH]^{2+}$, photoinduced electron transfer to MQ^+ is coupled to release of the pyimH N–H proton to buffer base (acetate anion (AcO^-), $*PT_1$ in Scheme 3). This PCET process can occur either in stepwise or concerted fashion, and it results in $[Ru^{III}(bpy)_2pyim]^{2+}$, $MQ^•$, and HOAc (PCET arrow in Scheme 3). Subsequent proton transfer (PT_2 step in Scheme 3) between buffer acid (HOAc) and $MQ^•$ then leads to the photoproducts detected in Fig. 5c. In fact, these two reaction steps can be temporally resolved (see below).

The reaction free energies for all conceivable reaction pathways are summarized in Scheme 4. The driving-forces in Scheme 4 emerge directly from the thermodynamic parameters of the two reaction partners in Schemes 1 and 2. The overall formal HAT process is dissected into photoexcitation (black arrows), electron transfer from the metal complex to monoquat (blue arrows), proton transfer from the metal complex to buffer base (PT_1, red arrows), and proton transfer from buffer acid to monoquat (PT_2, red arrows) as discussed above on the basis of Scheme 3.

From the starting point at the top left corner of Scheme 4, concerted proton-electron transfer (CPET) to form $[Ru^{III}(bpy)_2pyim]^{2+}$, $MQ^•$, and protonated buffer base (HOAc) is a plausible initial
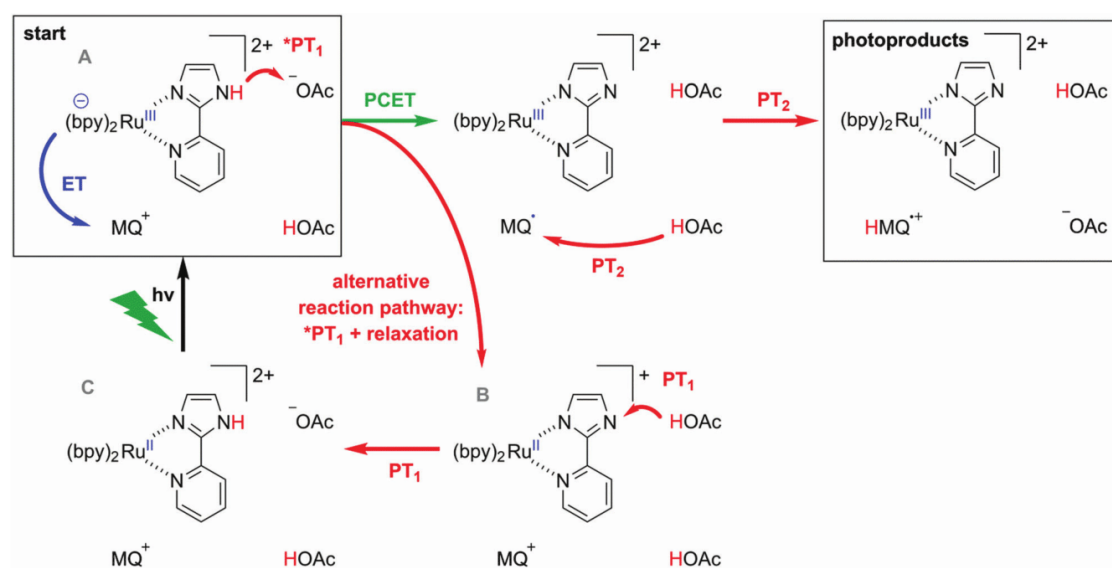
Scheme 3 Possible pathways for reaction of *[Ru(bpy)$_2$pyimH]$^{2+}$ with MQ$^+$ in acetate-buffered solution.
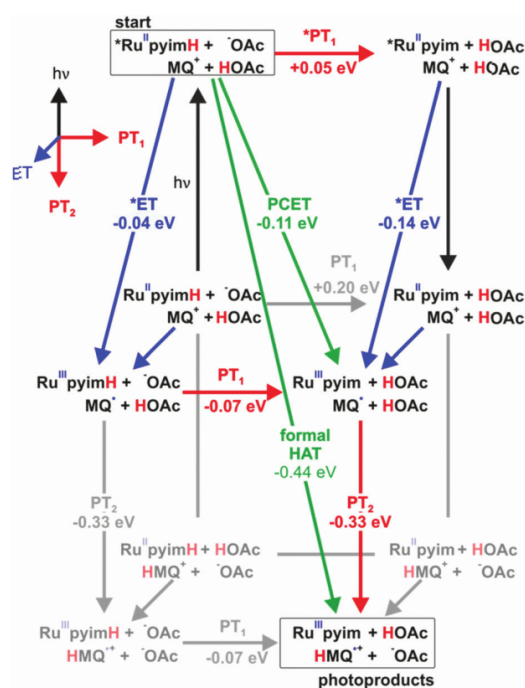
Scheme 4 Extended "cube"-scheme illustrating all reaction pathways for formal HAT between *[Ru(bpy)$_2$pyimH]$^{2+}$ and MQ$^+$ in acetate-buffered solution (based on a combination of Schemes 1 and 2). Excited state chemistry is shown in the upper level, ET processes are pointing towards the reader, PT$_1$ (complex to buffer base) is shown in horizontal direction and PT$_2$ (buffer acid to monoquat) is shown in the two lower levels. Driving forces for the individual reaction steps are based on experimentally determined redox potentials and acidity constants.

reaction pathway since $\Delta G_{PCET} = -(0.11 \pm 0.16)$ eV for this process (green arrow). However, a sequence of electron and proton transfer events cannot be excluded on thermodynamic grounds and would be equally compatible with our experimental data.

Classical Stern–Volmer luminescence quenching experiments could not be performed for determination of the kinetics of the initial PCET process (green arrow in Scheme 3) because the luminescence of [Ru(bpy)$_2$pyimH]$^{2+}$ is strongly quenched in presence of buffer molecules ($k_q = (8.3 \pm 0.5) \times 10^8$ L mol^{-1} s^{-1} as described earlier). Therefore, we performed experiments at 5 mM buffer concentration for which we used a different spectroscopic observable to monitor the kinetics of the relevant PCET process: when measuring the transient absorption spectrum immediately after laser excitation, an additional band at 500 nm becomes observable. Based on the data in Fig. 4c and d, this band can be attributed unambiguously to [Ru^{II}(bpy)$_2$pyim]$^+$, *i.e.*, to the deprotonated Ru^{II} complex in the electronic ground state. This species accumulates in a side-reaction to PCET as illustrated in the lower line, right side of Scheme 3; a subset of all excited complexes undergoes PCET chemistry to the photoproducts shown in the top right corner of Scheme 3 whereas another subsets merely acts as a photoacid (lower line, right side). Thus, the intensity of the transient absorption signal at 500 nm is a measure for the amount of ruthenium complexes that have been photoexcited but that have not undergone PCET chemistry. The temporal evolution of the transient signal at 500 nm shows classical A → B → C reaction kinetics (Fig. 6a), with species A corresponding to *[Ru^{II}(bpy)$_2$pyimH]$^{2+}$, species B being [Ru^{II}(bpy)$_2$pyim]$^+$, and species C corresponding to the protonated ground state as shown in Scheme 3. In absence of MQ$^+$ the signal at 500 nm rises with $\tau^{A \to B} = (105 \pm 10)$ ns and decays with $\tau^{B \to C} = (1.0 \pm 0.1)$ μs. With increasing MQ$^+$ concentration $\tau^{A \to B}$ decreased, $\tau^{B \to C}$ remained constant and

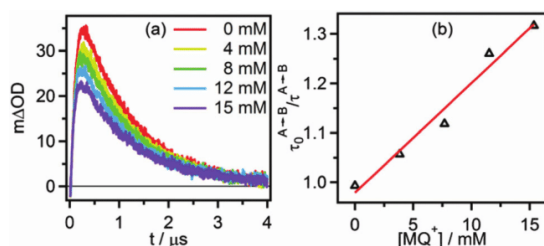This journal is © the Owner Societies 2016

Phys. Chem. Chem. Phys., 2016, **18**, 11374–11382 | **11379**

Fig. 6 (a) Change in optical density at 500 nm as a function of time after 532 nm excitation of 40 μM [Ru(bpy)$_2$pyimH]$^{2+}$ in 1:1 (v:v) CH$_3$CN/H$_2$O containing 5 mM acetate buffer and increasing concentrations of MQ$^+$. (b) Pseudo Stern–Volmer plot based on the kinetics for step A → B with constant B → C lifetime, see text for details.

the maximum intensity of the signal decreased. A plot of $\tau_0^{A\to B}/\tau^{A\to B}$ vs. [MQ$^+$] is shown in Fig. 6b. A linear regression fit yields a pseudo-Stern–Volmer constant (K_{SV}') of (22 ± 2) L mol^{-1} and a quenching constant (k_q') of $(2.1 \pm 0.4) \times 10^8$ L mol^{-1} s^{-1}. This PCET-quenching constant is on the same order of magnitude as the *PT$_1$-quenching constant and therefore both processes are competitive.

In buffered solution at pH 6.3 the final PCET photoproducts (i.e. [Ru^{III}(bpy)$_2$pyim]$^{2+}$ and HMQ$^{\bullet+}$) are formed within the first microsecond at buffer concentrations between 5 and 50 mM (Fig. 5c). When monitoring the transient absorption signals at 387 nm and 610 nm (Fig. 7b and c) it becomes evident that the formation of HMQ$^{\bullet+}$ occurs more slowly than deactivation of the ^{3}MLCT excited state of the [Ru^{II}(bpy)$_2$pyimH]$^{2+}$ complex (Fig. 7a). Based on the emission decay at 630 nm, the ^{3}MLCT
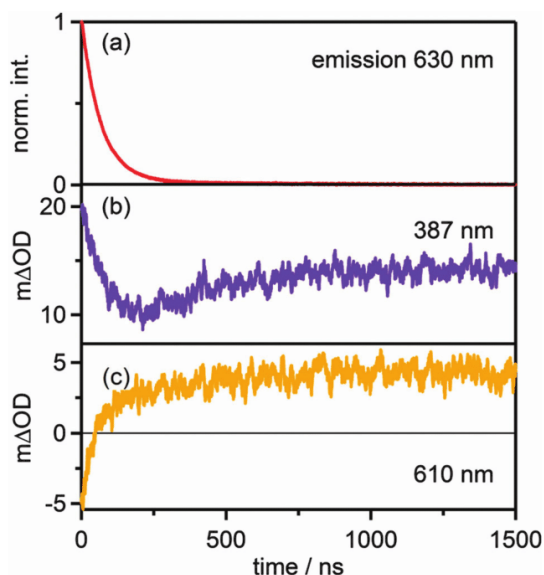

Fig. 7 (a) Decay of the emission signal at 630 nm and temporal evolution of the transient absorption signal at 387 nm (b) and at 610 nm (c) in the reaction of 40 μM [Ru(bpy)$_2$pyimH]$^{2+}$ with 15 mM MQ$^+$ in 1:1 (v:v) CH$_3$CN/H$_2$O at pH 6.3 with 5 mM acetate buffer.

Table 3 Stern–Volmer constants (K_{SV}) and bimolecular luminescence quenching constants (k_q) for *[Ru(bpy)$_2$pyimH]$^{2+}$ in presence of MQ$^+$ in deaerated 1:1 (v:v) CH$_3$CN/H$_2$O at different pH values in absence and presence of buffer

Conditions	K_{SV} [L mol^{-1}]	k_q [10^8 L mol^{-1} s^{-1}]	Process
Buffered pH 2	143 ± 13	6.8 ± 0.1	ET
Unbuffered pH 13	124 ± 12	20.7 ± 0.3	ET
Buffered pH 6.3	34 ± 2	5.7 ± 0.3	PCET
Unbuffered H$_2$O pH 7.3	70 ± 5	3.4 ± 0.5	PCET
Unbuffered D$_2$O pD 7.3	58 ± 6	2.5 ± 0.8	PCET

lifetime under these conditions is (70 ± 7) ns. Biexponential fits to the transients at 387 nm and 610 nm yield time constants of (70 ± 7) ns and (250 ± 25) ns with different signs of amplitude, corresponding to the ^{3}MLCT lifetime and the time constant for formation of HMQ$^{\bullet+}$, respectively. Thus, photoexcited [Ru^{II}(bpy)$_2$pyimH]$^{2+}$ disappears more rapidly than HMQ$^{\bullet+}$ forms, and this can be explained by rapid PCET (green arrow in Scheme 3) followed by slow PT$_2$ (red arrow in Scheme 3). By increasing the buffer concentration the kinetics of these processes is accelerated as described in the ESI† (Fig. S12).

In absence of buffer the reaction kinetics are different. The absence of buffer base leaves MQ$^+$ and water molecules as potential proton acceptors. The luminescence quenching experiment performed with acetate buffer (Fig. S7, ESI†) clearly shows that buffer base is a far better proton acceptor than water vis-à-vis photoexcited [Ru^{II}(bpy)$_2$pyimH]$^{2+}$. Transient absorption spectra recorded in 1:1 (v:v) CH$_3$CN/H$_2$O in absence of buffer are shown in Fig. 5d. The spectrum recorded without time delay (orange trace in Fig. 5d) is compatible with the formation of neutral MQ$^{\bullet}$ radical as a primary photoproduct, exhibiting a characteristic broad absorption centered on 545 nm. After 5 μs the population of MQ$^{\bullet}$ has decreased and HMQ$^{\bullet+}$ can be detected (brown trace in Fig. 5d). Thus, the overall photochemistry is the same as in presence of buffer (PCET followed by PT$_2$), but the kinetics are much different. The time constant for protonation of MQ$^{\bullet}$ is (2.5 ± 0.3) μs based on the temporal evolution of the transient signal at 610 nm (ESI,† Fig. S13a) which is a factor of 10 slower than in the presence of 5 mM acetate buffer. Stern–Volmer luminescence quenching studies yielded $k_q = (3.4 \pm 0.5) \times 10^8$ L mol^{-1} s^{-1} for the initial excited-state quenching process. When going from CH$_3$CN/H$_2$O to CH$_3$CN/D$_2$O, the protonation of MQ$^{\bullet}$ (PT$_2$) is slowed down by a factor of 2.6, and the initial excited state quenching process becomes a factor of (1.4 ± 0.6) slower (Table 3). In principle, an H/D kinetic isotope effect of 1.4 would be compatible with concerted electron–proton transfer (CPET), but definitive assignment of the PCET step in Scheme 3 (green arrow) either to concerted or consecutive electron and proton transfer steps is currently not possible.

3 Summary and conclusion

The thermodynamic properties of [Ru(bpy)$_2$pyimH]$^{2+}$ in its electronic ground state and in the long-lived ^{3}MLCT excited state in 1:1 (v:v) CH$_3$CN/H$_2$O were explored in detail. In the

Paper

ground state the formal BDFE of the N–H bond is in the range of primary and secondary amines ((91 ± 1) kcal mol^{-1}),[2,47,48] but upon excitation with a visible photon the BDFE drops by roughly 50 kcal mol^{-1} to only (43 ± 5) kcal mol^{-1}. Thus, photoexcitation leads to a formal N–H BDFE in the range of metal hydride complexes which are used as hydrogenation catalysts in their electronic ground states.[4,38] Transient absorption spectroscopy demonstrates that photoexcited [Ru(bpy)$_2$pyimH]$^{2+}$ and (N-methyl-4,4′-bipyridinium, MQ$^+$) undergo a formal HAT reaction, thereby confirming the finding of a very low formal N–H BDFE in the ruthenium complex; in HMQ$^{\bullet+}$ the N–H BDFE is (53 ± 1) kcal mol^{-1}. Mechanistically, formal HAT between these two reactants is found to proceed *via* a sequence of PCET and proton transfer reaction steps involving buffer or solvent molecules. More generally, our study demonstrates that aromatic imines can be reduced from the excited state of [Ru(bpy)$_2$pyimH]$^{2+}$.

Acknowledgements

Notes and references

1 D. R. Weinberg, C. J. Gagliardi, J. F. Hull, C. F. Murphy, C. A. Kent, B. C. Westlake, A. Paul, D. H. Ess, D. Granville and T. J. Meyer, *Chem. Rev.*, 2012, **112**, 4016–4093.

2 J. J. Warren, T. A. Tronic and J. M. Mayer, *Chem. Rev.*, 2010, **110**, 6961–7001.

3 S. Hammes-Schiffer, *J. Am. Chem. Soc.*, 2015, **137**, 8860–8871.

4 M. Bourrez, R. Steinmetz, S. Ott, F. Gloaguen and L. Hammarström, *Nat. Chem.*, 2015, **7**, 140–145.

5 J. M. Mayer, D. A. Hrovat, J. L. Thomas and W. T. Borden, *J. Am. Chem. Soc.*, 2002, **124**, 11142–11147.

6 T. Irebo, S. Y. Reece, M. Sjödin, D. G. Nocera and L. Hammarström, *J. Am. Chem. Soc.*, 2007, **129**, 15462–15464.

7 T. Irebo, M.-T. Zhang, T. F. Markle, A. M. Scott and L. Hammarström, *J. Am. Chem. Soc.*, 2012, **134**, 16247–16254.

8 V. W. Manner, A. D. Lindsay, E. A. Mader, J. N. Harvey and J. M. Mayer, *Chem. Sci.*, 2012, **3**, 230.

9 A. Wu, J. Masland, R. D. Swartz, W. Kaminsky and J. M. Mayer, *Inorg. Chem.*, 2007, **46**, 11190–11201.

10 J. P. Roth, J. C. Yoder, T. Won and J. M. Mayer, *Science*, 2001, **294**, 2524–2526.

11 J. P. Roth and J. M. Mayer, *Inorg. Chem.*, 1999, **38**, 2760–2761.

12 O. S. Wenger, *Coord. Chem. Rev.*, 2015, **46**, 150–158.

13 J. Nomrowski and O. S. Wenger, *Inorg. Chem.*, 2015, **54**, 3680–3687.

14 J. C. Freys, G. C. Bernardinelli and O. S. Wenger, *Chem. Commun.*, 2008, 4267–4269.

15 T. T. Eisenhart and J. L. Dempsey, *J. Am. Chem. Soc.*, 2014, **136**, 12221–12224.

16 H. G. Yayla and R. Knowles, *Synlett*, 2014, 2819–2826.

17 K. T. Tarantino, P. Liu and R. R. Knowles, *J. Am. Chem. Soc.*, 2013, **135**, 10022–10025.

18 J. J. Concepcion, M. K. Brennaman, J. R. Deyton, N. V. Lebedeva, M. D. E. Forbes, J. M. Papanikolas and T. J. Meyer, *J. Am. Chem. Soc.*, 2007, **129**, 6968–6969.

19 N. V. Lebedeva, R. D. Schmidt, J. J. Concepcion, M. K. Brennaman, I. N. Stanton, M. J. Therien, T. J. Meyer and M. D. E. Forbes, *J. Phys. Chem. A*, 2011, **115**, 3346–3356.

20 Y. Deng, J. A. Roberts, S.-M. Peng, C. K. Chang and D. G. Nocera, *Angew. Chem., Int. Ed.*, 1997, **36**, 2124–2127.

21 J. P. Kirby, J. A. Roberts and D. G. Nocera, *J. Am. Chem. Soc.*, 1997, **119**, 9230–9236.

22 J. Rosenthal, J. M. Hodgkiss, E. R. Young and D. G. Nocera, *J. Am. Chem. Soc.*, 2006, **128**, 10474–10483.

23 E. R. Young, J. Rosenthal, J. M. Hodgkiss and D. G. Nocera, *J. Am. Chem. Soc.*, 2009, **131**, 7678–7684.

24 C. Bronner and O. S. Wenger, *J. Phys. Chem. Lett.*, 2012, **3**, 70–74.

25 C. Bronner and O. S. Wenger, *Inorg. Chem.*, 2012, **51**, 8275–8283.

26 S. M. Barrett, C. L. Pitman, A. G. Walden and A. J. M. Miller, *J. Am. Chem. Soc.*, 2014, **136**, 14718–14721.

27 J. F. Ireland and P. A. H. Wyatt, *Adv. Phys. Org. Chem.*, Elsevier, 1976, vol. 12, pp. 131–221.

28 C. R. Waidmann, A. J. M. Miller, C.-W. A. Ng, M. L. Scheuermann, T. R. Porter, T. A. Tronic and J. M. Mayer, *Energy Environ. Sci.*, 2012, **5**, 7771–7780.

29 M.-A. Haga, *Inorg. Chim. Acta*, 1983, **75**, 29–35.

30 M.-A. Haga and A. Tsunemitsu, *Inorg. Chim. Acta*, 1989, **164**, 137–142.

31 A. M. Bond and M. Haga, *Inorg. Chem.*, 1986, **25**, 4507–4514.

32 M. Haga, M. M. Ali, S. Koseki, K. Fujimoto, A. Yoshimura, K. Nozaki, T. Ohno, K. Nakajima and D. J. Stufkens, *Inorg. Chem.*, 1996, **35**, 3335–3347.

33 M.-A. Haga, *Inorg. Chim. Acta*, 1980, **45**, L183–L184.

34 M. Haga, T. Ano, T. Ishizaki, K. Kano, K. Nozaki and T. Ohno, *J. Chem. Soc., Dalton Trans.*, 1994, 263.

35 X. Xiaoming, M. Haga, T. Matsumura-Inoue, Y. Ru, A. W. Addison and K. Kano, *J. Chem. Soc., Dalton Trans.*, 1993, 2477.

36 K. M. Lancaster, J. B. Gerken, A. C. Durrell, J. H. Palmer and H. B. Gray, *Coord. Chem. Rev.*, 2010, **254**, 1803–1811.

37 A. Wu and J. M. Mayer, *J. Am. Chem. Soc.*, 2008, **130**, 14745–14754.

38 J. Choi, M. E. Pulling, D. M. Smith and J. R. Norton, *J. Am. Chem. Soc.*, 2008, **130**, 4250–4252.

39 A. J. Morris, R. T. McGibbon and A. B. Bocarsly, *ChemSusChem*, 2011, **4**, 191–196.

40 J. Chen, K. Wu, B. Rudshteyn, Y. Jia, W. Ding, Z.-X. Xie, V. S. Batista and T. Lian, *J. Am. Chem. Soc.*, 2016, **138**, 884–892.

41 D. J. Boston, C. Xu, D. W. Armstrong and F. M. MacDonnell, *J. Am. Chem. Soc.*, 2013, **135**, 16252–16255.

42 A. A. Vlcek, E. S. Dodsworth, W. J. Pietro and A. B. P. Lever, *Inorg. Chem.*, 1995, **34**, 1906–1913.

43 A. Yoshimura, M. Z. Hoffman and H. Sun, *J. Photochem. Photobiol., A*, 1993, **70**, 29–33.

44 L. M. Tolbert and K. M. Solntsev, *Acc. Chem. Res.*, 2002, **35**, 19–27.

45 J. W. Park, Y. Kim and J. M. Kim, *Bull. Korean Chem. Soc.*, 1993, 174–175.

46 A. Harriman, G. R. Millward, P. Neta, M. C. Richoux and J. M. Thomas, *J. Phys. Chem.*, 1988, **92**, 1286–1290.

47 F. G. Bordwell, X. Zhang and J. P. Cheng, *J. Org. Chem.*, 1991, **56**, 3216–3219.

48 F. G. Bordwell, X. M. Zhang and J. P. Cheng, *J. Org. Chem.*, 1993, **58**, 6410–6416.

49 D. P. Rillema, R. Sahai, P. Matthews, A. K. Edwards, R. J. Shaver and L. Morgan, *Inorg. Chem.*, 1990, **29**, 167.

50 C. J. Gagliardi, B. C. Westlake, C. A. Kent, J. J. Paul, J. M. Papanikolas and T. J. Meyer, *Coord. Chem. Rev.*, 2010, **254**, 2459–2471.

51 P. S. Braterman and J. I. Song, *J. Org. Chem.*, 1991, **56**, 4678–4682.

52 D. M. Roundhill, *Photochemistry and Photophysics of Metal Complexes*, Springer US, Boston, MA, 1994.

53 A. Juris, V. Balzani, F. Barigelletti, S. Campagna, P. Belser and A. von Zelewsky, *Coord. Chem. Rev.*, 1988, **84**, 85–277.

Full Paper

▌ **Proton–Coupled Electron Transfer**

Ruthenium(II)–Pyridylimidazole Complexes as Photoreductants and PCET Reagents

Andrea Pannwitz,[a] Alessandro Prescimone,[a] and Oliver S. Wenger*[a]

Abstract: Complexes of the type $[Ru(bpy)_2pyimH]^{2+}$ [bpy = 2,2′-bipyridine; pyimH = 2-(2-pyridyl)imidazole] with various substituents on the bpy ligands can act as photoreductants. Their reducing power in the ground state and in the long-lived ^{3}MLCT excited state is increased significantly upon deprotonation, and they can undergo proton-coupled electron transfer (PCET) in the ground and excited state. PCET with both the proton and electron originating from a single donor resembles hydrogen atom transfer (HAT) and can be described thermodynamically by formal bond dissociation free energies (BDFEs).

Whereas the class of complexes studied herein has long been known, their N–H BDFEs have not been determined even though this is important in view of assessing their reactivity. Our study demonstrates that the N–H BDFEs in the ^{3}MLCT excited states are between 34 and 52 kcal mol^{-1} depending on the chemical substituents at the bpy spectator ligands. Specifically, we report on the electrochemistry and PCET thermochemistry of three heteroleptic complexes in 1:1 (v/v) CH_3CN/H_2O with CF_3, tBu, and NMe_2 substituents on the bpy ligands.

Introduction

In the context of photochemistry and solar-energy conversion, transition-metal complexes traditionally play an important role. Especially d^6 metal complexes such as $Ru(bpy)_3^{2+}$ are useful photosensitizers, due to the long-living ^{3}MLCT excited states that are accessible with visible light irradiation.[1,2] Redox processes from this state are energetically favored compared with the ground state, and absorbed light energy can be transformed into chemical energy, for example by photoredox catalysis in organic synthesis,[3–5] or the generation of so-called solar fuels.[6–8] In the general context of redox catalysis and charge transfer, the coupling to proton transfer can play a crucial role, because energy barriers can be lowered substantially by proton-coupled electron transfer (PCET), and reduction products can be stabilized by protonation, whereas oxidation products can be stabilized by deprotonation. It would be attractive to combine the benefits of PCET with the principle of using light as the principal energy input.[9–13] In some previous studies, photons were used to generate reactive species that could subsequently undergo PCET in the electronic ground state.[14–19] A very promising approach is the use of photoexcited metal complexes and external bases or acids.[10,11,20,21] PCET reactions and even hydride transfer directly involving the excited-state species are possible and have received increasing attention.[22–32]

We report here on the ground- and excited-state properties of a family of ruthenium–diimine complexes bearing a pyimH ligand (Figure 1). The imidazole unit of the pyimH ligand can be deprotonated, and this drastically influences the redox properties of the entire complex. Strong reductants are accessible by photoexcitation, particularly when combined with deprotonation.
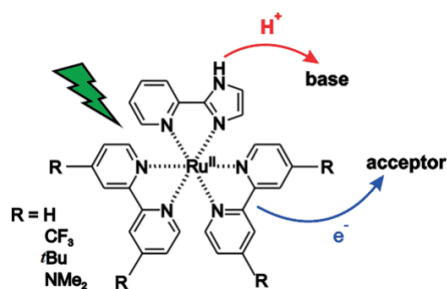
Figure 1. Investigated $[Ru^RpyimH]^{2+}$ complexes and their PCET reactivity.

Recently, we reported on the $[Ru^RpyimH]^{2+}$ complex with R = H, in which two unsubstituted bpy spectator ligands were present.[27] Building on prior work,[33,34] we demonstrated that the combined release of an electron and a proton makes this complex a very strong (formal) hydrogen atom donor in the long-lived ^{3}MLCT excited state. Mechanistically, formal hydrogen atom transfer (HAT) is a PCET process, but thermodynamically the determination of a formal N–H BDFE is meaningful.[35,36] For the $[Ru^RpyimH]^{2+}$ complex with R = H, we determined 43 kcal mol^{-1} in 1:1 (v/v) CH_3CN/H_2O. In this work, we explored to what extent the formal N–H BDFE is tunable by altering the bpy spectator ligands. This seems important in view

[a] *Department of Chemistry, University of Basel*
St. Johanns-Ring 19 and Spitalstrasse 51, 4056 Basel, Switzerland
E-mail: oliver.wenger@unibas.ch
www.chemie.unibas.ch/~wenger/index.html
💻 *Supporting information and ORCID(s) from the author(s) for this article are*
ⓘ *available on the WWW under http://dx.doi.org/10.1002/ejic.201601403.*

Wiley Online Library 609

of tailoring the excited-state redox and PCET reactivity for specific applications.

In general, the BDFE for an X–H bond can be estimated from the reaction free energies associated with the individual electron and proton transfer steps, as shown in the so-called square scheme in Scheme 1. Proton transfer (PT) and electron transfer (ET) are thermodynamica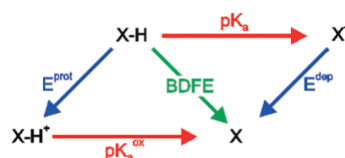lly characterized by the acidity constant (pK_a) and the redox potential ($E°$), respectively. In aqueous solution, the X–H BDFE can be calculated from Equation (1), where $E°$ must be entered in units of V vs. NHE, and the last summand is a solvent-characteristic parameter describing solvation of hydrogen atoms.[35]

$$\text{BDFE(X–H)} = 1.37\ pK_a + 23.06\ E° + 57.6\ \text{kcal mol}^{-1} \qquad (1)$$

Scheme 1. Thermochemical square scheme for the cleavage of X–H bonds by individual deprotonation (pK_a, pK_a^{ox}) and oxidation steps (E^{prot}, E^{dep}).

As noted above, the complex with R = H exhibits a formal N–H BDFE of only 43 kcal mol^{-1},[27] which is comparable to metal hydride complexes such as HV(CO)$_4$(P-P) [with P-P = Ph$_2$P(CH$_2$)$_n$PPh$_2$] or (Cp)Cr(CO)$_3$H (with Cp = cyclopentadienyl). The low N–H BDFE in our [Ru^{H}pyimH]$^{2+}$ complex results from the conversion of light energy into chemical energy, and it is manifested by the lowering of the N–H BDFE by ca. 50 kcal mol^{-1} between the ground and the excited state. This energy difference corresponds essentially to the absorbed visible photon. In this work, three derivatives of the parent complex with different chemical substituents at the 4- and 4′-positions of the bpy spectator ligands are characterized in their ground and excited states in 1:1 (v/v) CH$_3$CN/H$_2$O mixture. We find that it is possible to tune the excited-state BDFEs between 52 kcal mol^{-1} (R = CF$_3$) and 34 kcal mol^{-1} (R = NMe$_2$), with the latter being an unusually low value.[10,37,38]

Results and Discussion

Synthesis and Crystallographic Characterization

All commercially available chemicals for synthesis, including 4,4′-di-tert-butyl-2,2′-bipyridine and RuCl$_3$·3H$_2$O, were used as received. The syntheses of the ligands 2-(2-pyridyl)imidazole (pyimH) and 4,4′-bis(dimethylamino)-2,2′-bipyridine was achieved by applying known procedures.[39,40] All [Ru^{R}pyimH]$^{2+}$ complexes were isolated as PF$_6^-$ salts. The preparation of [Ru^{CF3}pyimH](PF$_6$)$_2$ followed the previously published procedure.[41] The syntheses of [Ru^{tBu}pyimH](PF$_6$)$_2$ and [Ru^{NMe2}-pyimH](PF$_6$)$_2$ were similar.[40–42] Synthetic procedures, including complex and ligand syntheses are reported in the Experimental Section and in the Supporting Information.

Monocrystalline needles of [Ru^{NMe2}pyimH](PF$_6$)$_2$ were obtained by slow diffusion of diethyl ether into a solution of the compound in acetonitrile (Figure 2). It crystallized in space group P$\bar{1}$ with two PF$_6^-$ counterions, 0.5 acetonitrile, and 0.5 diethyl ether molecules per complex in the asymmetric unit. Crystallographic details are included in the Supporting Information.
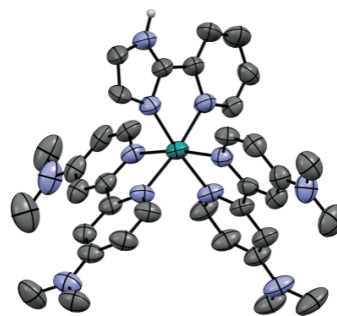

Figure 2. Crystal structure of [Ru^{NMe2}pyimH]$^{2+}$. Thermal ellipsoids are drawn at the 50 % probability level. Solvent molecules, counterions, and hydrogen atoms, except N–H, are omitted for clarity.

Redox and Acid-Base Chemistry

As described in the Introduction, the formal BDFE of the pyimH N–H functionality can be calculated on the basis of redox and acid-base properties to predict formal HAT or PCET behavior in the ground and excited states.[27,35] For the [Ru^{R}pyimH]$^{2+}$ complexes with R = CF$_3$, tBu and NMe$_2$, the relevant parameters were determined analogously to our previously published example of [Ru^{H}pyimH]$^{2+}$.[27] For the determination of the ground-state acidity constant (pK_a), the spectral changes occurring in the spectral range of the ^{1}MLCT absorption band were monitored as a function of pH (see the Supporting Information, Figures S1–S3). Pourbaix diagrams (Figure 3) were established on the basis of cyclic voltammograms recorded at different pH values (see the Supporting Information, Figures S4–S6). There are three different regimes: At very basic pH, the redox potential E^{dep} is pH-independent, because the complex is deprotonated in both the Ru^{II} and Ru^{III} oxidation states. The redox potential in the strongly acidic pH regime, E^{prot}, is also pH-independent, because the complex is protonated irrespective of whether the oxidation state is +II or +III. In the intermediate pH regime, the redox potential is expected to shift with a slope of –59 mV per pH unit. For R = tBu and NMe$_2$, the oxidation process is reversible and the slopes in the one-electron, one-proton regime are –52 mV pH^{-1} and –54 mV pH^{-1} respectively (Figure 3b and c). For R = CF$_3$, a slope of –74 mV pH^{-1} was determined (Figure 3a). This deviation from ideal behavior is attributed to the irreversible nature of the one-electron oxidation process in this specific complex. In all three complexes, the acidity constant decreases by 4–5 logarithmic units upon oxidation. [Ru^{CF3}pyimH]$^{2+}$ is the most acidic (pK_a 7.2) and [Ru^{NMe2}pyimH]$^{2+}$ is the least acidic complex due to the elec-

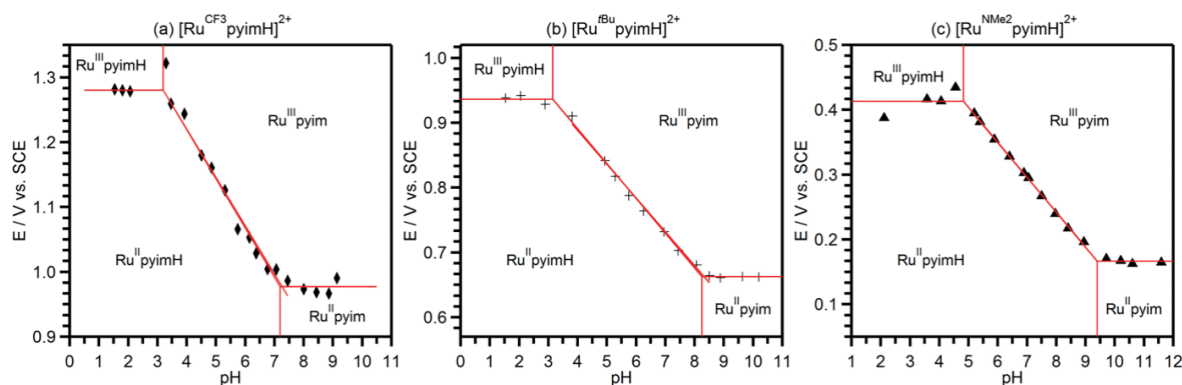Figure 3. Pourbaix diagrams for $[Ru^RpyimH]^{2+}$ in 1:1 (v/v) CH_3CN/H_2O with 0.05 M buffer. The slopes for the one-electron, one-proton redox processes are (a) −74 mV pH^{-1}, (b) −52 mV pH^{-1}, (b) −54 mV pH^{-1}, established based on the cyclic voltammetry data shown in Figures S4–S6 of the Supporting Information.

Table 1. Thermodynamic parameters for the $[Ru^RpyimH]^{2+}$ complexes in 1:1 (v/v) CH_3CN/H_2O: Acidity constants in the electronic ground state (pK_a), in the long-lived ^{3}MLCT excited state (pK_a^*) and in the one-electron oxidized form (pK_a^{ox}), oxidation potential in the ground state, ^{3}MLCT energy and oxidation potential in the excited state for protonated complex (E^{prot}, E_{00}^{prot}, $*E^{prot}$) and deprotonated complex (E^{dep}, E_{00}^{dep}, $*E^{dep}$).

R	pK_a	pK_a^*	pK_a^{ox}	E^{prot} [V vs. SCE]	E_{00}^{prot} [eV][a]	$*E^{prot}$ [V vs. SCE]	E^{dep} [V vs. SCE]	E_{00}^{dep} [eV][a]	$*E^{dep}$ [V vs. SCE]
H[b]	8.1 ± 0.1	5.6 ± 0.3	3.6 ± 0.1	1.00 ± 0.05	2.1 ± 0.1	−1.1 ± 0.1	0.73 ± 0.05	1.9 ± 0.1	−1.2 ± 0.1
CF$_3$	7.2 ± 0.1	5.3 ± 1[c]	3.2 ± 0.1	1.28 ± 0.05	1.9 ± 0.1	−0.6 ± 0.1	0.98 ± 0.05	1.8 ± 0.1	−0.8 ± 0.1
tBu	8.2 ± 0.1	5.4 ± 0.3	3.2 ± 0.1	0.94 ± 0.05	2.1 ± 0.1	−1.1 ± 0.1	0.66 ± 0.05	2.0 ± 0.1	−1.3 ± 0.1
NMe$_2$	9.2 ± 0.1	8.4 ± 0.5	4.8 ± 0.1	0.41 ± 0.05	2.0 ± 0.1	−1.6 ± 0.1	0.17 ± 0.05	1.9 ± 0.1	−1.7 ± 0.1

[a] From luminescence spectra recorded at 77 K in ethanol/methanol mixture, shown in the Supporting Information. [b] From ref.[27] [c] From ref.[41]

tronic influence of the substituents on the bpy spectator ligands (Table 1). The oxidation potential of all four pyimH complexes shifts cathodically by ca. 0.3 V upon deprotonation, in line with prior reports on iron and ruthenium complexes with deprotonatable ligands.[43–46] The highest oxidation potential is observed with the CF$_3$ substituents (E^{prot} = 1.28 ± 0.05 V vs. SCE for the protonated and E^{dep} = 0.98 ± 0.05 V vs. SCE for the deprotonated complex, respectively). The lowest oxidation potential is detected for the complex with NMe$_2$ substituents (E^{prot} = 0.41 ± 0.05 V and E^{dep} = 0.17 ± 0.05 V vs. SCE, respectively).

Excited-state oxidation potentials ($*E^{prot}$, $*E^{dep}$) were estimated from Equations (2) and (3) based on the relevant ground-state oxidation potentials (E^{prot}, E^{dep}). ^{3}MLCT energies were determined at 77 K for the protonated (E_{00}^{prot}) and deprotonated complexes (E_{00}^{dep}) (see the Supporting Information, Figure S7).

$$*E^{prot} = E^{prot} - E_{00}^{prot} \qquad (2)$$

$$*E^{dep} = E^{dep} - E_{00}^{dep} \qquad (3)$$

Photoacid Behavior and Excited-State Lifetimes

The acidity constant of the ^{3}MLCT state (pK_a^*) was estimated from the Förster equation based on the luminescence maxima of protonated and deprotonated complex (λ^{prot}, λ^{dep}) at room temperature in 1:1 (v/v) CH_3CN/H_2O.[47] For R = H and CF$_3$ the

pK_a^* values were already known,[27,41] and for the complexes with R = tBu and NMe$_2$ the Förster method was applied. The resulting pK_a^* values were verified by pH titration monitoring steady-state emission as shown in the Supporting Information (Figures S8–S9). Because the π*-orbitals of the bpy ligands are energetically lower lying than the π*-orbitals of the pyimH ligand, electron density is withdrawn from the acidic N–H functionality, and its acidity is increased in the emissive ^{3}MLCT states of all four complexes (Table 1) analogous to other photoacids.[34,48] Excited-state acid-base equilibration takes place in the pH range between pK_a and pK_a^*, where the excited $[Ru^RpyimH]^{2+}$ complexes are deprotonated by solvent or buffer molecules. Proton release then very quickly leads to the deprotonated ground state. This can unambiguously be seen in the transient absorption spectra, which are essentially the difference between the UV/Vis spectra recorded before and after laser excitation (for R = tBu in Figure 4). At pH 3 (Figure 4a) and at pH 10 (Figure 4b), a bleach between 400 and 550 nm is detected, which originates from disappearance of the ^{1}MLCT absorption. Under basic conditions, the bleach is redshifted, because the ground state is deprotonated, and the ^{1}MLCT absorption band is redshifted compared with the protonated form. At pH 6 (Figure 4c), a positive signal at around 500 nm becomes detectable, which can be explained by deprotonation in the excited state and rapid relaxation to the deprotonated ground state. When subtracting the UV/Vis spectrum of the $[Ru^{tBu}pyimH]^{2+}$ complex from that of its deprotonated congener, the spectrum in Figure 4d is obtained. This spectrum is very similar to the transient absorption spectrum in Figure 4c,

41

from which we conclude that in the time-resolved laser experiment the deprotonated complex in the ground state indeed accumulates. This effect is less pronounced for the complex with R = NMe$_2$, in which case the deprotonated ground state can only be detected after the excited stated has completely decayed (see the Supporting Information, Figure S11). Presumably, this is due to the weaker driving force for proton release in this case, and different complex–buffer interactions. The excited-state lifetimes are shortened by 50–90 % upon deprotonation (Table 2), ranging from 70 to 210 ns for the protonated forms and from 17 to 75 ns for the deprotonated forms, respectively, in the absence of oxygen. This effect can be explained by the energy-gap law and by mixing of pyim$^-$-based orbitals with metal-centered d-orbitals. As a consequence, the resulting excited state in the deprotonated complexes has a non-negligible ligand-to-ligand charge transfer character, and this can contribute to the lifetime shortening relative to the protonated complex.[34] The excited-state lifetimes under aerated conditions are reported in the Supporting Information (Table S3).
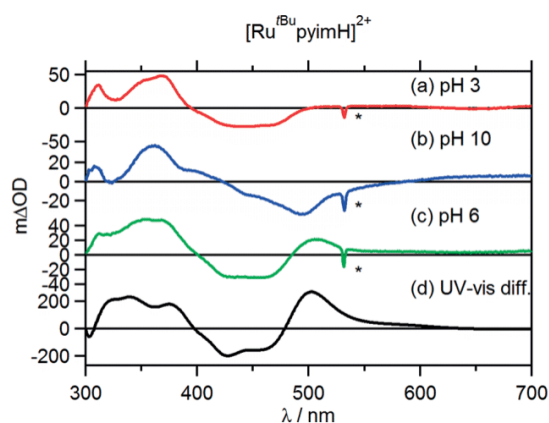
Table 2. Excited-state properties of [Ru^{R}pyimH]$^{2+}$ at 25 °C in 1:1 (v/v) CH$_3$CN/H$_2$O at luminescence maxima of protonated and deprotonated complexes (λ^{prot}, λ^{dep}) and lifetimes of protonated and deprotonated complexes (τ^{prot}, τ^{dep}) under deaerated conditions.

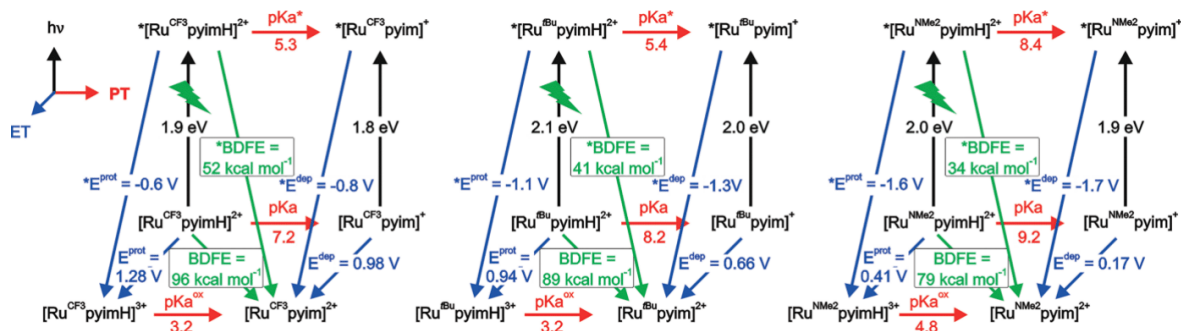| R	λ^{prot} [nm]	λ^{dep} [nm]	τ^{prot} [ns]	τ^{dep} [ns]
H[a]	625	675	210 ± 20	70 ± 7
CF$_3$[b]	670	708	160 ± 16	17 ± 5
tBu	625	683	140 ± 14	75 ± 8
NMe$_2$	675	692	70 ± 7	25 ± 2

[a] Taken from ref.[27] [b] Taken from ref.[41]

Formal N–H BDFEs

Based on the acidity constants and redox potentials in Table 1, formal N--H BDFEs were calculated from Equation (1); the results are listed in Table 3. The values obtained for the ground state were doubly determined by using pK_a and E^{dep} on the one hand, and pK_a^{ox} and E^{prot} on the other hand. Both sets of data were measured independently from each other, and ultimately they lead to an internally consistent picture. The BDFEs for the electronic excited states (*BDFE) were also doubly determined by using pK_a* and *E^{dep}, and by using pK_a^{ox} and *E^{prot}, respectively. The double determinations yielded the same BDFEs within experimental accuracy. The general observation is that for every complex the N–H bond cleavage is facilitated by ca. 50 kcal mol^{-1} in the excited state. The ground-state BDFEs are in the range from 79 ± 1 kcal mol^{-1} (R = NMe$_2$) to 96 ± 1 kcal mol^{-1} (R = CF$_3$), which is comparable in magnitude to the N–H BDFEs of primary and secondary amines.[35,49,50] Consequently, the BDFE can be tuned over a range of ca. 20 kcal mol^{-1} by substituent variation at the bpy spectator ligands. The complete thermochemistry regarding proton and electron transfer in ground and excited states is summarized in Scheme 2 in so-called "cube" schemes. In this representation, the ground-state redox potentials (E^{prot} and E^{dep}) for the protonated and deprotonated complexes are found at the bottom along with the acidity constants of the Ru^{II} and Ru^{III} species (pK_a and pK_a^{ox}). The bottom of Scheme 2 is, in fact, analogous to the thermodynamic square scheme for the cleavage of X–H bonds shown in Scheme 1. In Scheme 2, excitation to the ^{3}MLCT state is represented by vertical arrows for both the pro-

Figure 4. (a)–(c) Transient absorption spectra of [Ru^{tBu}pyimH]$^{2+}$ in 1:1 (v/v) CH$_3$CN/H$_2$O at different pH values. Excitation occurred at 532 nm with laser pulses of ca. 10 ns duration, the spectra were recorded without time delay over a period of 200 ns. (d) Difference of ground-state UV/Vis spectra of protonated and deprotonated complex. The asterisks mark laser stray light.

Table 3. X–H bond dissociation free energies in the ground (BDFE) and excited state (*BDFE) for some selected metal complexes, which can be considered formal H-atom donors.

Complex	BDFE [kcal mol^{-1}]	*BDFE [kcal mol^{-1}]	Ref.	Comment
[Ru^{H}pyimH]$^{2+}$	91 ± 1	43 ± 5	[27]	
[Ru^{CF3}pyimH]$^{2+}$	96 ± 1	52 ± 5	this work	
[Ru^{tBu}pyimH]$^{2+}$	89 ± 1	41 ± 5	this work	
[Ru^{NMe2}pyimH]$^{2+}$	79 ± 1	34 ± 5	this work	
[Ru(bpy)$_2$BiBzimH$_2$]$^{2+}$	90	42	[33,53,54]	[a,b]
[Ru(bpy)$_2$BiimH$_2$]$^{2+}$	86	40	[33,53,54]	[a,b]
[Os(bpy)$_2$BiBzimH$_2$]$^{2+}$	80	42	[33,53,54]	[a–c,e]
[Ru(hfacac)$_2$pyimH]$^{2+}$	80	–	[55]	
[Ru(bpy){(OH)$_2$-phen}$_2$]$^{2+}$	78	30	[56]	[a,b,d,f]

[a] BDFE calculated based on available redox potentials and acidity constants using both pathways illustrated in Scheme 1. [b] Excited-state bond dissociation free energies (*BDFEs) calculated based on available pK_a^{ox}, *E^{prot} values. [c] Redox potentials only in CH$_3$CN available. [d] pK_a^{ox} determined from the Nernst equation. [e] E_{00} = 1.66 eV, approximated from [Os(bpy)$_3$]$^{2+}$, as reported in ref.[57] [f] E_{00} = 2.1 eV approximated from [Ru(bpy)$_3$]$^{2+}$.[58]

$h\nu$ PT ET

[Ru^{CF3}pyimH]$^{2+}$ → pKa 5.3 → *[Ru^{CF3}pyim]$^{+}$

[Ru^{tBu}pyimH]$^{2+}$ → pKa 5.4 → *[Ru^{tBu}pyim]$^{+}$

[Ru^{NMe2}pyimH]$^{2+}$ → pKa 8.4 → *[Ru^{NMe2}pyim]$^{+}$

1.9 eV   1.8 eV   2.1 eV   2.0 eV   2.0 eV   1.9 eV

*BDFE = 52 kcal mol^{-1} *BDFE = 41 kcal mol^{-1} *BDFE = 34 kcal mol^{-1}

*E^{prot} = −0.6 V   *E^{dep} = −0.8 V   *E^{prot} = −1.1 V   *E^{dep} = −1.3 V   *E^{prot} = −1.6 V   *E^{dep} = −1.7 V

[Ru^{CF3}pyimH]$^{2+}$ → pKa 7.2 → [Ru^{CF3}pyim]$^{+}$

[Ru^{tBu}pyimH]$^{2+}$ → pKa 8.2 → [Ru^{tBu}pyim]$^{+}$

[Ru^{NMe2}pyimH]$^{2+}$ → pKa 9.2 → [Ru^{NMe2}pyim]$^{+}$

E^{prot} = 1.28 V   BDFE = 96 kcal mol^{-1} E^{dep} = 0.98 V

E^{prot} = 0.94 V   BDFE = 89 kcal mol^{-1} E^{dep} = 0.66 V

E^{prot} = 0.41 V   BDFE = 79 kcal mol^{-1} E^{dep} = 0.17 V

[Ru^{CF3}pyimH]$^{3+}$ → pKa^{ox} 3.2 → [Ru^{CF3}pyim]$^{2+}$

[Ru^{tBu}pyimH]$^{3+}$ → pKa^{ox} 3.2 → [Ru^{tBu}pyim]$^{2+}$

[Ru^{NMe2}pyimH]$^{3+}$ → pKa^{ox} 4.8 → [Ru^{NMe2}pyim]$^{2+}$

Scheme 2. Thermodynamic "cube" scheme for [Ru^{R}pyimH]$^{2+}$ in 1:1 (v/v) CH$_3$CN/H$_2$O based on the data in Tables 1 and 2. Horizontal/red: pK_a values, vertical/black: ^{3}MLCT energy E_{00}, pointing towards the reader in blue: oxidation potentials in V vs. SCE, diagonal in green: BDFEs.

tonated (E_{00}^{prot}) and deprotonated (E_{00}^{dep}) forms. In the excited state, the thermodynamically relevant processes are acid-base equilibration (pK_a*) (marked by a horizontal red arrow) and oxidation of the *Ru^{II} complexes to give the respective Ru^{III} complexes in the electronic ground state, as represented by blue face diagonals (*E^{prot}, *E^{dep}). The combined loss of a proton and an electron from the excited state is shown on the space diagonal from the back upper left corner to the lower front right corner, indicated by *BDFE (green arrows).

Thus, for the excited state of [Ru^{NMe2}pyimH]$^{2+}$ an exceptionally low *BDFE of 34 ± 5 kcal mol^{-1} is found, and this is caused by the strongly electron-donating NMe$_2$ groups, which lead to a low potential for metal oxidation. The inverse effect accounts for the behavior of [Ru^{CF3}pyimH]$^{2+}$, which has a relatively high *BDFE of 52 ± 5 kcal mol^{-1}. Nevertheless, even this *BDFE value is still in the order of magnitude reported for M–H cleavage in metal hydride catalysts that are used for thermal hydrogenation reactions.[37,51]

In summary, the N–H BDFEs in [Ru^{R}pyimH]$^{2+}$ complexes decrease with more electron-donating substituents on the bpy spectator ligands. A similar finding was reported for the ground-state N–H BDFEs of ruthenium(II)–2-(2-pyridyl)imidazole complexes when going from hexafluoroacetylacetonato (hfacac) to acetylacetonato (acac) spectator ligands, which lead to a decrease from 80 to 62 kcal mol^{-1}.[52]

The strong decrease of the N–H BDFEs upon photoexcitation to values below 60 kcal mol^{-1} is in line with our prior report on the [Ru^{R}pyimH]$^{2+}$ complex with R = H.[27] In principle, this effect is also expected for other metal complexes that can release both a proton and an electron in the ^{3}MLCT excited state, but to date such excited-state BDFEs have not been reported. Based on published acidity constants and redox potentials, we have tried to estimate some excited-state BDFEs for previously investigated complexes (Table 3), but these data should be considered with caution, because often different solvents were used for determination of pK_a values and redox potentials, and there are considerable uncertainties in their excited-state energies. The general observation is that excited-state BDFEs are in the range between 30 and 50 kcal mol^{-1}. As noted before and as evident from Equation (1), the changes in redox potential have more influence on the BDFE than changes of the acidity constants.[52]

Conclusions

All relevant thermodynamic parameters regarding proton-coupled oxidation, i.e., formal H-atom donation, were determined for three photoactive complexes in 1:1 (v/v) CH$_3$CN/H$_2$O. The key findings are: (i) Deprotonation of the studied complexes yields a gain in reducing power of 0.3 V in the ground state and 0.1–0.2 eV in the emissive excited state. (ii) The formal N–H BDFE can be tuned over a range of ca. 20 kcal mol^{-1} by varying the spectator ligands. (iii) Formal H-atom release is facilitated by roughly 50 kcal mol^{-1} upon excitation of these complexes to their long-lived ^{3}MLCT excites states, reaching excited-state BDFEs down to 34 kcal mol^{-1}. Thus, the photoexcited [Ru^{R}pyimH]$^{2+}$ complexes are very strong formal H-atom donors even when compared to metal hydride complexes that are used as hydrogenation catalysts.

Experimental Section

Methods and Equipment: All commercially available chemicals for synthesis were used as received. Acetonitrile for electrochemical and photophysical measurements was HPLC grade, and water had Millipore standard. Salts for buffers were used as received, and aqueous buffer solutions (0.1 M concentration) were prepared according to reported procedures.[59] The following buffers were used for the various pH ranges: TsOH/TsONa (pH 1.0–2.0), citric acid (pH 2.2–3.6), glycine/HCl (pH 2.2–3.6), acetate (pH 3.6–5.6), phosphate (pH 5.8–8.0), glycine/NaOH (pH 8.6–10.6), and phosphate (pH 11.0–12.0). Unless otherwise noted, all measurements were performed in 1:1 (v/v) CH$_3$CN/H$_2$O with a final buffer concentration of 0.05 M at 25 °C. The pH of the solvent mixture was determined by correcting the measured pH value (pH^{meas}) in the mixture by using the relationship pH = pH^{meas} − δ. For the 1:1 (v/v) CH$_3$CN/H$_2$O mixture, the correction constant δ is −0.257.[60] All pH values reported in this publication were corrected accordingly, and pK_a values taken from ref.[41] were also corrected accordingly. ^{1}H NMR spectra were measured with a 400 MHz Bruker Avance III instrument. UV/Vis spectra were measured with a Cary 5000 instrument from Varian. Cyclic voltammetry was performed with a Versastat3-200 potentiostat from Princeton Applied Research using a glassy carbon disk working electrode, a saturated calomel electrode as reference electrode, and a platinum wire was used as counter electrode, 0.05 M buffer served as supporting electrolyte. Prior to voltage sweeps at

43

rates of 0.1 V s^{-1}, the solutions were flushed with argon. For reversible cyclic voltammograms the average of reductive and oxidative peak potentials was used to determine the redox potential; for irreversible oxidations, the inflection point of the oxidative sweep was used as an approximation for the oxidation potential. Steady-state luminescence experiments were performed with a Fluorolog-3 apparatus from Horiba Jobin–Yvon. Samples were excited at wavelengths corresponding to the isosbestic points observed in acid-base titration experiments in Figures S2 and S3 of the Supporting Information. Luminescence lifetime and transient absorption experiments were conducted with an LP920-KS spectrometer from Edinburgh Instruments equipped with an iCCD detector from Andor. The excitation source was the frequency-doubled output from a Quantel Brilliant b laser. For aerated optical spectroscopic experiments, quartz cuvettes from Starna and Helma were used. For all deaerated optical spectroscopic experiments the samples were deoxygenated through three subsequent freeze–pump–thaw cycles in home-built quartz cuvettes that were specifically designed for this purpose. CCDC 1518357 {for [Ru^{NMe_2}pyimH](PF$_6$)$_2$} contains the supplementary crystallographic data for this paper. These data can be obtained free of charge from The Cambridge Crystallographic Data Centre.

[Ru{(tBu)$_2$bpy}$_2$pyimH](PF$_6$)$_2$ {[Ru^{tBu}pyimH](PF$_6$)$_2$}: The following procedure was applied based on a previously published protocol.[41] [Ru{(tBu)$_2$bpy}$_2$Cl$_2$] (177 mg, 250 μmol, 1.00 equiv.) was suspended at reflux in a degassed mixture of water (5 mL) and EtOH (5 mL). 2-(1H-Imidazol-2-yl)pyridine (44.0 mg, 305 μmol, 1.22 equiv.) was added, and the reaction mixture was heated to reflux for 3 h. After cooling to room temperature, a few drops of concentrated aq. HCl were added, and then ethanol was removed in vacuo. After addition of satd. aq. KPF$_6$ solution, the precipitate was filtered and washed with water and Et$_2$O. The solid was collected to give the product (193 mg, 180 μmol, 72 %) as an orange solid. ^{1}H NMR (300 MHz, CDCl$_3$): δ = 11.76 (s, 1 H), 8.30–8.10 (m, 6 H), 7.80 (td, J = 7.8, 1.4 Hz, 1 H), 7.73 (d, J = 6.0 Hz, 1 H), 7.69–7.57 (m, 4 H), 7.49 (dd, J = 6.1, 2.0 Hz, 1 H), 7.46–7.37 (m, 3 H), 7.32 (ddd, J = 7.3, 5.7, 1.3 Hz, 1 H), 7.25 (s, 1 H), 6.43 (s, 1 H), 1.41 (d, J = 6.3 Hz, 36 H) ppm. C$_{44}$H$_{55}$F$_{12}$N$_7$P$_2$Ru (1072.97): calcd. C 49.25, H 5.17, N 9.14; found C 49.32, H 4.95, N 9.01. ESI-HRMS: calcd. for [C$_{78}$H$_{67}$N$_9$O$_4$Ru]$^{2+}$ 391.6782; found 391.6777.

[Ru{(NMe$_2$)$_2$bpy}$_2$pyimH](PF$_6$)$_2$ {[Ru^{NMe_2}pyimH](PF$_6$)$_2$}: The following procedure was applied based on a previously published protocol.[40] A degassed mixture of [Ru{(NMe$_2$)$_2$bpy}$_2$Cl$_2$]Cl·4H$_2$O (100 mg, 131 μmol, 1.00 equiv.), 2-(1H-imidazol-2-yl)pyridine (74.0 mg, 510 μmol, 3.89 equiv.) and NEt$_3$ (0.2 mL) in water (5 mL) and EtOH (5 mL) was heated to reflux for 7 h. After cooling to room temperature, satd. aq. NH$_4$PF$_6$ solution (0.5 mL) was added. Some solvent was evaporated in vacuo, and the precipitate was filtered and washed with water. The obtained solid was purified by column chromatography (SiO$_2$; acetone → acetone/H$_2$O/satd. aq. KNO$_3$, 100:10:1). The solvent of the red phase was removed in vacuo, and 0.1 M acetate buffer (pH 5, 10 mL) and satd. aq. KPF$_6$ solution were added sequentially. The organic solvent was removed in vacuo, and the precipitate was collected by filtration. The product (65 mg, 63.7 μmol, 48 %) was obtained as a red solid. ^{1}H NMR (400 MHz, CD$_3$CN): δ = 11.80 (s, 1 H), 8.03 (d, J = 7.9 Hz, 1 H), 7.86 (t, J = 7.7 Hz, 1 H), 7.79 (d, J = 5.6 Hz, 1 H), 7.47 (d, J = 7.3 Hz, 4 H), 7.39 (s, 1 H), 7.28 (d, J = 6.5 Hz, 2 H), 7.18 (m, 3 H), 6.62–6.41 (m, 5 H), 3.10 (m, 24 H) ppm. C$_{36}$H$_{43}$F$_{12}$N$_{11}$P$_2$Ru·0.75CH$_3$COCH$_3$·2.5H$_2$O (1109.37): calcd. C 41.41, H 4.77, N 13.89; found C 41.45, H 4.78, N 13.91. ESI-HRMS: calcd. for [C$_{36}$H$_{43}$F$_{12}$N$_{11}$P$_2$Ru]$^{2+}$ 365.6368; found 365.6371.

[1] C. R. Bock, T. J. Meyer, D. G. Whitten, *J. Am. Chem. Soc.* **1974**, *96*, 4710–4712.

[2] R. Bensasson, C. Salet, V. Balzani, *J. Am. Chem. Soc.* **1976**, *98*, 3722–3724.

[3] C. K. Prier, D. A. Rankic, D. W. C. MacMillan, *Chem. Rev.* **2013**, *113*, 5322–5363.

[4] H. Huo, X. Shen, C. Wang, L. Zhang, P. Röse, L.-A. Chen, K. Harms, M. Marsch, G. Hilt, E. Meggers, *Nature* **2014**, *515*, 100–103.

[5] L. A. Büldt, X. Guo, A. Prescimone, O. S. Wenger, *Angew. Chem. Int. Ed.* **2016**, *55*, 11247–11250.

[6] S. Berardi, S. Drouet, L. Francàs, C. Gimbert-Suriñach, M. Guttentag, C. Richmond, T. Stoll, A. Llobet, *Chem. Soc. Rev.* **2014**, *43*, 7501–7519.

[7] L. Hammarström, *Acc. Chem. Res.* **2015**, *48*, 840–50.

[8] J. L. Fillol, Z. Codolà, I. Garcia-Bosch, L. Gómez, J. J. Pla, M. Costas, *Nat. Chem.* **2011**, *3*, 807–813.

[9] C. J. Gagliardi, B. C. Westlake, C. A. Kent, J. J. Paul, J. M. Papanikolas, T. J. Meyer, *Coord. Chem. Rev.* **2010**, *254*, 2459–2471.

[10] E. C. Gentry, R. R. Knowles, *Acc. Chem. Res.* **2016**, *49*, 1546–1556.

[11] K. T. Tarantino, P. Liu, R. R. Knowles, *J. Am. Chem. Soc.* **2013**, *135*, 10022–10025.

[12] M. Zhang, T. Irebo, O. Johansson, L. Hammarström, *J. Am. Chem. Soc.* **2011**, *133*, 13224–13227.

[13] O. S. Wenger, *Acc. Chem. Res.* **2013**, *46*, 1517–1526.

[14] M. Sjödin, S. Styring, H. Wolpher, Y. Xu, L. Sun, L. Hammarström, *J. Am. Chem. Soc.* **2005**, *127*, 3855–3863.

[15] M. Sjödin, S. Styring, B. Åkermark, L. Sun, L. Hammarström, *J. Am. Chem. Soc.* **2000**, *122*, 3932–3936.

[16] A. Magnuson, H. Berglund, P. Korall, L. Hammarström, B. Åkermark, S. Styring, L. Sun, *J. Am. Chem. Soc.* **1997**, *119*, 10720–10725.

[17] P. Dongare, S. Maji, L. Hammarström, *J. Am. Chem. Soc.* **2016**, *138*, 2194–2199.

[18] G. F. Manbeck, E. Fujita, J. J. Concepcion, *J. Am. Chem. Soc.* **2016**, *138*, 11536–11549.

[19] J. Chen, M. Kuss-Petermann, O. S. Wenger, *J. Phys. Chem. B* **2015**, *119*, 2263–2273.

[20] H. G. Yayla, R. Knowles, *Synlett* **2014**, *25*, 2819–2826.

[21] J. Nomrowski, O. S. Wenger, *Inorg. Chem.* **2015**, *54*, 3680–3687.

[22] T. T. Eisenhart, J. L. Dempsey, *J. Am. Chem. Soc.* **2014**, *136*, 12221–12224.

[23] B. C. Westlake, M. K. Brennaman, J. J. Concepcion, J. J. Paul, S. E. Bettis, S. D. Hampton, S. A. Miller, N. V. Lebedeva, M. D. E. Forbes, A. M. Moran, T. J. Meyer, J. M. Papanikolas, *Proc. Natl. Acad. Sci. USA* **2011**, *108*, 8554–8558.

[24] O. S. Wenger, *Coord. Chem. Rev.* **2015**, *282–283*, 150–158.

[25] J. C. Freys, G. Bernardinelli, O. S. Wenger, *Chem. Commun.* **2008**, 4267–4269.

[26] C. Bronner, O. S. Wenger, *Inorg. Chem.* **2012**, *51*, 8275–8283.

[27] A. Pannwitz, O. S. Wenger, *Phys. Chem. Chem. Phys.* **2016**, *18*, 11374–11382.

[28] C. Bronner, O. S. Wenger, *J. Phys. Chem. Lett.* **2012**, *3*, 70–74.

[29] S. M. Barrett, C. L. Pitman, A. G. Walden, A. J. M. Miller, *J. Am. Chem. Soc.* **2014**, *136*, 14718–14721.

[30] D. R. Weinberg, C. J. Gagliardi, J. F. Hull, C. F. Murphy, C. A. Kent, B. C. Westlake, A. Paul, D. H. Ess, D. Granville, T. J. Meyer, *Chem. Rev.* **2012**, *112*, 4016–4093.

[31] J. J. Concepcion, M. K. Brennaman, J. R. Deyton, N. V. Lebedeva, M. D. E. Forbes, J. M. Papanikolas, T. J. Meyer, *J. Am. Chem. Soc.* **2007**, *129*, 6968–6969.

45

Full Paper

[32] N. V. Lebedeva, R. D. Schmidt, J. J. Concepcion, M. K. Brennaman, I. N. Stanton, M. J. Therien, T. J. Meyer, M. D. E. Forbes, *J. Phys. Chem. A* **2011**, *115*, 3346–3356.

[33] M.-A. Haga, *Inorg. Chim. Acta* **1983**, *75*, 29–35.

[34] K. M. Lancaster, J. B. Gerken, A. C. Durrell, J. H. Palmer, H. B. Gray, *Coord. Chem. Rev.* **2010**, *254*, 1803–1811.

[35] J. J. Warren, T. A. Tronic, J. M. Mayer, *Chem. Rev.* **2010**, *110*, 6961–7001.

[36] C. R. Waidmann, A. J. M. Miller, C.-W. A. Ng, M. L. Scheuermann, T. R. Porter, T. A. Tronic, J. M. Mayer, *Energy Environ. Sci.* **2012**, *5*, 7771–7780.

[37] J. Choi, M. E. Pulling, D. M. Smith, J. R. Norton, *J. Am. Chem. Soc.* **2008**, *130*, 4250–4252.

[38] E. F. Van Der Eide, M. L. Helm, E. D. Walter, R. M. Bullock, *Inorg. Chem.* **2013**, *52*, 1591–1603.

[39] S. Anderson, E. C. Constable, K. R. Seddon, J. E. Turp, J. E. Baggott, M. J. Pilling, *J. Chem. Soc., Dalton Trans.* **1985**, 2247–2261.

[40] S. J. Slattery, N. Gokaldas, T. Mick, K. A. Goldsby, *Inorg. Chem.* **1994**, *33*, 3621–3624.

[41] R. Hönes, M. Kuss-Petermann, O. S. Wenger, *Photochem. Photobiol. Sci.* **2013**, *12*, 254–261.

[42] T. Ben Hadda, H. Le Bozec, *Polyhedron* **1988**, *7*, 575–577.

[43] R. F. Carina, L. Verzegnassi, G. Bernardinelli, A. F. Williams, *Chem. Commun.* **1998**, 2681–2682.

[44] H. Jones, M. Newell, C. Metcalfe, S. E. Spey, H. Adams, J. A. Thomas, *Inorg. Chem. Commun.* **2001**, *4*, 475–477.

[45] M. J. Fuentes, R. J. Bognanno, W. G. Dougherty, W. J. Boyko, W. Scott Kassel, T. J. Dudley, J. J. Paul, *Dalton Trans.* **2012**, *41*, 12514–12523.

[46] S. Klein, W. G. Dougherty, W. S. Kassel, T. J. Dudley, J. J. Paul, *Inorg. Chem.* **2011**, *50*, 2754–2763.

[47] L. M. Tolbert, K. M. Solntsev, *Acc. Chem. Res.* **2002**, *35*, 19–27.

[48] R. M. O'Donnell, R. N. Sampaio, G. Li, P. G. Johansson, C. L. Ward, G. J. Meyer, *J. Am. Chem. Soc.* **2016**, *138*, 3891–3903.

[49] F. G. Bordwell, X. Zhang, J. P. Cheng, *J. Org. Chem.* **1991**, *56*, 3216–3219.

[50] F. G. Bordwell, X. M. Zhang, J. P. Cheng, *J. Org. Chem.* **1993**, *58*, 6410–6416.

[51] M. Bourrez, R. Steinmetz, S. Ott, F. Gloaguen, L. Hammarström, *Nat. Chem.* **2015**, *7*, 140–145.

[52] A. Wu, J. Masland, R. D. Swartz, W. Kaminsky, J. M. Mayer, *Inorg. Chem.* **2007**, *46*, 11190–11201.

[53] A. M. Bond, M. Haga, *Inorg. Chem.* **1986**, *25*, 4507–4514.

[54] D. P. Rillema, R. Sahai, P. Matthews, A. K. Edwards, R. J. Shaver, L. Morgan, *Inorg. Chem.* **1990**, *29*, 167–175.

[55] A. Wu, J. M. Mayer, *J. Am. Chem. Soc.* **2008**, *130*, 14745–14754.

[56] S. M. Zakeeruddin, D. M. Fraser, M.-K. Nazeenruddin, M. Grätzel, *J. Electroanal. Chem.* **1992**, *337*, 253–283.

[57] A. A. Vlcek, E. S. Dodsworth, W. J. Pietro, A. B. P. Lever, *Inorg. Chem.* **1995**, *34*, 1906–1913.

[58] A. Juris, V. Balzani, F. Barigelletti, S. Campagna, P. Belser, A. von Zelewsky, *Coord. Chem. Rev.* **1988**, *84*, 85–277.

[59] D. D. Perrin, B. Dempsey, *Buffers for pH and Metal Ion Control*, Chapman And Hall, London, **1979**.

[60] L. G. Gagliardi, C. B. Castells, C. Ràfols, M. Rosés, E. Bosch, *Anal. Chem.* **2007**, *79*, 3180–3187.

45

3 Double-PCET in a Molecular Triad as Photosystem II Mimic with Long-Living Radical Separated State

3.1 Abstract

The investigated donor-photosensitizer-acceptor assembly is based on a phenol as combined electron and proton donor, a $[Ru(bpy)_3]^{2+}$-type photosensitizer and a 4,4'-bipyridinium proton and electron acceptor as shown in Figure 3-1. The photochemically generated radicals are separated by 20 Å. They are formed via two PCETs which mimics enzymatic long-range charge transfer more closely than any reported molecular model system.
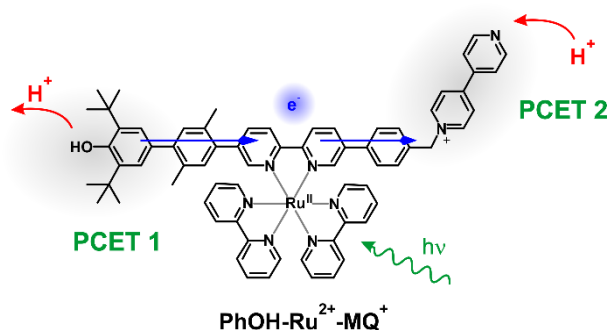

Figure 3-1 The investigated triad with a $[Ru(bpy)_3]^{2+}$-type photosensitizer and photoinduced PCET at the phenol (PCET 1) and monoquat unit (PCET 2).

This chapter is structured into *Main Article* and *Supporting Information*, and will be the basis for a manuscript for publication.
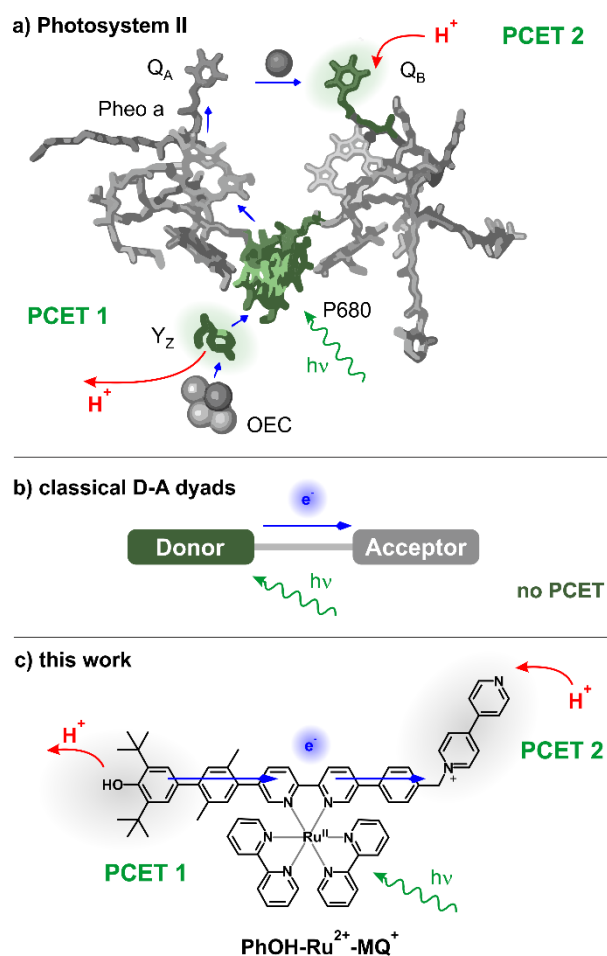
3.2 **Main Article**

Figure 3-2 a) Electron transfer chain in photosystem II, with ET to Pheophytin a (Pheo a) and PCET at Tyrosine Z (Y_Z, PCET 1) and plastoquinone B (Q_B, PCET 2). b) Previously investigated electron-donor acceptor (D-A) systems usually do not involve PCET and mimic ET from P680 to one of the acceptors in the electron transfer chain of PS II. c) Investigated triad with photoinduced PCET at the phenol (PCET 1) and monoquat unit (PCET 2) resembles radical transfer from Y_Z to Q_B.

Photoinduced charge transfer in molecular systems is efficiently performed in photosynthesis, namely by the membrane bound enzyme complexes photosystem I and II (PSI, PS II). Visible light is used as energy resource for the transfer of electrons from the oxidative site to the reducing side of the membrane. In PS II, light is absorbed by the chlorophyll-dimer P680 which is the central part and photosensitizer in the electron transfer chain, as shown in Figure 3-2a.[8] All electron donors and acceptors are pre-arranged by the protein structure of PS II. Upon excitation, P680 donates an electron to the neighboring Pheophytin a (Pheo a) which subsequently reduces plastoquinone A (Q_A). The electron is further transferred to plastoquinone B (Q_B) which subsequently takes up a proton and diffuses to the next acceptor after uptake of a

second electron and proton. The oxidized P680 abstracts an electron from the nearby tyrosine Z (Y_Z) which subsequently oxidizes the water oxidizing complex (OEC). Tyrosine Z is deprotonated upon oxidation which sums up two proton-coupled electron transfers (PCET) in PS II.[26,27] The respective charge-neutral radicals $Y_Z^\bullet$ and $HQ_B^\bullet$ are generated 40 Å apart from one each other.[28]

The concept of photoinduced long-range charge transfer was mimicked numerously in covalently linked donor-acceptor assemblies (D-A), which are sketched in Figure 1b. Excitation of such compounds with visible light induces intramolecular electron transfer (ET), yielding D^+ and A^-.[29] This simple ET resembles photoinduced ET from P680 to one of the acceptors in the electron transfer chain of PS II. The importance of PCET is usually ignored in such artificial model systems. PCET is performed by enzymes, because deprotonation of electron donors facilitates their oxidation whereas protonation of acceptors facilitates their reduction. Photoinduced single PCET in dyads has been demonstrated with proton-coupled oxidation of phenols.[30–38] However, two-fold PCET, as described above in PS II, has not yet been studied in model systems. By mimicking photoinduced PCET 1 at the Y_Z in combination with PCET 2 at Q_B we generate radical separated states, similar to PS II. Our model system is presented in Figure 1c. It consists of a molecular triad (**PhOH-Ru^{2+}-MQ$^+$**) with a Ru(bpy)$_3^{2+}$-type photosensitizer. The covalently linked 2,6-di-*tert*-butylphenol (PhOH) acts as a combined electron and proton donor whereas *N*-methyl-4,4' bipyridinium (MQ$^+$) serves as a combined proton and electron acceptor. The aryl bridges provide a rigid scaffold for the arrangement of PhOH donor, Ru(bpy)$_3^{2+}$ photosensitizer, and MQ$^+$ acceptor guaranteeing a donor-acceptor distance of approximately 22 Å.[39] Excitation of the Ru(bpy)$_3^{2+}$ center induces proton-coupled oxidation of PhOH (PCET 1) and proton-coupled reduction of MQ$^+$ (PCET 1), generating the radical pair PhO$^\bullet$ and HMQ$^{\bullet+}$ according to the following equation:

$$\textbf{PhOH-Ru}^{2+}\textbf{-MQ}^+ \quad \rightarrow \quad \textbf{PhO}^\bullet\textbf{-Ru}^{2+}\textbf{-HMQ}^{\bullet+} \tag{3-1}$$
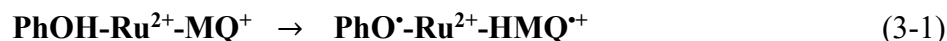
PCET 1 and PCET 2 at **PhOH-Ru(II)-MQ$^+$** require the presence of external acid and base, hence an amphoteric solvent or a buffer. A suitable buffer deprotonates the phenol only upon photoinduced oxidation and protonates the MQ$^+$ acceptor only upon reduction. Based on available acidity constants, pyridine (py) and pyridinium (pyH$^+$) match these requirements (thermochemical discussion see Supporting Information). PCET at the phenol is most efficient, when the phenolic O-H is hydrogen bound to the base.[19,40,41] The design of the triad does not include any intramolecular hydrogen bonds opposed to other model systems.[17,38,42–45] Association constants for the formation of intermolecular hydrogen bonds between phenols and

pyridine are usually small in commonly used solvents such as acetonitrile. They might be reduced by the sterically demanding *tert*-butyl groups, that shield the phenolic proton.[19] Therefore, high concentration of pyridine is necessary, to achieve quantitative hydrogen bonding to the PhOH donor of the triad. Neat pyridine as solvent ensures almost quantitative hydrogen bonding of the phenolic protons to pyridine, as discussed in the Supporting Information.[19]
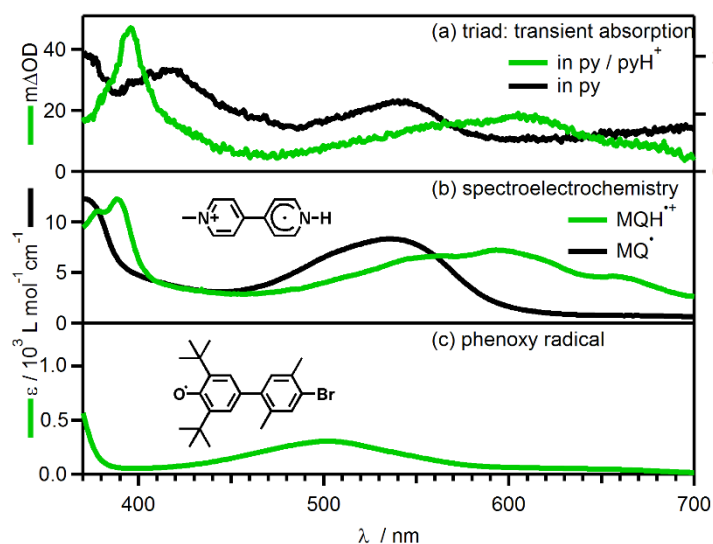

Figure 3-3 a) Transient absorption spectra of 34 µM triad in pyridine/ 0.22 M pyridinium buffer (green traces) and of 55 µM triad in neat pyridine (gray traces). Both spectra are recorded 2 µs after excitation at 532 nm with pulses of ~10 ns duration. b) Electrochemically generated spectra of HMQ$^{\bullet+}$ and MQ$^{\bullet}$ in MeCN with 0.1 M TBAPF$_6$ as supporting electrolyte. Extinction coefficients are derived from previous studies.[46] c) Spectrum of chemically generated phenoxy radical PhO$^{\bullet}$-xy-TMS in toluene.
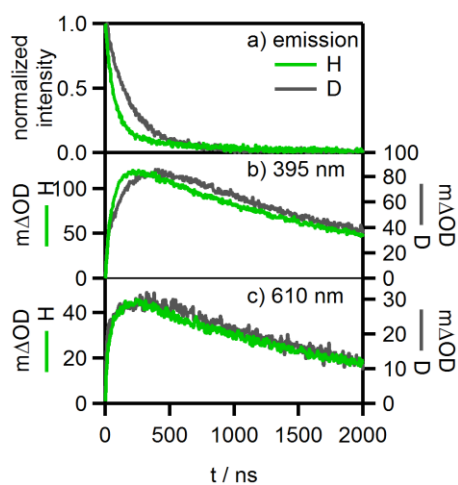

Figure 3-4 Kinetic traces of 34 µM triad in py with 0.22 M pyH$^+$ or pyD$^+$ recorded after pulsed excitation at 532 nm with laser pulses of ~10 ns duration. The same traces at a longer time-scale are shown in the Supporting Information. a) Emission traces recorded at 630 nm. b) Absorbance at 395 nm. c) Absorbance at 610 nm.

In pyridine (py) as solvent with 0.22 M pyridinium (pyH$^+$), the luminescence of photoexcited Ru(bpy)$_3^{2+}$-unit in the triad is quenched and a long-living photoproduct is formed, shown at 2 µs after pulsed excitation at 532 nm in Figure 3-3a. The excited state decays biexponentially with $\tau = 68 \pm 7$ ns (85 %) and $\tau' = 780 \pm 80$ ns (15 %). The faster component is related to the prominent transient absorption signals at 395 nm and 610 nm, which rise with $\tau^{rise} = 68 \pm 7$ ns and decay with $\tau^{dec} = 1.9 \pm 0.2$ µs as shown in Scheme 1-4 and summarized in Table 1. The slower luminescent component is due to a subset of slower decaying excited state, or different luminescent species from ligand exchange to pyridine. The transient absorption spectrum resembles the spectrum of the well-known radical of methyl viologen (N,N'-dimethyl-4,4'bipyridine, MV^{2+}).[46] Protonation and reduction of the MQ$^+$ acceptor generates a spectrum similar to the methyl viologen radical.[47,48] We therefore assume to have obtained the spectrum of HMQ$^{•+}$. For direct verification of the spectroscopic signature of the radical separated state (**PhO$^•$-Ru^{2+}-HMQ$^{•+}$**), we recorded UV/Vis absorption of radical species from reference compounds. The spectrum of HMQ$^{•+}$ was obtained by electrochemical reduction of protonated N-methyl-4,4'-bipyridine in acetonitrile and is shown as green trace in Figure 3-3b. It is in line with previous studies and with the transient absorption spectrum of the triad in py/pyH$^+$ buffer.[47,48] The reference spectrum for PhO$^•$ was generated by chemical oxidation of PhOH-xy-TMS (3,5-di-tert-butyl-2',5'-dimethyl-4'-(trimethylsilyl)-[1,1'-biphenyl]-4-ol) with ferricyanide under basic conditions, yielding the phenoxy radical (PhO$^•$).[49] It shows a band maximum at 507 nm which is in line with reported related phenoxy radical spectra.[49,50] Its estimated extinction coefficient is 500 L^{-1} mol cm^{-1},[49,50] whereas the estimated extinction coefficient of MQH$^{•+}$ is approximately 5000 L^{-1} mol cm^{-1} at this wavelength.[46] Hence, absorption of HMQ$^{•+}$ is much stronger than absorption of the PhO$^•$ and therefore MQH$^{•+}$ dominates the spectrum of the radical separated state in Figure 3-3a (green trace).

Because we can only hypothesize the formation of PCET 1 product PhO$^•$, we will show in the following, that the phenol is oxidized and deprotonated in py with 0.22 M pyH$^+$ despite its weak signature in the spectrum. If the phenol was not involved in the photochemistry of **PhOH-Ru^{2+}-MQ$^+$**, the functional units of the molecule would merely be the Ru(bpy)$_3^{2+}$ photosensitizer and the MQ$^+$ radical acceptor. These two functional units are a donor-acceptor assembly with one possible PCET. Similar dyads with MV^{2+} acceptors and Ru(bpy)$_3^{2+}$ photosensitizers were reported to have charge separated state lifetimes in the order of few ps to less than 10 ns.[51–55] In contrast, the photoproduct observed in Figure 3-3a has a lifetime on the order of a few µs.

Similar triads, with central Ru(bpy)$_3^{2+}$ photosensitizer, triaryl amine donor and anthraquinone acceptor separated by similar distances, have charge separated state lifetimes in the μs time regime as well, which indicates that **PhOH-Ru^{2+}-MQ$^+$** also acts as a triad.[39,56]

To further probe the role of the phenol, photoinduced radical transfer was monitored after pulsed excitation at 532 nm in neat pyridine. Absence of acid excludes protonation of the (reduced) MQ$^+$ acceptor and therefore it excludes PCET 2, whereas pure electron transfer to MQ$^+$ is still possible based on the relevant reduction potentials (see SI). In neat pyridine, ^{3}MLCT luminescence is quenched to $\tau = (35 \pm 4)$ ns (89 %) and $\tau = (1.2 \pm 1)$ μs (11 %). Long living photoproducts are formed with $\tau = (35 \pm 4)$ ns. The transient absorption spectrum of the photoproduct 2 μs after pulsed excitation is shown in Figure 3-3a as grey trace. The bands at around 370 nm and 550 nm resemble the signature of MQ$^\bullet$, which is the reduced acceptor. A reference spectrum of spectroelectrochemically generated MQ$^\bullet$ in acetonitrile is shown as grey trace in Figure 3-3b. It is in agreement with reported spectra of MQ$^\bullet$.[46,48] The band at 420 nm is assigned to the deprotonated phenol based on the difference spectrum derived upon deprotonation of **PhOH-Ru^{2+}-MQ$^+$** with TBAOH (see Figure S 3-8 and Figure S 3-9). The band at 420 nm is very long-living and decays with $\tau^{420} = 18$ μs which is more persistent than the MQ$^\bullet$ signature which decays with $\tau = 3.0 \pm 0.3$ μs. In the absence of acid, the phenolate is the secondary photoproduct which is formed after intramolecular thermal reverse electron transfer from MQ$^\bullet$ to the phenoxy radical (**PhO$^\bullet$-Ru^{2+}-MQ$^\bullet$ → PhO$^-$-Ru^{2+}-MQ$^+$**). Additionally, thermal recombination of the transiently formed species **PhO$^\bullet$-Ru$^+$- MQ$^+$** is expected to be fast as reported earlier for closely related dyads.[32,34,36] However, at low proton concentration protonation of the phenolate is extremely slow, which makes it very long-living. Based on thermochemical calculations (see Supporting Information for details), the most probable way the observed MQ$^\bullet$ species is formed, is via reductive quenching of ^{3}MLCT excited Ru(bpy)$_3^{2+}$ photosensitizer by the phenol. The resulting Ru(I)(bpy)$_3^+$ can easily reduce the MQ$^+$ acceptor with a driving force of approximately -0.5 eV. In absence of acid, oxidative quenching by MQ$^+$ is approximately thermoneutral compared to the excited state.[48,57,58] ET from PhOH to ^{3}MLCT Ru(bpy)$_3^{2+}$ is exergonic only when coupled to deprotonation of PhOH.[10,57] For similar PhOH-Ru^{2+} dyads it is reported, that intramolecular ET from phenol to photoexcited Ru(bpy)$_3^{2+}$ takes place in presence of base via concerted PCET (CPET).[36,59] The phenolate form of the molecule as secondary photoproduct was found in these studies as well as for **PhOH-Ru^{2+}-MQ$^+$** under basic conditions. The observation of the phenolate species shows that PCET takes place at the PhOH and that the electron for the reduction of the acceptor originates from the phenol.

In neat acetonitrile, solvent mediated PT is not posible and consequently only simple ET reactions are expected. However, the observed long-living product after photoexcitation of **PhOH-Ru^{2+}-MQ$^+$** is the ^{3}MLCT state of the photosensitizer[39] with a luminescence lifetime of τ = (900 ± 90) ns. Based on thermochemical calculations, photoinduced ET to MQ$^+$ is thermoneutral. The associated error range of these calculations do not exclude it completely. However, it is not observed spectroscopically. Transient absorption and luminescence spectra of the triad in acetonitrile are shown in the Supporting Information (Figure S 3-10 to Figure S 3-12). These experiments show the importance of the buffer for the excited state redox chemistry of **PhOH-Ru^{2+}-MQ$^+$**.

Table 3-1 Lifetimes of relevant processes under de-aerated conditions at 25 °C.

solvent	py / pyH$^+$	py / pyD$^+$	py
^{3}MLCT decay rise times of photoproduct	68 ± 7 ns	150 ± 15 ns	35 ± 4 ns
lifetime of radical separated state	1.9 ± 0.2 μs	1.8 ± 0.2 μs	3.0 ± 0.3 μs
lifetime of phenolate			18 ± 2 μs

PCET was further probed with kinetic H/D exchange experiments in py/pyH$^+$ buffer. In py with 0.22 M pyD$^+$ it was found that the main luminescent species decays with τ_D = 150 ± 15 ns, which is by factor (2.2 ± 0.2) slower than in py with 0.22 M pyH$^+$ (68 ± 7) ns. The minor species decays with τ_D' = 380 ± 38 ns, which is faster by factor two. Formation of the final photoproduct in transient absorption under deuterated conditions takes place with τ_D^{rise} = 150 ± 15 ns referring to a H/D kinetic isotope effect (KIE) of (2.2 ± 0.2), comparable to the luminescence decay. Recombination of the photoproducts under deuterated conditions takes place with τ_D^{dec} = 1.8 μs, corresponding to a H/D KIE of 0.9 +/0.2. The fact that the time constant for luminescence decay of the main species corresponds to the formation of the photoproduct implies that initial quenching of the ^{3}MLCT- excited photosensitizer is followed by subsequent PCET on the sub-ns time scale to form the radical separated state. The H/D KIE of (2.2 ± 0.2) shows that proton transfer is involved in the rate limiting step, hence ^{3}MLCT quenching via CPET is evident.

Based on thermochemical calculations (energy level scheme in Figure S 3-17 to Figure S 3-19) initial concerted PCET at the PhOH via reductive ^{3}MLCT quenching is estimated to have the same driving force as oxidative ^{3}MLCT quenching via concerted PCET at the MQ$^+$ (of ΔG_{PCET} = -0.2 eV). For initial reductive quenching of ^{3}MLCT Ru(bpy)$_3^{2+}$ via PCET 1 at the

PhOH, the follow-up reduction of MQ^+ is exergonic by approximately ΔG_{ET} = -0.5 eV, in agreement with an ET-PT mechanism. For initial oxidative ^{3}MLCT quenching and PCET 2 at the MQ^+, the follow-up oxidation of the PhOH is likely to occur in concert with deprotonation (CPET with (ΔG_{PCET} = -0.7 eV) as demonstrated for a similar PhOH-Ru^{2+} dyad in a flash-quench experiment and as found for phenols several times before.[19,30,32,34–36]

In py/pyH$^+$ it is theoretically possible that only one of the PCETs takes place because one PCET site is protonated or deprotonated in advance due to protonation and deprotonation equilibria. We wish to comment on this in the following. The acidity constants (pK$_a$) of pyridine, PhOH and MQ^+ or their respective acids are known in water. [10,48,60] The difference in acidity of PhOH and pyH$^+$ is reasonably high to assume that no deprotonation of the PhOH by pyridine takes place at equimolar concentration. However, at the given concentrations, up to 8 % of the triad molecules might be deprotonated in neat pyridine, as calculated in the Supporting Information. On the other hand, the UV-vis absorption spectrum of the triad in pyridine shows only minor differences to the spectrum in acetonitrile (Figure S 3-13). Furthermore, photoinduced radical separation in pyridine shows phenolate as secondary reaction product, therefore indicating that deprotonation occurs only after photoexcitation. We therefore assume that the observed photoproducts derive from PCET at **PhOH-Ru^{2+}-MQ$^+$** as major species. We exclude protonation of MQ^+ by pyH$^+$ because py is a stronger base and in the reaction mixture six orders of magnitude more concentrated than the triad.

The absence of a significant KIE in the radical recombination indicates ET as the rate limiting step. This is in line with thermochemical calculations where intramolecular ET **PhO$^•$-Ru^{2+}-MQH$^{•+}$ → PhO$^-$-Ru^{2+}-MQH^{2+}** is exergonic by approximately 0.6 eV (see Supporting Information for details). No spectral evidence of MQH^{2+} and PhO$^-$ was found under buffered conditions, indicating that the follow-up twofold PT to reestablish ground state **PhOH-Ru^{2+}-MQ$^+$** is fast.

In summary, two opposing, photoinduced PCETs were performed on the same molecule, transferring a radical over approximately 30 Å. The photo-generated radical pair is similarly long-lived as electron-hole pairs in triads. For the first time, the electron-hole pair is stabilized by *two* PCET events, which successfully mimics photoinduced primary and secondary ET and PCET events of PS II in a simple artificial system.

3.3 Supporting Information

3.3.1 Equipment and Methods

All commercially available chemicals for synthesis were used as received. Acetonitrile for electrochemical and photophysical measurements was HPLC grade. Steady-state luminescence experiments were performed on a Fluorolog-3 apparatus from Horiba Jobin-Yvon. Luminescence lifetime and transient absorption experiments occurred on an LP920-KS spectrometer from Edinburgh Instruments equipped with an iCCD detector from Andor. If not otherwise noted, the excitation source was the frequency-doubled output from a Quantel Brilliant b laser. For all deaerated optical spectroscopic experiments the samples were de-oxygenated via two subsequent freeze–pump–thaw cycles in quartz cuvettes that were specifically designed for this purpose. UV-vis spectra of electrochemically generated species were recorded with the Cary 5000 instrument by applying voltage with a Versastat3-200 potentiostat, using a platinum gauze electrode as working electrode, a saturated calomel electrode (SCE) as reference electrode, and a platinum wire as counter electrode. The substance was dissolved in MeCN with 0.1 M TBAPF$_6$ as supporting electrolyte and the suitable potential was applied in a spectroelectrochemical cell from *ALS* with 1 mm path length. Potentials for electrolysis were determined by cyclic voltammetry. The following experimental errors are considered: Excited state lifetimes were considered accurate to 10 %, and ground state redox potentials are considered accurate to $\pm$ 0.05 V. UV-Vis spectra were measured on a Cary 5000 instrument from Varian. Cyclic voltammetry was performed on a Versastat3-200 potentiostat from Princeton Applied Research using a glassy carbon disk working electrode, a saturated calomel electrode (SCE) as reference electrode, and a platinum wire as counter electrode. Prior to voltage sweeps at rates of 0.1 V s^{-1}, the solutions were flushed with argon. For quasi-reversible cyclic voltammograms the average of reductive and oxidative peak potential was used to determine the redox potential, for irreversible processes the peak potential is reported.
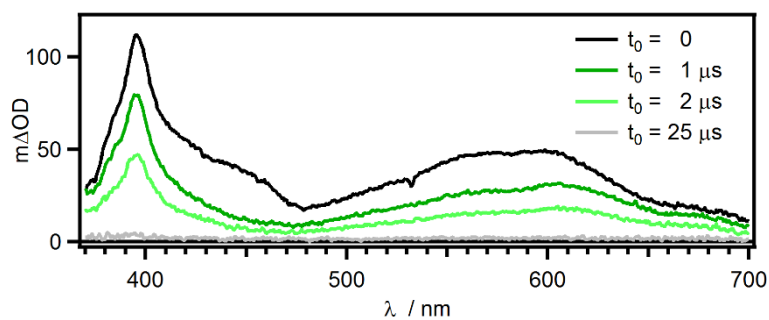
3.3.2 Kinetic Traces and Transient Absorption Spectra in py/0.22M pyH$^+$

Figure S 3-1 Transient absorption spectra of 34 µM triad in py / 0.22 M pyH$^+$ buffer. Signal integration occurred over 200 ns at different delay times (t_0) after excitation at 532 nm with laser pulses of ca. 10 ns duration.
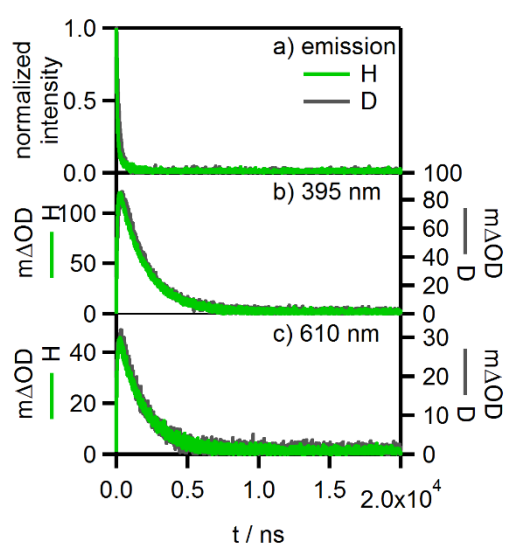

Figure S 3-2 Kinetic traces of 34 µM triad in py with 0.22 M pyH$^+$ (green) and py with 0.22 M pyD$^+$ recorded after excitation at 532 nm with laser pulses of ~10 ns duration.

3.3.3 Spectroelectrochemistry of MQ$^+$ in Acetonitrile

Spectroelectrochemistry on MQ$^+$ was performed in MeCN and the applied potentials are derived from cyclic voltammograms of MQ$^+$ in MeCN.
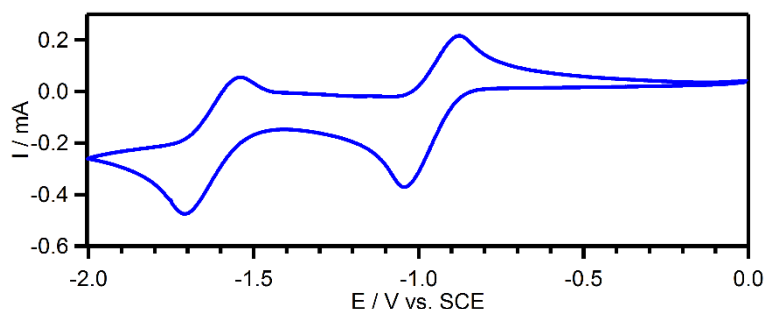
Figure S 3-3 Cyclic voltammogram of 0.02 M MQ$^+$ in MeCN the presence of 0.1 M TBAPF$_6$ as supporting electrolyte at a sweep rate of 0.1 V s^{-1}.
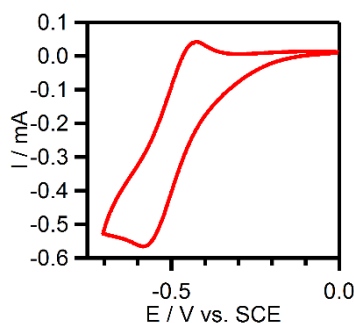

Figure S 3-4 Cyclic voltammogram of 0.03 M MQ$^+$ in MeCN the presence of 0.03 M triflic acid and 0.1 M TBAPF$_6$ as supporting electrolyte at a sweep rate of 0.1 V s^{-1}.

Table S 3-1 Redox potentials of MQ$^+$ and HMQ^{2+} in MeCN with 0.1 M TBAPF$_6$ as supporting electrolyte at sweep rates of 0.1 V s^{-1}. ΔE is the difference of oxidative peak potential and reductive peak potential.

redox process	E / V vs. SCE	ΔE / V
MQ$^{+/\bullet}$	-0.96	0.17
MQ$^{\bullet/-}$	-1.62	0.17
HMQ$^{2+/\bullet+}$	-0.50	0.16

The spectrum of MQ$^{\bullet}$ was generated in a 0.05 M solution of MQPF$_6$ in MeCN with 0.1 M TBAPF$_6$ as supporting electrolyte at a potential of -1 V vs. SCE. The spectrum of HMQ$^{\bullet+}$ was generated by applying -0.5 V vs. SCE on a 0.05 M solution of MQPF$_6$ in MeCN the presence of 0.05 M triflic acid and 0.1 M TBAPF$_6$ as supporting electrolyte.

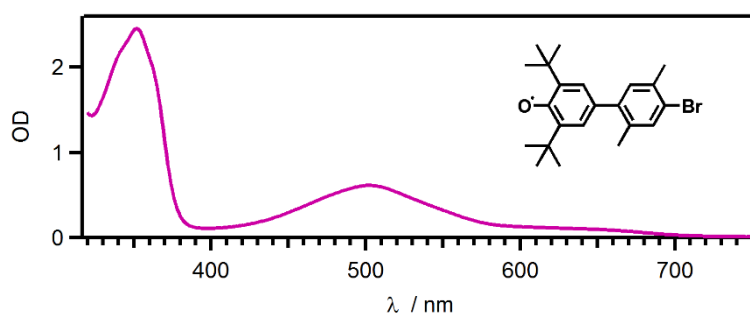### 3.3.4 UV-Vis Spectrum of the Phenoxy Radical

Figure S 3-5 Absorption spectrum of the phenoxy radical of PhOH-xy-TMS in a 1:6 py/toluene mixture after oxidation with $K_3[Fe(CN)_6]$ according to published procedure.[49]

The absorption maxima of the phenoxy radical are at 507 nm and 365 nm.

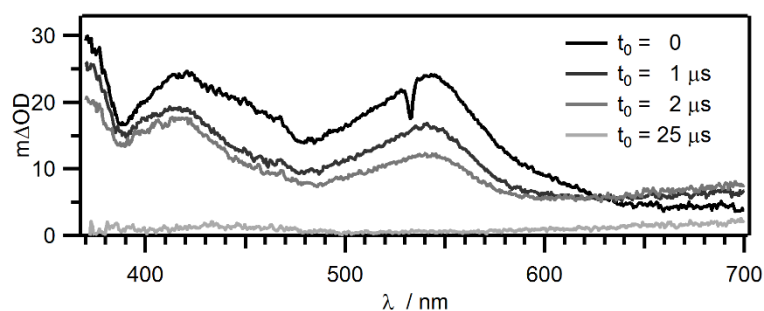### 3.3.5   Kinetic Traces and Transient Absorption Spectra in Pyridine

Figure S 3-6 Transient absorption spectra of 55 μM **PhOH-Ru^{2+}-MQ$^+$** in py. Signal integration occurred over 200 ns at different delay times (t_0) after excitation at 532 nm with laser pulses of ~10 ns duration.
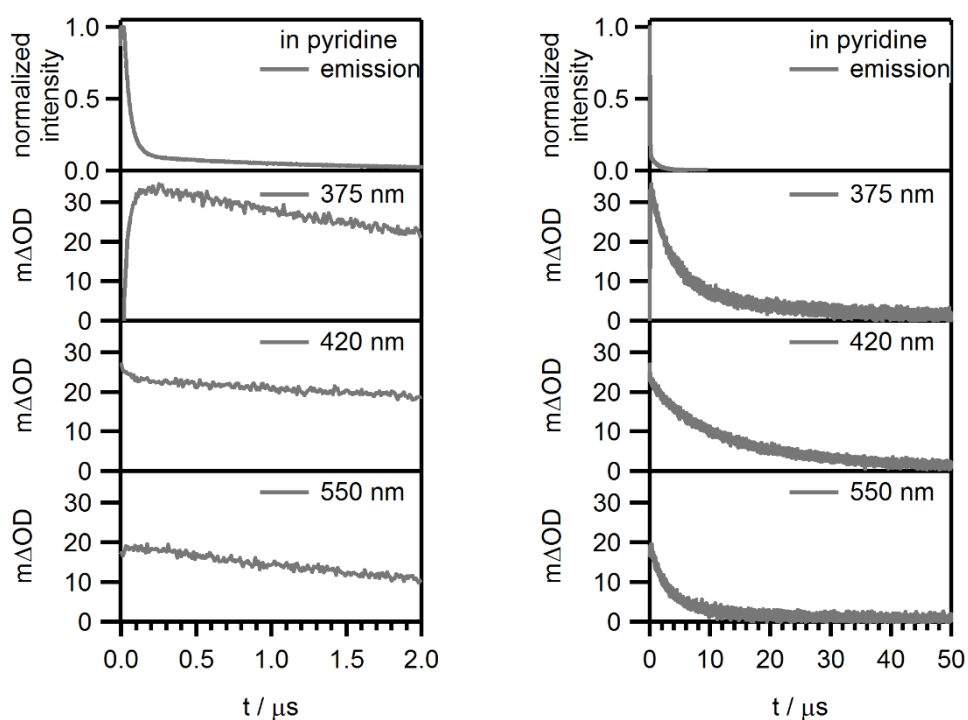
Figure S 3-7 Kinetic traces of 55 μM **PhOH-Ru^{2+}-MQ$^+$** in py recorded after excitation at 532 nm with laser pulses of ~10 ns duration. Two different time scales are shown.

3.3.6 UV-Vis Spectrum of the Deprotonated PhOH-Ru^{2+}-MQ$^+$

The spectrum of the phenolate form of the triad was generated by adding 4 equivalents of TBAOH in MeCN to a solution of PhOH-Ru^{2+}-MQ$^+$ in MeCN under inert conditions. Spectra were recorded at 2 two different times after addition of TBAOH: immediately, and 5 min after addition. Difference spectra of deprotonated PhOH-Ru^{2+}-MQ$^+$ compared to PhOH-Ru^{2+}-MQ$^+$ in MeCN were generated to compare with transient absorption spectra shown in the main article.

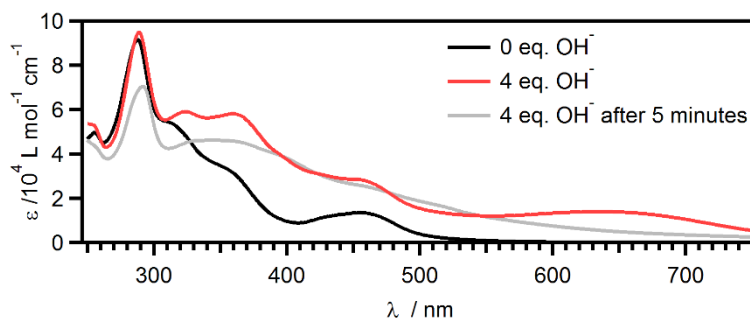**Figure S 3-8** Spectrum of the **PhOH-Ru^{2+}-MQ$^+$** in MeCN (black) and spectrum after addition of 4 equivalents of TBAOH, directly after addition (red) and 5 minutes later (grey), under inert conditions.
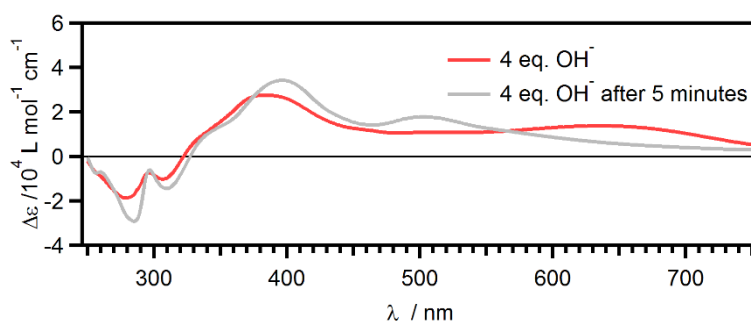

Figure S 3-9 Difference spectra, derived from Figure S 3-8of **PhOH-Ru^{2+}-MQ$^+$** in MeCN (black) and spectrum after addition of 4 equivalents of TBAOH, directly after addition (red) and 5 minutes later (grey), under inert conditions.
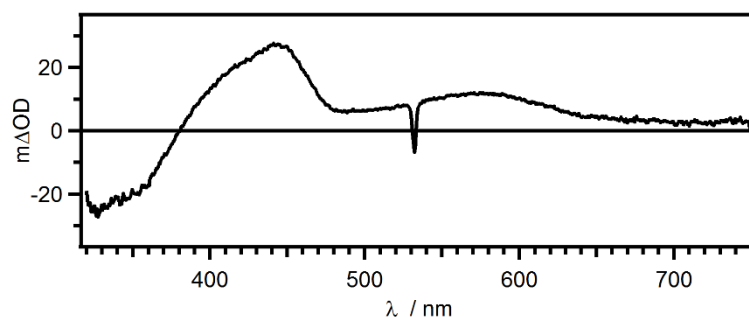
3.3.7 Transient Absorption of PhOH-Ru^{2+}-MQ$^+$ in MeCN

Figure S 3-10 Transient absorption spectrum of 27 µM **PhOH-Ru^{2+}-MQ$^+$** in MeCN. Signal integration occurred over 200 ns directly after excitation at 532 nm with laser pulses of ca. 10 ns duration.

The transient absorption spectrum of the PhOH-Ru^{2+}-MQ$^+$ in MeCN (Figure S 3-10) exhibits maximum absorption around 440 nm and 570 nm and a bleach around 330 nm. This is comparable to the transient absorption spectrum of a similar Ru(bpy)$_3^{2+}$ based photosensitizer with one bpy ligand, substituted with xylenes.[39] Consequently, this spectrum is attributed to the ^{3}MLCT excited state of the photosensitizer in the **PhOH-Ru^{2+}-MQ$^+$** triad.
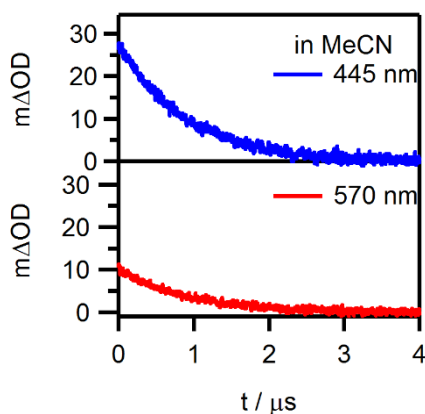

Figure S 3-11 Kinetic traces of transient absorption of 27 µM **PhOH-Ru^{2+}-MQ$^+$** in MeCN after excitation at 532 nm with laser pulses of ca. 10 ns duration.
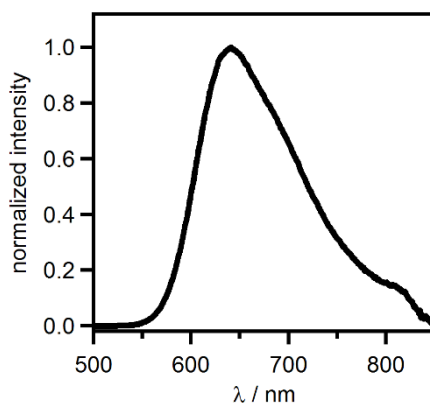
3.3.8 Luminescence Spectrum of PhOH-Ru^{2+}-MQ$^+$

Figure S 3-12 Normalized luminescence spectra of 23 µM **PhOH-Ru^{2+}-MQ$^+$** in MeCN. Excitation occurred at 450 nm.

3.3.9 UV-vis Spectra of PhOH-Ru^{2+}-MQ$^+$ in MeCN and Pyridine
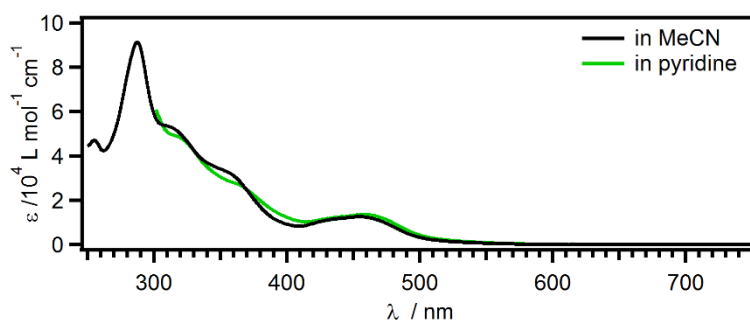
Figure S 3-13 UV-vis spectrum of PhOH-Ru^{2+}-MQ$^+$ in MeCN (black) and in pyridine (green). Below 300 nm pyridine is not sufficiently transparent hence the respective spectrum starts at this wavelength.

3.3.10 **Thermochemistry**

3.3.10.1 **Energy Level Scheme**

Photoinduced radical transfer was performed in py/pyH$^+$ buffer as solvent. No thermochemical data, namely redox potentials and acidity constants of respective reference compounds are reported in pyridine as solvent. Redox potentials and acidity constants are available for water as solvent. Thermochemical calculations are therefore based on aqueous solvent. Water is a polar, hydrogen bonding and protic solvent, whereas pyridine is polar and hydrogen bonding, but not protic (in absence of added acid). The calculated driving forces are therefore to be regarded as an approximation.

Uptake or release of electrons which directly involves the transfer of protons, called proton-coupled electron transfer (PCET). Proton transfer (PT) and electron transfer (ET) can be performed individually, where PT is acid-base chemistry and ET is normal redox chemistry. A PCET is called stepwise PCET when ET is followed by ET or vice versa. When PT and ET take place in a concerted fashion, this is called concerted proton-electron transfer (CPET).

The driving force for PT (ΔG_{PT}) can be calculated with the acidity constants (pK$_a$) of proton donor and proton acceptor:

$$\Delta G_{PT} = 0.059 \text{ eV } \left[pK_a(\text{donor})\text{-}pK_a(\text{acceptor}) \right] \quad\quad (S1)$$

The driving force for ET (ΔG_{ET}) can be calculated with the redox potentials (E) of electron donor and acceptor with the following equation:

$$\Delta G_{ET} = \text{-n F } \Delta E° = E(\text{donor})\text{-}E(\text{acceptor}) \quad\quad (S2)$$

The overall driving force for a PCET reaction (ΔG_{PCET}) is the sum over the driving force for PT and ET:

$$\Delta G_{PCET} = \Delta G_{PT} + \Delta G_{ET} \quad\quad (S3)$$

An energy level diagram for the photoinduced ET, PT and PCET reaction steps was calculated based on reported thermochemical data, namely acidity constants (pKa) and redox potentials E of Ru(bpy)$_3{}^{2+}$, MQ$^+$, 2,4,6-^{t}Bu$_3$PhOH and pyridinium in water.[10,48,57,60]
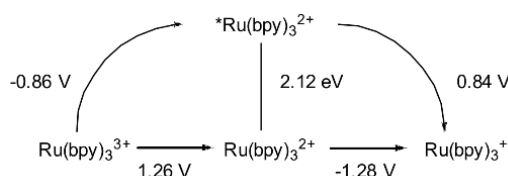

Figure S 3-14 Latimer diagram of Ru(bpy)$_3{}^{2+}$ in water, including excited state energy and redox potentials in ground and excited state in V vs. NHE.[57]
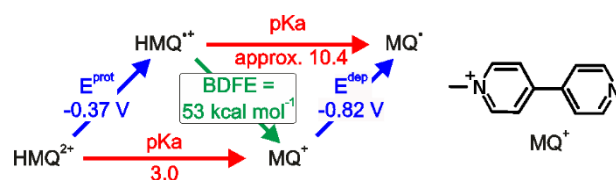
Figure S 3-15 Thermochemical square-scheme for MQ^+ in 1:1 (v:v) CH_3CN/H_2O with redox potentials in V vs. NHE.[48]
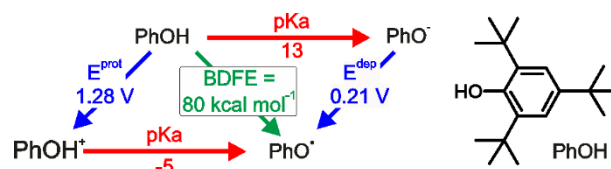

Figure S 3-16 Thermochemical square-scheme for 2,4,6-$^tBu_3PhOH$ in water with redox potentials in V vs. NHE. [10]

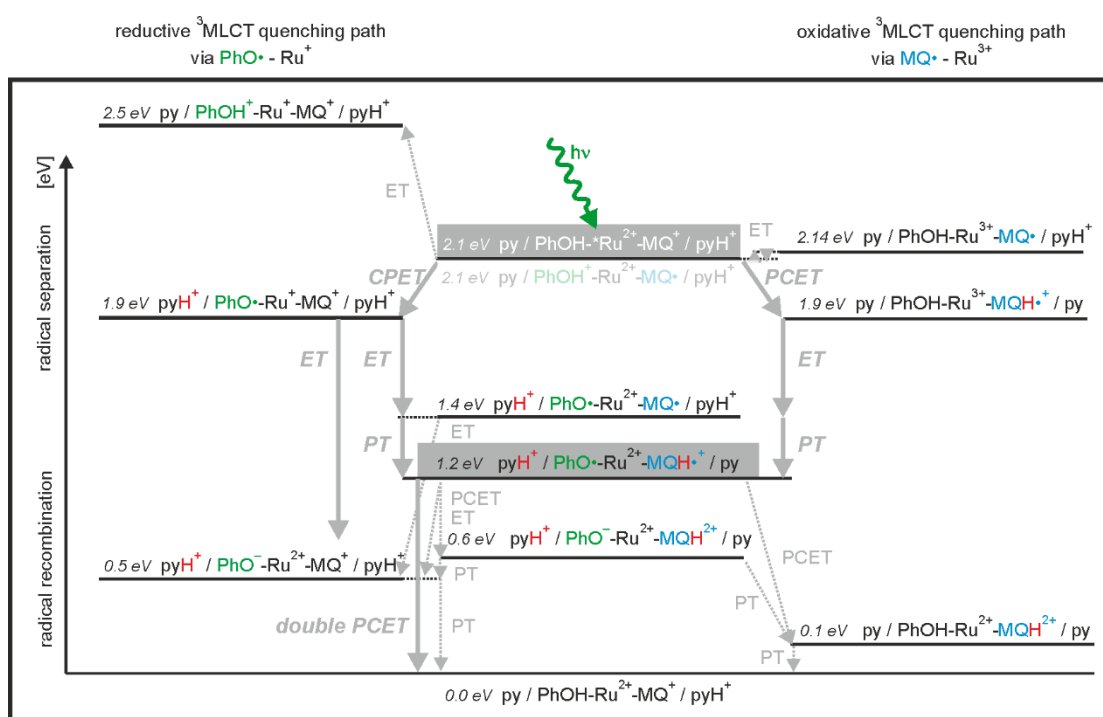The pKa value of pyridinium in water is 5.23.[60]

Figure S 3-17 Energy level diagram for all possible pathways of photoinduced radical separation and thermal recombination. Energy scale estimated based on thermochemical data (pKa, E).

3.3.10.2 **Energy Level Schemes of Observed Reaction Pathways**

In Figure S 3-17, all possible electron and proton transfer steps are depicted, including PCET and CPET steps. Based on observed photoproducts, KIE and the thermochemical considerations in pyridine with 0.22 M pyridinium the key reaction pathways are depicted in Figure S 3-18. Initial reductive and oxidative quenching of excited $Ru(bpy)_3^{2+}$ are endergonic or have no driving force, whereas reductive and oxidative quenching via CPET or PCET respectively are exergonic. Based on thermochemistry, there is no preferential pathway for the initial radical transfer after photoexcitation. The secondary radical transfer was found to be fast because luminescence decay constant equals the rate constant for photo product formation. For phenol oxidation as the secondary step, CPET at the phenol occurs. For reduction of MQ^+ as secondary step, successive ET-PT is expected (see Figure S 3-18).

For pyridine as solvent, protonation of the monoquat acceptor is neither observed, nor expected and reaction pathways are depicted in Figure S 3-19.
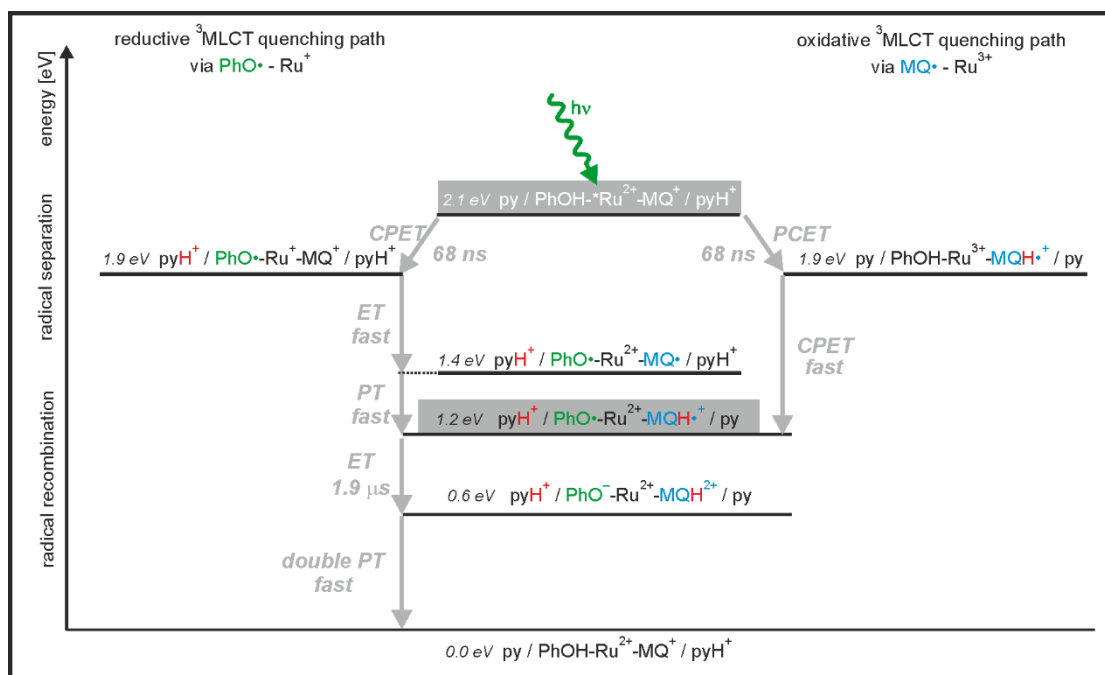

Figure S 3-18 Energy level diagram for photoinduced radical separation and thermal recombination in py with 0.22 M pyH$^+$. Energy scale estimated based on thermochemical data (pKa, E), time constants from kinetic traces, as described in the main article.
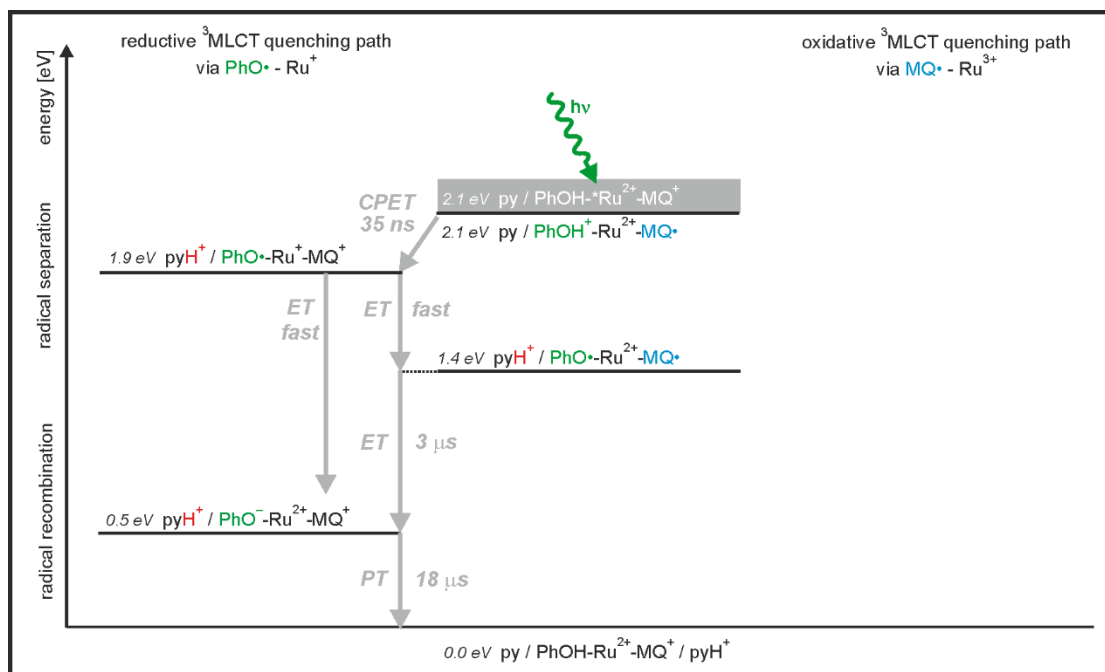
Figure S 3-19 Energy level diagram for photoinduced radical separation and thermal recombination in py. Energy scale estimated based on thermochemical data (pKa, E), time constants from kinetic traces, as described in the main article.

3.3.10.3 **Thermochemical Evaluation of Proton Transfer in the Ground State**

Pyridine was chosen as a base. It was used in very high concentration (neat solvent) and the deprotonation equilibrium (S4) between pyridine and the phenol unit of the triad must be considered. Acidity constants for pyridine and the reference phenol 2,4,6-^{t}Bu$_3$PhOH are available in water which allows an approximation of the acid-base equilibrium.

For the equilibrium described in eq. S4, the equilibrium constant K can be approximated from the pK$_a$ values as described in eq. S5.

$$K = \frac{[pyH^+] \cdot [PhO^-]}{[py] \cdot [PhOH]} \tag{S4}$$

$$K = 10^{-(pK_a(PhOH) - pK_a(pyH^+))} \tag{S5}$$

With $pK_a(pyH^+) = 5.23$ and $pK_a(PhOH) = 13$ one obtains $K = 1.7 \cdot 10^{-8}$.

It is approximated that $[PhOH] = 3 \cdot 10^{-5}$M, the pyridine concentration $[py] = 12.4$ M

The approximate phenolate concentration $[PhO^-]$ is therefore calculated as follows:

With $[pyH^+] = [PhO^-]$ one obtains:

$$K = \frac{([PhO^-])^2}{[py] \cdot [PhOH]} \tag{S6}$$

$$([PhO^-])^2 = K \cdot [py] \cdot [PhOH] \tag{S7}$$

$$[PhO^-] = \sqrt{1.7 \cdot 10^{-8} \cdot [12.4 \text{ M}] \cdot [3 \cdot 10^{-5 \text{M}}]} \tag{S8}$$

$$[PhO^-] = 0.25 \cdot 10^{-5} \text{M} \tag{S9}$$

Based on the pKa values in water, in a $3 \cdot 10^{-5}$M phenol solution up to $0.25 \cdot 10^{-5}$M phenol is deprotonated in pyridine. This amounts to ~8% of the total phenol concentration.

3.3.10.4 Thermochemical Evaluation of Hydrogen Bonding Equilibria in the Ground State

In previous work, it was shown that for PCET chemistry between phenols and an oxiziding photosensitizer the presence of a base and hydrogen bonded adducts are important.[19] The association constants K_A for all investigated phenols with pyridine in acetonitrile as solvent range between 1 and 2 M^{-1}.

For the phenol-unit here an association constant was approximated with $K_A = 1$ M^{-1}.

For the hydrogen bonding equilibrium (S10) that means:

$$\text{PhOH} + \text{py} \leftrightarrows \text{PhO-H-py} \tag{S10}$$

$$K_A = \frac{[\text{PhO-H-py}]}{[\text{PhOH}] \cdot [\text{py}]} \tag{S11}$$

$$K_A = \frac{[\text{PhO-H-py}]}{([\text{PhOH}]_0 - [\text{PhO-H-py}]) \cdot [\text{py}]} \tag{S12}$$

$$[\text{PhO-H-py}] = K([\text{PhOH}]_0 - [\text{PhO-H-py}]) \cdot [\text{py}] \tag{S13}$$

$$[\text{PhO-H-py}] = \frac{[\text{PhOH}]_0 \cdot K \cdot [\text{py}]}{1 + K \cdot [\text{py}]} \tag{S14}$$

With $K_A = 1$ M^{-1}, [py] = 12.4 M and $[\text{PhOH}]_0 = 3 \cdot 10^{-5}$M one obtains:

$$[\text{PhO-H-py}] = 2.8 \cdot 10^{-5} \text{M} \tag{S15}$$

Based the approximation $K_A = 1$ M^{-1}, in a $3 \cdot 10^{-5}$M solution of the triad in pyridine, $2.8 \cdot 10^{-5}$M of the phenol molecules are hydrogen bonded to pyridine. This corresponds to ~93% of all phenol molecules.

3.3.11 Synthesis

All synthesis steps were performed under nitrogen atmosphere. 2,5-Dimethyl-4-trimethylsilyl-1-phenylboronic acid (**2**) was synthesized from 2,5-dibromo-*p*-xylene according to an established procedure.[61] Syntheses of phenols **PhOH-xy-TMS** and **3** were similar to previous work,[61] as well as the borylation yielding **4**,[56] and the synthesis of **6**.[62] [RuCl$_2$(bpy)$_2$]·2 H$_2$O (**10**) was synthesized from 2,2'-bpy and RuCl$_3$·xH$_2$O as reported.[63] The

synthesis of MQPF$_6$ has been reported.[48] All other chemicals used in this work are commercially available.
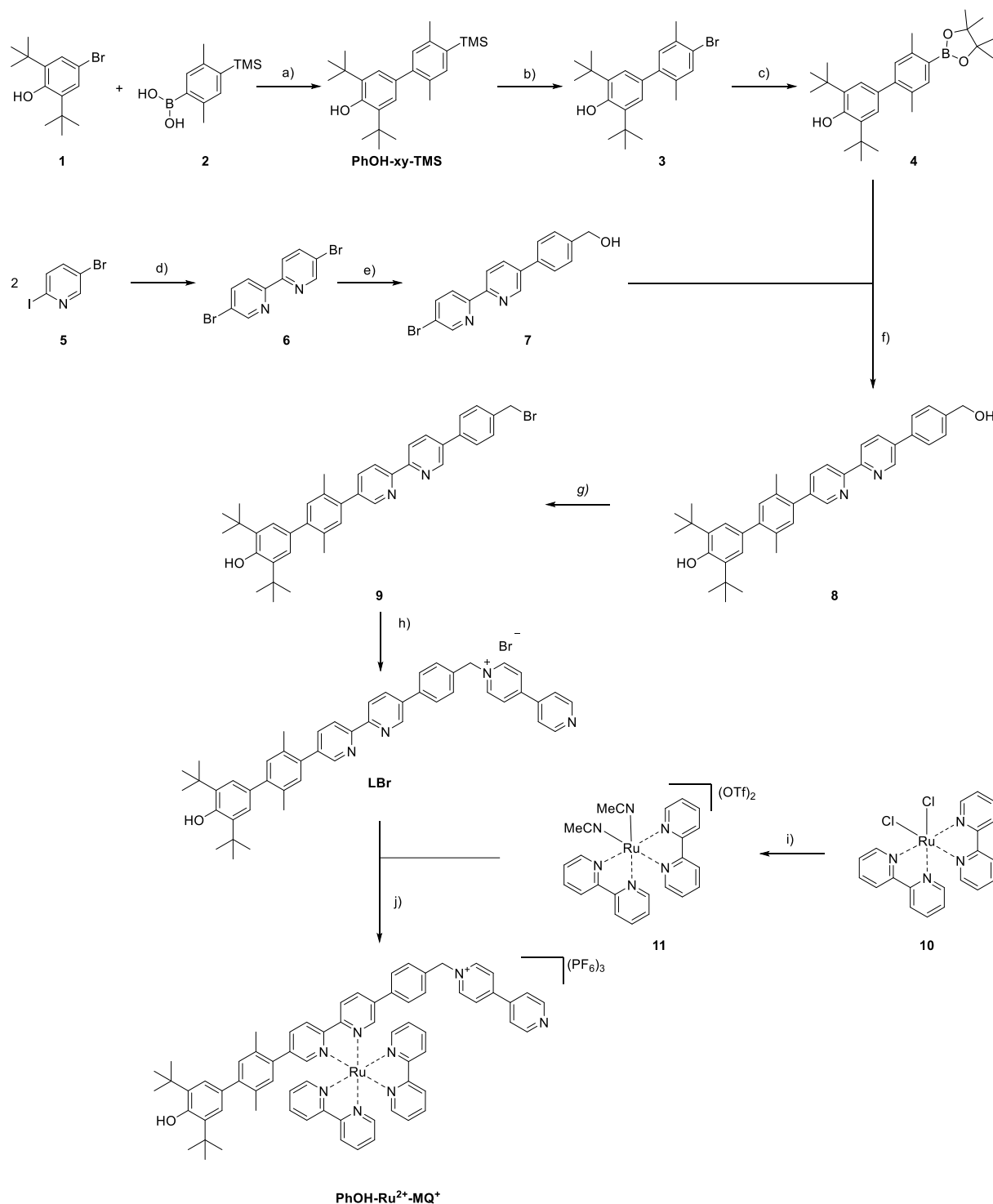
Figure S 3-20 a) Pd(PPh$_3$)$_4$, Na$_2$CO$_3$, THF/H$_2$O 8:1, reflux, dark 67 %, b) Br$_2$, NaOAc, THF, 0 °C, dark 68 %, c) (BPin)$_2$, [PdCl$_2$(dppf)]·CH$_2$Cl$_2$, KOAc, DMSO, 100 °C, 86 %, d) bis(tributyltin), Pd(PPh$_3$)$_4$, m-xylene, 180 °C, <61%, e) 4-(hydroxymethyl)phenylboronic acid, K$_2$CO$_3$, Pd(PPh$_3$)$_4$, THF/H$_2$O 8:1, reflux, 39 %, f) K$_2$CO$_3$, Pd(PPh$_3$)$_4$, THF/H$_2$O 5:1, reflux, 95 %, g) PBr$_3$, dry CH$_2$Cl$_2$, room temperature, 89 %, h) 4,4'-bpy, dry CH$_2$Cl$_2$, reflux, 59 %, i) AgOTf, MeCN, reflux, 100 %, j) ethylene glycol, AgOTf, 105 °C, 90 %.

3.3.11.1 3,5-Di-*tert*-butyl-2',5'-dimethyl-4'-(trimethylsilyl)-[1,1'-biphenyl]-4-ol (PhOH-xy-TMS)[61]
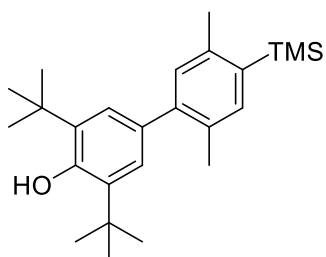
PhOH-xy-TMS

A mixture of 4-bromo-2,6-di-*tert*-butylphenol (**1**) (1.27 g, 4.45 mmol, 1.00 eq.), 2,5-dimethyl-4-trimethylsilyl-1-phenylboronic acid (**2**) (1.19 g, 5.18 mmol, 1.16 eq.), Na_2CO_3 (1.41 g, 13.3 mmol, 3.00 eq.) and $Pd(PPh_3)_4$ (277 mg, 223 μmol, 5.0 mol%) in a degassed mixture of THF (40 mL) and water (5 mL) were heated at reflux in the dark for 16 h. After cooling to room temperature, the m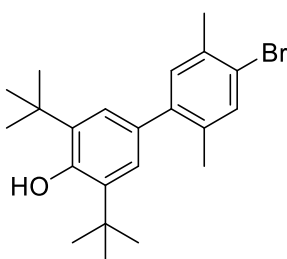ixture was extracted with CH_2Cl_2 (3×). The combined organic phases were dried over Na_2SO_4 and the solvent was removed under reduced pressure. Purification by column chromatography (SiO_2, pentane) afforded **PhOH-xy-TMS** as a colorless oil (1.14 g, 2.98 mmol, 67 %).

^{1}H NMR (400 MHz, CDCl$_3$): δ (ppm) = 7.35 (s, 1H), 7.14 (s, 2H), 7.08 (s, 1H), 5.19 (s, 1H), 2.46 (s, 3H), 2.28 (s, 3H), 1.46 (s, 18H), 0.35 (s, 9H).

^{13}C NMR (101 MHz, CDCl$_3$): δ (ppm) = 152.85, 143.59, 140.96, 136.76, 136.54, 135.46, 132.86, 131.73, 131.60, 126.00, 34.59, 30.59, 22.60, 20.38, 0.13.

3.3.11.2 4'-Bromo-3,5-di-*tert*-butyl-2',5'-dimethyl-[1,1'-biphenyl]-4-ol (3)[61]

3

Bromine (1.3 mL, 4.2 g, 26 mmol, 4.1 eq.) was added to a degassed suspension of **PhOH-xy-TMS** (2.50 g, 6.42 mmol, 1.00 eq.) and NaOAc (1.07 g, 13.0 mmol, 2.03 eq.) in dry THF (40 mL) at 0 °C in the dark. The mixture was stirred in the dark at room temperature for 2.5 h, NEt_3 (7.3 mL, 52 mmol, 8.0 eq.) and saturated aqueous $Na_2S_2O_3$ solution (55 mL) were added, and stirring of the black mixture was continued for 16 h. The mixture was extracted with CH_2Cl_2

(3×), the organic phases were dried over Na_2SO_4 the solvent was removed under reduced pressure. Purification by column chromatography (SiO_2, pentane → pentane/CH_2Cl_2 1:3) afforded compound **3** as an off-white solid (1.71 g, 4.38 mmol, 68 %).

¹H NMR (400 MHz, CDCl₃): δ (ppm) = 7.43 (s, 1H), 7.11 (s, 1H), 7.08 (s, 2H), 5.22 (s, 1H), 2.39 (s, 3H), 2.23 (s, 3H), 1.47 (s, 18H).

¹³C NMR (101 MHz, CDCl₃): δ (ppm) = 153.03, 142.07, 135.64, 134.98, 134.95, 133.83, 132.35, 131.97, 125.82, 122.97, 34.56, 30.54, 22.44, 20.12.

3.3.11.3 3,5-Di-*tert*-butyl-2',5'-dimethyl-4'-(4,4,5,5-tetramethyl-1,3,2-dioxaborolan-2-yl)-[1,1'-biphenyl]-4-ol (4)[56]

4
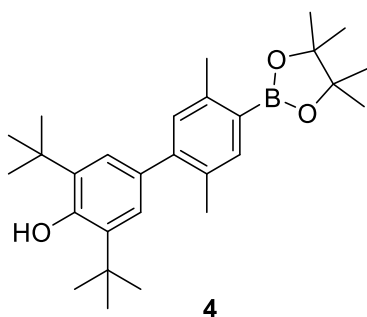
A mixture of **3** (1.65 g, 4.23 mmol, 1.00 eq.), bis(pinacolato)diboron (1.61 g, 6.33 mmol, 1.5 eq.) KOAc (1.66 g, 16.9 mmol, 4.00 eq.) and [PdCl₂(dppf)]·CH_2Cl_2 (172 mg, 211 μmol, 5 mol%) in DMSO (60 mL) was degassed and subsequently heated at 100 °C in the dark for 16 h. After cooling to room temperature, water and brine were added, and the mixture was extracted with pentane (3×). The combined organic phases were dried over Na_2SO_4 and the solvent was removed under reduced pressure. Purification by column chromatography (SiO_2, pentane / CH_2Cl_2 5:1) afforded compound **4** as a white solid (1.57 g, 3.62 mmol, 86 %).

¹H NMR (400 MHz, CDCl₃): δ (ppm) = 7.68 (s, 1H), 7.13 (s, 2H), 7.08 (s, 1H), 5.20 (s, 1H), 2.54 (s, 3H), 2.27 (s, 3H), 1.46 (s, 18H), 1.35 (s, 12H).

**¹³C NMR (101 MHz, CDCl₃):** δ 152.77, 145.14, 142.27, 138.06, 135.32, 132.79, 131.57, 125.74, 83.30, 34.42, 30.42, 24.88, 21.70, 19.97.

3.3.11.4 5,5'-Dibromo-2,2'-bipyridine (6)[62]

6
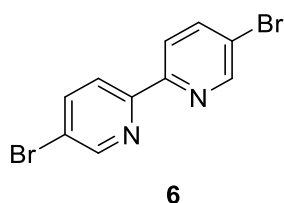
A mixture of 5-bromo-2-iodopyridine (**5**) (12.0 g, 42.3 mmol, 1.00 eq.), bis(tributyltin) (10.7 mL, 12.2 g, 21.2 mmol, 0.50 eq.) and *m*-xylene (60 mL) was degassed. After addition of Pd(PPh$_3$)$_4$ (977 mg, 785 µmol, 1.8 mol%) the reaction mixture was degassed again and heated at reflux for 3d. After cooling to room temperature, the solidified mixture was dissolved in CH$_2$Cl$_2$ and subjected to column chromatography (SiO$_2$, CH$_2$Cl$_2$). Compound **6** was isolated as an off-white solid (8.56 g, <25.9 mmol, <61%) that was contaminated with unidentified tin compounds (approx. 5 mol%) as sometimes observed after Stille coupling reactions.

^{1}H NMR (400 MHz, CDCl$_3$): δ (ppm) = 8.70 (dd, *J* = 2.3, 0.8 Hz, 2H), 8.29 (dd, *J* = 8.4, 0.7 Hz, 2H), 7.93 (dd, *J* = 8.5, 2.4 Hz, 2H).

^{13}C NMR (101 MHz, CDCl$_3$): δ (ppm) = 150.19, 140.22, 122.72, 121.81.

3.3.11.5 (4-(5'-Bromo-[2,2'-bipyridin]-5-yl)phenyl)methanol (7)

7
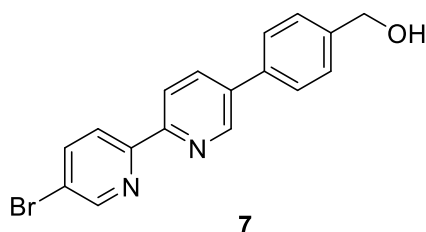
A mixture of **6** (870 mg, 2.77 mmol, 1.00 eq.), K$_2$CO$_3$ (1.15 g, 8.32 mmol, 3.00 eq.), THF (70 mL) and water (15 mL) was degassed. After addition of Pd(PPh$_3$)$_4$ (172 mg, 137 µmol, 5.0 mol%) the mixture was degassed again and heated to reflux. A degassed suspension of 4-(hydroxymethyl)phenylboronic acid (421 mg, 2.77 mmol, 1.00 eq.) in THF (55 mL) was added dropwise to the refluxing reaction mixture within 1 h. After addition was complete the mixture was heated for further 30 min and then cooled to room temperature. The mixture was extracted with CH$_2$Cl$_2$ (3×), the combined organic phases were dried over Na$_2$SO$_4$ and the solvent was removed under reduced pressure. Purification by column chromatography (SiO$_2$, CH$_2$Cl$_2$ → Et$_2$O) afforded unreacted starting material **6** (219 mg, 697 µmol, 25 %) and compound **7** as a white solid (365 mg, 1.07 mmol, 39 %).

^{1}H NMR (400 MHz, CDCl$_3$): δ (ppm) = 8.91 (s, 1H), 8.75 (s, 1H), 8.48 (d, J = 8.3 Hz, 1H), 8.42 (d, J = 8.6 Hz, 1H), 8.06 (dd, J = 8.3, 2.3 Hz, 1H), 7.97 (dd, J = 8.5, 2.3 Hz, 1H), 7.65 (d, J = 8.2 Hz, 2H), 7.52 (d, J = 8.0 Hz, 2H), 4.79 (s, 2H), 1.83 (s, 1H).

^{13}C NMR (101 MHz, DMSO-d$_6$): δ (ppm) = 153.73, 152.89, 149.99, 147.27, 142.95, 139.90, 135.82, 134.97, 134.77, 127.16, 126.52, 122.08, 120.74, 120.42, 62.53.

3.3.11.6 3,5-Di-*tert*-butyl-4'-(5'-(4-(hydroxymethyl)phenyl)-[2,2'-bipyridin]-5-yl)-2',5'-dimethyl-[1,1'-biphenyl]-4-ol (8)


8
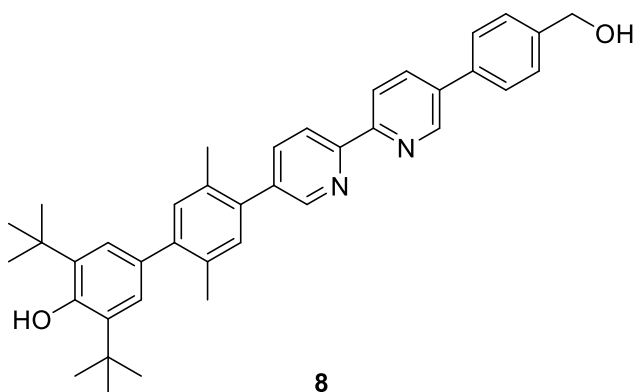
Pd(PPh$_3$)$_4$ (195 mg, 157 µmol, 5.0 mol%) was added to a degassed mixture of **7** (1.06 g, 3.11 mmol, 1.00 eq.), **4** (1.50 g, 3.44 mmol, 1.11 eq.) and K$_2$CO$_3$ (1.30 g, 9.41 mmol, 3.02 eq.), THF (100 mL) and water (20 mL). The mixture was degassed again and subsequently heated to reflux for 15 h in the dark. After removal of THF under reduced pressure the aqueous phase was extracted with CH$_2$Cl$_2$ (3×). The combined organic phases were dried over Na$_2$SO$_4$ and the solvent was removed under reduced pressure. The solid was recrystallized from CH$_2$Cl$_2$/acetone (10 mL/5 mL) Filtration of the precipitate and washing with CH$_2$Cl$_2$ afforded compound **9** as an off-white solid (1.25 g, 2.18 mmol, 70 %). Purification of the mother liquor by column chromatography (SiO$_2$, CH$_2$Cl$_2$ → Et$_2$O) afforded additional **8** (0.44 g, 0.78 mmol, 25 %).

^{1}H NMR (400 MHz, CDCl$_3$): δ (ppm) = 8.95 (dd, J = 2.4, 0.8 Hz, 1H), 8.75 (dd, J = 2.3, 0.9 Hz, 1H), 8.56 – 8.45 (m, 2H), 8.05 (dd, J = 8.3, 2.4 Hz, 1H), 7.87 (dd, J = 8.2, 2.3 Hz, 1H), 7.69 (d, J = 8.1 Hz, 2H), 7.52 (d, J = 7.9 Hz, 2H), 7.24 (s, 1H), 7.22 (s, 1H), 7.19 (s, 2H), 5.24 (s, 1H), 4.80 (d, J = 4.6 Hz, 2H), 2.35 (s, 3H), 2.34 (s, 3H), 1.79 (t, J = 5.4 Hz, 1H), 1.49 (s, 18H).

^{13}C NMR (101 MHz, CDCl$_3$): δ (ppm) = 154.98, 154.27, 153.02, 149.64, 147.76, 142.84, 141.25, 137.73, 137.54, 137.02, 136.38, 136.18, 135.64, 135.29, 133.41, 132.99, 132.48, 132.42, 132.01, 127.87, 127.34, 126.00, 121.13, 120.61, 68.11, 65.05, 34.61, 30.59, 25.75, 20.37, 20.10.

3.3.11.7 4'-(5'-(4-(Bromomethyl)phenyl)-[2,2'-bipyridin]-5-yl)-3,5-di-tert-butyl-2',5'-dimethyl-[1,1'-biphenyl]-4-ol (9)

9
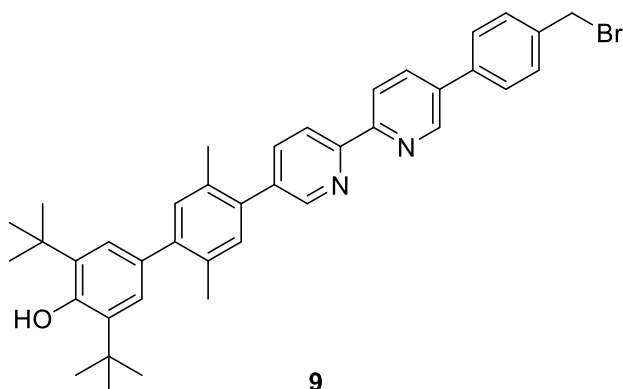
At room temperature, PBr$_3$ (8.32 µL, 87.6 µmol, 1.00 eq.) was added to a suspension of **8** (50.0 mg, 87.6 µmol, 1.00 eq.) in dry CH$_2$Cl$_2$ (5 mL). The yellow solution was stirred at room temperature for 16 h. Brine was added, the mixture was stirred for 30 min and then extracted with CH$_2$Cl$_2$ (3×). The combined organic phases were dried over Na$_2$SO$_4$ and the solvent was removed under reduced pressure. Purification by column chromatography (SiO$_2$, Et$_2$O) afforded compound **9** as an off-white solid (49.4 mg, 78.0 µmol, 89 %).

^{1}H NMR (400 MHz, CDCl$_3$): δ (ppm) = 9.02 – 8.88 (m, 1H), 8.75 (dd, J = 2.3, 0.8 Hz, 1H), 8.58 – 8.41 (m, 2H), 8.08 – 8.02 (m, 1H), 7.87 (dd, J = 8.1, 2.3 Hz, 1H), 7.73 – 7.63 (m, 2H), 7.54 (d, J = 8.2 Hz, 2H), 7.24 (s, 1H), 7.21 (s, 1H), 7.19 (s, 2H), 5.24 (s, 1H), 4.62 (d, J = 38.0 Hz, 2H), 2.35 (s, 3H), 2.34 (s, 3H), 1.49 (s, 18H).

3.3.11.8 1-(4-(5'-(3',5'-Di-*tert*-butyl-4'-hydroxy-2,5-dimethyl-[1,1'-biphenyl]-4-yl)-[2,2'-bipyridin]-5-yl)benzyl)-[4,4'-bipyridin]-1-ium bromide (LBr)


LBr
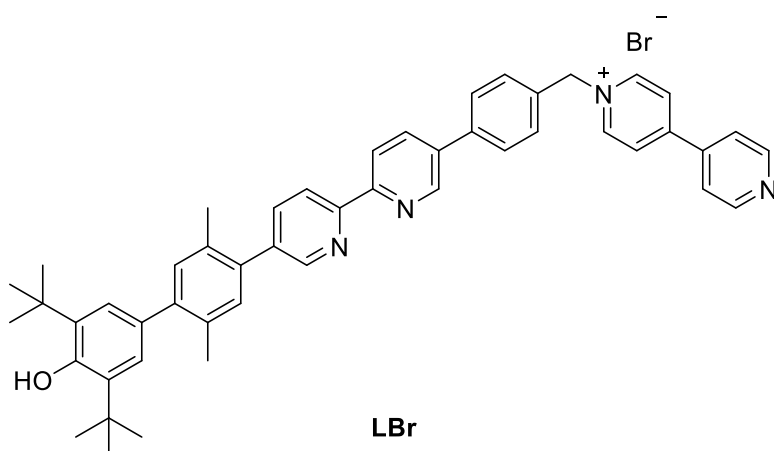
A solution of **9** (159 mg, 251 µmol, 1.00 eq.) and 4,4'-bipyridine (80.0 mg, 512 µmol, 2.04 eq.) in dry CH$_2$Cl$_2$ (30 mL) was heated at reflux for 16 h. The solvent was removed under

reduced pressure. The solid residue was dissolved in $CHCl_3$ (5 mL) and added dropwise to stirring Et_2O. The precipitate was filtered and washed with Et_2O and dried under reduced pressure. The compound **LBr** was obtained as an off-white solid (117 mg, 148 µmol, 59 %)

^{1}H NMR (400 MHz, DMSO-d_6): δ (ppm) = 9.61 – 9.18 (m, 2H), 9.10 (s, 1H), 8.94 – 8.84 (m, 2H), 8.77 (s, 1H), 8.71 – 8.66 (m, 2H), 8.55 (s, 2H), 8.34 (s, 1H), 8.07 – 8.03 (m, 2H), 7.99 – 7.95 (m, 2H), 7.78 (d, J = 8.0 Hz, 2H), 7.24 (s, 1H), 7.21 (s, 1H), 7.10 (s, 2H), 7.07 (s, 1H), 5.98 (s, 2H), 2.31 (s, 3H), 2.28 (s, 3H), 1.44 (s, 18H).

^{13}C NMR (101 MHz, DMSO-d_6): δ (ppm) = 153.04, 152.91, 150.97, 145.42, 141.02, 138.94, 132.56, 131.99, 131.75, 129.86, 127.70, 126.03, 125.21, 122.11, 62.63, 40.15, 39.94, 39.73, 39.52, 39.31, 39.10, 38.89, 34.64, 30.46, 19.94, 19.64.

3.3.11.9 [Ru(bpy)$_2$(MeCN)$_2$](OTf)$_2$ (12)
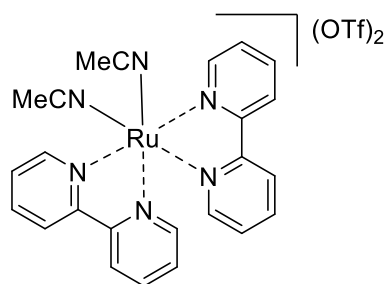
11

A mixture of **10** (298 mg, 572 µmol, 1.00 eq.) and silver triflate (312 mg, 1.21 mmol, 2.12 eq.) in acetonitrile (100 mL) was degassed and then heated at reflux in the dark for 18 h. After cooling to room temperature the precipitate was filtered and rinsed with acetonitrile (5 mL). The solvent of the orange filtrate was removed under reduced pressure, and compound **11** was obtained as an orange solid (453 mg, 572 µmol, ~100%)

^{1}H NMR (400 MHz, CD$_3$CN): δ (ppm) = 9.32 (ddd, J = 5.6, 1.5, 0.8 Hz, 2H), 8.52 (dt, J = 8.2, 1.0 Hz, 2H), 8.41 – 8.34 (m, 2H), 8.27 (ddd, J = 8.2, 7.7, 1.5 Hz, 2H), 7.94 (ddd, J = 8.2, 7.6, 1.5 Hz, 2H), 7.85 (ddd, J = 7.7, 5.6, 1.3 Hz, 2H), 7.59 (ddd, J = 5.7, 1.5, 0.8 Hz, 2H), 7.25 (ddd, J = 7.6, 5.7, 1.3 Hz, 2H), 2.27 (s, 6H).

3.3.11.10   [Ru(bpy)$_2$(L)](PF$_6$)$_3$ (PhOH-Ru^{2+}-MQ$^+$)
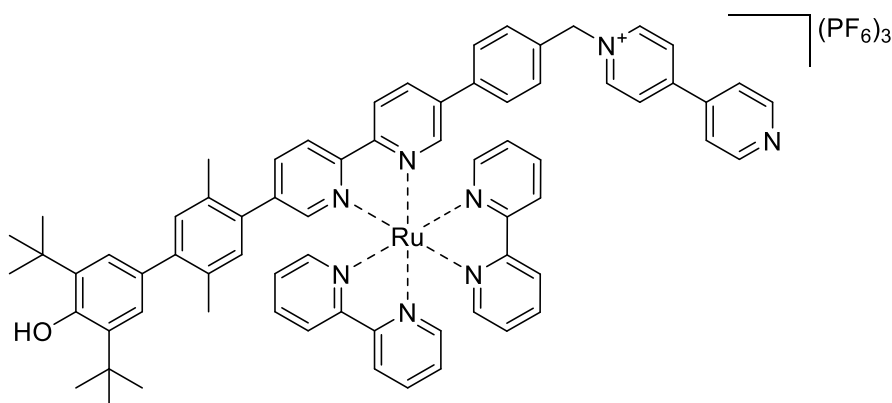
PhOH-Ru^{2+}-MQ$^+$

A suspension of **12** (30.3 mg, 38.0 μmol, 1.00 eq.), the ligand **LBr** (30.0 mg, 38.0 μmol, 1.00 eq.) and silver triflate (15 mg, 58.0 μmol, 1.54 eq.) in ethylene glycol (8 mL) was degassed and then heated at 105 °C for 4 d. After cooling to room temperature, the mixture was taken up in methanol and acetone and filtered through a pad of celite which was then rinsed with acetone. The solvent was removed under reduced pressure, and the residue was purified by column chromatography (SiO$_2$, acetone → acetone, water, saturated aqueous KNO$_3$ 100:10:1 → acetone, water, saturated aqueous KNO$_3$ 100:50:10). Acetate buffer (pH 5, 0.1 M, 10 mL) and saturated aqueous KPF$_6$ solution was added to the last red fraction which contained the desired triad. The organic solvent was removed under reduced pressure. The resulting precipitate was filtered, washed with water and dried under reduced pressure. **[Ru(bpy)$_2$(L)](PF$_6$)$_3$ (PhOH-Ru^{2+}-MQ$^+$)** was obtained as a red solid (53 mg, 34 μmol, 90 %).

^{1}H NMR (400 MHz, CD$_3$CN): δ (ppm) = 8.90 – 8.80 (m, 4H), 8.65 – 8.56 (m, 2H), 8.53 – 8.47 (m, 3H), 8.37 – 8.30 (m, 3H), 8.16 – 7.99 (m, 6H), 7.93 – 7.87 (m, 2H), 7.84 (dd, J = 2.0, 0.7 Hz, 1H), 7.82 (ddd, J = 5.6, 1.6, 0.7 Hz, 1H), 7.80 – 7.77 (m, 2H), 7.73 (ddd, J = 5.6, 1.5, 0.7 Hz, 1H), 7.63 (dd, J = 2.0, 0.7 Hz, 1H), 7.51 (d, J = 0.8 Hz, 4H), 7.48 – 7.34 (m, 4H), 7.12 (s, 1H), 7.10 (s, 2H), 7.05 (s, 1H), 5.77 (s, 2H), 5.57 (s, 1H), 2.23 (s, 3H), 1.98 (s, 3H), 1.43 (s, 18H).

HRMS: calculated (*m/z*) for C$_{69}$H$_{65}$N$_8$ORu$^+$: 374.4776, found: 374.4782.

Anal. Calcd. for C$_{69}$H$_{65}$F$_{18}$N$_8$OP$_3$Ru·0.4 C$_3$H$_6$O·2.5 H$_2$O: C 51.84, H 4.49, N 6.89; found: C 51.53, H 4.87, N 7.27.

4 Hydrogen Bond Effects on Luminescence of Ruthenium(II) Complexes in the Crystalline State

4.1 Abstract

Luminescence spectra of $[Ru((R_2\text{-bpy})_2biimH_2]^{2+}$ (R_2-bpy = 2,2'-bipyridine, substituted in 4 and 4' position, $biimH_2$ = 2,2'-biimidazole) complexes are investigated in the solid state at variable temperature and pressure with R= ^tBu and CF_3. Complexes with electron donating R = ^tBu groups show two overlapping luminescence bands that are resolved at 80 K. In presence of hydrogen bonds to $(CO_2PhSO_3)^{2-}$ (4-sulfonate benzoic acetate dianion), a constant red-shift of luminescence is observed at increasing pressure, which has a changeover in slope in absence of hydrogen bonded $(CO_2PhSO_3)^{2-}$. In complexes with electron withdrawing R = CF_3 groups, only small changes take place at variable temperature or pressure. The influence of the bpy and $biimH_2$ ligands on the luminescence spectra was qualitatively rationalized for the fully protonated and singly deprotonated $biimH_2$ ligands by DFT calculations and excited state proton transfer is discussed.
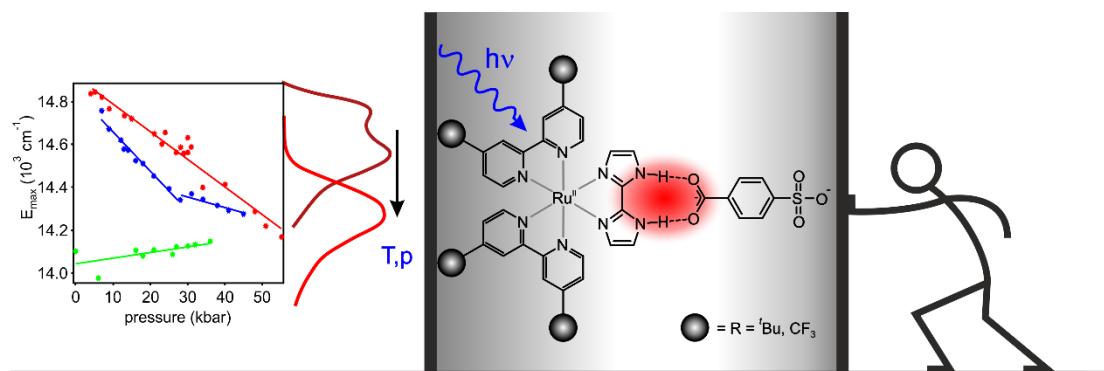
Figure 4-1 Graphical summary of processes at various pressure and temperature for $[Ru((R_2\text{-bpy})_2biimH_2]X$ with R = ^tBu, CF_3 and X = $(CO_2PhSO_3)^{2-}$, 2 Cl^-. Hydrogen bonds are formed with the $(CO_2PhSO_3)^{2-}$.

Author Contributions:

- Andrea Pannwitz[a] carried out synthesis, and spectroscopic measurements in solution. She took part in solid state spectroscopic measurements, data analysis and contributed equally to data interpretation and design of the project.

- Stéphanie Poirier[b] performed Raman and luminescence spectroscopy under pressure and their data analysis. She contributed equally to data interpretation.

- Nicolas Bélanger-Desmarais[b] performed all computational calculations. He also performed Raman and luminescence spectroscopy under pressure and at various temperatures along with data analysis.

- Dr. Alessandro Prescimone[c] measured and solved all single-crystal structures.

- Prof. Dr. Oliver S. Wenger[a] was equally involved in the design of the project and data interpretation.

- Prof. Dr. Christian Reber[b] was equally involved in the design of the project and data interpretation.

[a]Department of Chemistry, University of Basel, St. Johanns-Ring 19, 4056 Basel, Switzerland.

[b]Département de chimie, Université de Montréal, Montréal, Québec H3C 3J7, Canada.

[c]Department of Chemistry, University of Basel, Spitalstrasse 51, 4056 Basel, Switzerland.

4.2 Introduction

Hydrogen bonds are non-covalent interactions that play important roles in 2D or 3D structures, as well as in catalytic transformations. Prominent examples of their structural impact are found in the secondary and tertiary structure of proteins, DNA, and in the scaffolding of supramolecular assemblies. Hydrogen bonds can have crucial effects on charge- and energy-transfer in enzymes and artificial assemblies.[64] In metal complexes, hydrogen bonds are usually secondary coordination sphere interactions, because they primarily involve the ligands as donors or acceptors. This way, hydrogen bonds influence kinetics and thermodynamics of chemical reactions, thereby influencing catalytic conversions with metal complexes.[65,66] Hydrogen bonding effects on luminescence was previously studied in solution, revealing that electronic structure as well as kinetic stability of the excited state will be altered.[67–69] The solution behavior has been studied and analyzed for many compounds, but the effects of such second-sphere interactions on luminescence spectra in the solid state have not been studied systematically. Can temperature and pressure changes influence the excited state of a 1:1 adduct of a hydrogen bonded donor-acceptor system? Secondary coordination sphere interactions in crystalline planar d^8 complexes show characteristic variations with external pressure,[70–72] while in ruthenium polypyridyl complexes such as $[Ru(bpy)_3]^{2+}$, only a very small negative shift on the phosphorescent ^{3}MLCT excited state is observed.[73,74] The presence of hydrogen bond interactions in the secondary coordination sphere is expected to influence the luminescent excited states.
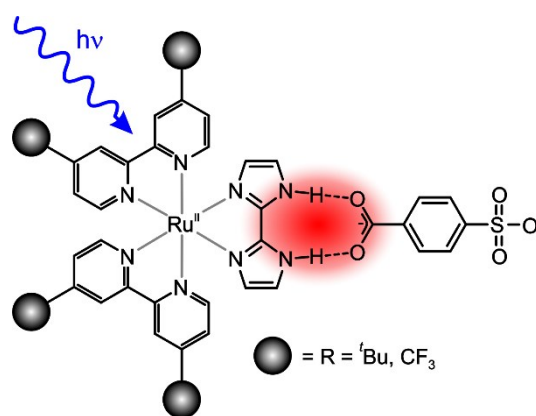
Figure 4-2 The investigated $[Ru(R_2\text{-bpy})_2\text{biimH}_2]^{2+}$ complexes with hydrogen bonding $(CO_2PhSO_3)^{2-}$ counter ion.

We report the luminescence behavior of $[Ru(R_2\text{-bpy})_2\text{biimH}_2]^{2+}$complexes, which are similar to $[Ru(bpy)_3]^{2+}$ except for a single bpy ligand which is replaced by one biimidazole ligand that can donate two hydrogen bonds via the N-H units. Metal biimidazole complexes are

known to form supramolecular assemblies with carboxylic acids.[68,75] As shown in Figure 4-2, hydrogen bonded assemblies with $(CO_2PhSO_3)^{2-}$ are targeted. The bpy spectator ligands are varied with electron donating *tert*-butyl (^tBu) substituents $[Ru(^tBu_2\text{-}bpy)_2biimH_2]^{2+}$ and electron withdrawing CF_3 groups $[Ru((CF_3)_2\text{-}bpy)_2biimH_2]^{2+}$ to identify the electronic effect of the spectator ligands. The effect of the hydrogen bonds was investigated in presence and absence of $(CO_2PhSO_3)^{2-}$ for $[Ru(^tBu_2\text{-}bpy)_2biimH_2]^{2+}$.

4.3 Results and Discussion

4.3.1 Hydrogen-bonded Structures

[Ru(^{t}Bu$_2$-bpy)$_2$biimH$_2$]Cl$_2$ and [Ru((CF$_3$)$_2$-bpy)$_2$biimH$_2$]Cl$_2$ were co-crystallized with Na,K(CO$_2$PhSO$_3$), yielding the hydrogen bonded adduct of [Ru(R$_2$-bpy)$_2$biimH$_2$](CO$_2$PhSO$_3$). Hydrogen bonds were formed between the biimidazole N-H and the carboxylate function of the dianion (CO$_2$PhSO$_3$)$^{2-}$, building a formal 9-membered ring, as sketched in Figure 4-2 and reported for other biimidazole-carboxylate adducts.[68,75] Single crystals of both complexes were measured with X-ray diffraction and their structures were solved. Depending on storage conditions of the crystals, different amounts of co-crystallized solvent molecules were found. Crystals that were stored in the acetone-water mother liquor, hold additional water and acetone molecules. Crystals stored outside the mother liquor do not have any co-crystallized solvent molecules. The presence or absence of solvent molecules, especially hydrogen bonding water molecules influences the crystal structure, lattice parameters and geometry of the hydrogen bonded adduct between imidazole and the carboxylate. In case of [Ru((CF$_3$)$_2$-bpy)$_2$biimH$_2$]-(CO$_2$PhSO$_3$), evaporation of solvent molecules even leads to a phase transition from a monoclinic to triclinic unit cell and two unsymmetrical isomers of the hydrogen bonded adduct. This phase transition also leads to decreased quality of the crystal which induces lower resolution of atom coordinates.

The biimidazole N-H hydrogen atoms of all complexes were found on the electron density map as N-H bond, except for solvent-free [Ru((CF$_3$)$_2$-bpy)$_2$biimH$_2$](CO$_2$PhSO$_3$). In the latter complex, only one N-H bond per molecule was found. The second biimH$_2$-associated hydrogen atom was not found on the electron density map which could be due to strong delocalization of the atom within the N-H-O hydrogen bond.

A short comparison of selected averaged bond lengths is summarized in Table 4-1. It is found that in [Ru(^{t}Bu$_2$-bpy)$_2$biimH$_2$](CO$_2$PhSO$_3$) co-crystals, the Ru-N distances between Ru and bpy-N-donors are comparable to [Ru(bpy)$_3$](PF$_6$)$_2$ and generally longer than in [Ru((CF$_3$)$_2$-bpy)$_2$biimH$_2$](CO$_2$PhSO$_3$) co-crystals.[76] The Ru-N distances between Ru and biimH$_2$-N-donors in all solved structures are at 2.09 Å, except for the solvent-free Ru((CF$_3$)$_2$-bpy)$_2$-biimH$_2$](CO$_2$PhSO$_3$) with a Ru-N^{biimH2} distance of (2.07 ± 0.03) Å. The latter is shorter and the large standard deviation is due to the two different isomers in the unit cell and certain asymmetry at the isomer 1 as described later, in section 4.3.1.4. It is comparable to a reported hydrogen bonded [Ru(bpy)$_2$biimH$_2$]$^{2+}$ with Ru-N^{biimH2} distances of 2.075 Å.[69]

Table 4-1 Selected averaged bond lengths and angles of [Ru(R$_2$-bpy)$_2$biimH$_2$](CO$_2$PhSO$_3$) in comparison with literature values, including standard deviations. a) [Ru(bpy)$_3$](PF$_6$)$_2$,[76] b) [Ru(bpy)$_2$biimH$_2$]$^{2+}$,[69] c) reference, [68,75,77–79] d) reference,[68,75,79]

	Literature	R = ^{t}Bu	R = ^{t}Bu · 2 H$_2$O · 2 C$_3$H$_6$O	R = CF$_3$ · H$_2$O · 2 C$_3$H$_6$O	R = CF$_3$
Temperature		300 K	123 K	123 K	300 K
Ru-N^{bpy} [Å]	2.053 (105 K)^a 2.056 (298 K)^a 2.03 ^{b}	2.045 ± 0.010	2.042 ± 0.006	2.037 ± 0.007	2.03 ± 0.04
Ru-N^{biimH2} [Å]	2.075 ^{b}	2.089 ± 0.002	2.096 ± 0.007	2.095 ± 0.004	2.07 ± 0.03
N···O [Å]	2.62 - 2.75 ^{c}	2.659 ± 0.002	2.688 ± 0.005	2.635 ± 0.015	2.62 ± 0.04
C-O [Å]	1.25 - 1.26 ^{c}	1.249 ± 0.002	1.258 ± 0.005	1.26 ± 0.03	1.26 ± 0.02
Angle (biiimH$_2$)-(carboxylate)	7.2°, 9.3° ^{d}	12.4°	19.9°	27.0°	34.68° and 26.12°

The averaged N···O distances involving the hydrogen bonds are in the normal range for biimidazole-benzoate derivatives at metal complexes, ranging between 2.62 Å and 2.75 Å.[68,75,77–79] The solvent-free [Ru((CF$_3$)$_2$-bpy)$_2$biimH$_2$](CO$_2$PhSO$_3$) exhibits very short N···O distances of (2.62 ± 0.04) Å.

The carboxylate C-O bonds are relatively symmetrical and range around 1.25 and 1.26 Å for Ru(^{t}Bu$_2$-bpy)$_2$biimH$_2$]-(CO$_2$PhSO$_3$) pairs which is compatible with other hydrogen bonded biimidazole-benzoate derivatives at metal complexes that have carboxylate C-O bond lengths between 1.25 Å and 1.26 Å.[68,75,77–79] [Ru((CF$_3$)$_2$-bpy)$_2$biimH$_2$]-(CO$_2$PhSO$_3$) pairs exhibit unsymmetrical carboxylates in both crystal structures (1.26 ± 0.02 Å, 1.26 ± 0.02 Å), as well as unsymmetrical N···O distances (2.635 ± 0.015 Å, 2.62 ± 0.04 Å). This indicates that one proton is further localized on the carboxylate compared to the Ru(^{t}Bu$_2$-bpy)$_2$biimH$_2$]-(CO$_2$PhSO$_3$) pairs. The carboxylate anion coordinates to the planar biimidazole in angles between 12.4° and 34.68° which is significantly larger than in similar iridium bi(benz)imidazole complexes with hydrogen bonds to benzoates (7.2° and 9.3°).[68,75] The larger angles may be due to packing effects involving the bulky substituents on the bpy ligands but are mainly attributed to the hydrogen bonding networks in the crystal structure. The angles between C-O-N and C-N-O that involve the hydrogen bonds in the biimidazole-carboxylate adduct are in a normal range of 120° - 130° for hydrogen bonded structures.

More detailed structural information is discussed in section 4.3.1.1 to 4.3.1.5, including tables of bond lengths and angles and crystallographic data.

4.3.1.1 [Ru(^{t}Bu$_2$-bpy)$_2$biimH$_2$](CO$_2$PhSO$_3$)
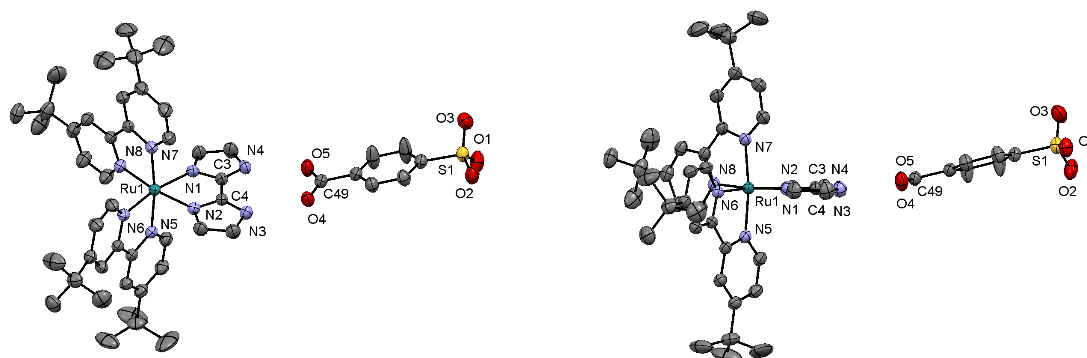
Figure 4-3 The crystallized hydrogen bonded [Ru(^{t}Bu$_2$-bpy)$_2$biimH$_2$](CO$_2$PhSO$_3$) adduct at two perspectives at 300 K. Thermal ellipsoids are drawn at 30% probability level and hydrogen atoms are omitted for clarity.

Crystals of [Ru(^{t}Bu$_2$-bpy)$_2$biimH$_2$](CO$_2$PhSO$_3$), that were stored outside the mother liquor, are found in the monoclinic space group P 2_1/c. The unit cell consists of four asymmetric units and each asymmetric unit consists of one pair of [Ru(^{t}Bu$_2$-bpy)$_2$biimH$_2$]$^{2+}$ and (CO$_2$PhSO$_3$)$^{2-}$. The unit cell parameters of the solvent-free structure at 300 K are:

a 11.5811(3) **b** 20.0963(6) **c** 23.8732(7) and **α** 90 **β** 98.459(4) **γ** 90.

Ru-N distances for bipyridine donor atoms are between 2.029 Å and 2.055 Å which is for most of these Ru-N^{bpy} distances slightly shorter than in [Ru(bpy)$_3$](PF$_6$)$_2$ (2.053 Å) at room temperature.[76] The Ru-N distances to the biimH$_2$ donor atoms are longer than the Ru-N^{bpy} distances, namely 2.087 Å and 2.091 Å. According to the electron density map, protons are located at N3 and N4, which are the hydrogen bond donors in the adduct of biimH$_2$ and carboxylate. The carboxylate exhibits similar C-O bond lengths of 1.247 Å and 1.251 Å. The N···O distances in the hydrogen bonded adduct are 2.674 Å and 2.643 Å, the N^{biimH2}-O-C^{CO2} angles are 128.71° and 128.49°, and the C^{biimH2}-N^{biimH2}-O angles are 125.77° and 126.78°. The angle between the biimH$_2$ plane and the carboxylate plane is 12.44° which is comparable to the bending observed in similar hydrogen bonded adducts with iridium bi(benz)imidazole complexes hydrogen bound to benzoates at 7.2° and 9.3°.[68,75]
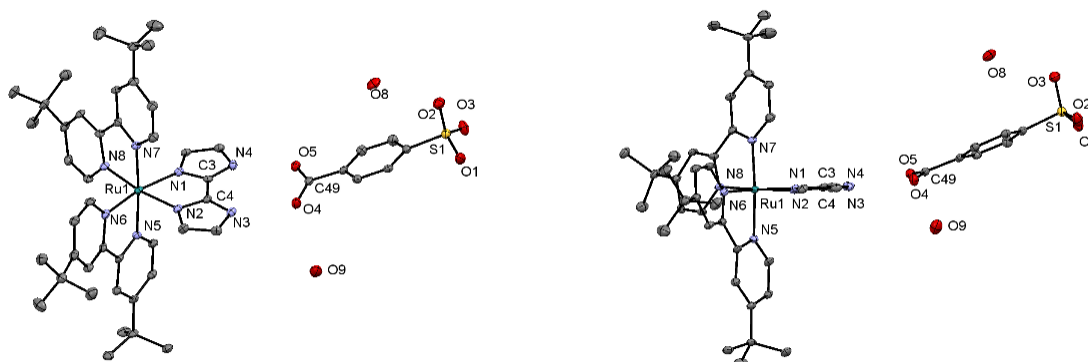
4.3.1.2   [Ru(^{t}Bu$_2$-bpy)$_2$biimH$_2$](CO$_2$PhSO$_3$) · 2 H$_2$O · 2 C$_3$H$_6$O

Figure 4-4 The hydrogen bonded adduct in crystals of [Ru(^{t}Bu$_2$-bpy)$_2$biimH$_2$](CO$_2$PhSO$_3$) · 2 H$_2$O · 2 C$_3$H$_6$O from two perspectives at 123 K. Thermal ellipsoids are drawn at 30% probability level. Hydrogen atoms and acetone molecules are omitted for clarity.

Crystals of [Ru(^{t}Bu$_2$-bpy)$_2$biimH$_2$](CO$_2$PhSO$_3$) · 2 H$_2$O · 2 C$_3$H$_6$O stored in the acetone-water mother liquor have the monoclinic space group P 2$_1$/c. The unit cell consists of four asymmetric units and each asymmetric unit consists of one [Ru(^{t}Bu$_2$-bpy)$_2$biimH$_2$]-(CO$_2$PhSO$_3$) pair, two acetone and two water molecules. The unit cell parameters of this structure at 123 K are:

a 11.2577(8) **b** 21.9487(16) **c** 23.1222(13) and **α** 90 **β** 95.020(3) **γ** 90.

The presence of additional solvent molecules manifests by the almost 2 Å longer b-axis compared to the solvent-free structure at 300 K. The other axes are shorter compared to the solvent-free structure, because the crystal was cooled down to 123 K, contracting the crystal structure.

Ru-N distances for bipyridine donor atoms vary between 2.034 Å and 2.050 Å which is slightly shorter than the Ru-N^{bpy} distances in [Ru(bpy)$_3$](PF$_6$)$_2$.[76] The distances of Ru to the N-donor atoms of the biimidazole ligand are 2.089 Å and 2.103 Å, which is slightly more unsymmetrical compared to the solvent-free structure. The carboxylate exhibits slightly unsymmetrical C-O bond lengths of 1.253 Å and 1.262 Å. The N···O distances in the hydrogen bonded adduct are 2.664 Å and 2.711 Å. The N^{biimH2}-O-C^{CO2} angles are 121.09 ° and 132.27°, and the C^{biimH2}-N^{biimH2}-O angles are 122.15° and 131.39° which is distorted compared to the solvent-free structure. The carboxylate plane is bent by 19.49° with respect to the biimidazole plane. This is also stronger than in the solvent-free structure and stronger than in iridium bi(benz)imidazole complexes hydrogen bound to benzoates at 7.2° and 9.3°.[68,75] Incorporation of solvent, especially water molecules seems to affect the geometry of the [Ru(^{t}Bu$_2$-

bpy)$_2$biimH$_2$]-(CO$_2$PhSO$_3$) adduct. The solvent water associated with O9 coordinates to O4 of the carboxylate at 2.929 Å and to O3 of a neighboring sulfonate at 2.871 Å. O9 therefore bridges two neighboring anions, forming hydrogen bonded anion chains through the crystal structure. Another water molecule (O8) is coordinated to O2 of the sulfonate function at 2.805 Å, but has no further hydrogen bonds.

4.3.1.3 [Ru((CF$_3$)$_2$-bpy)$_2$biimH$_2$](CO$_2$PhSO$_3$) · H$_2$O · 2 C$_3$H$_6$O
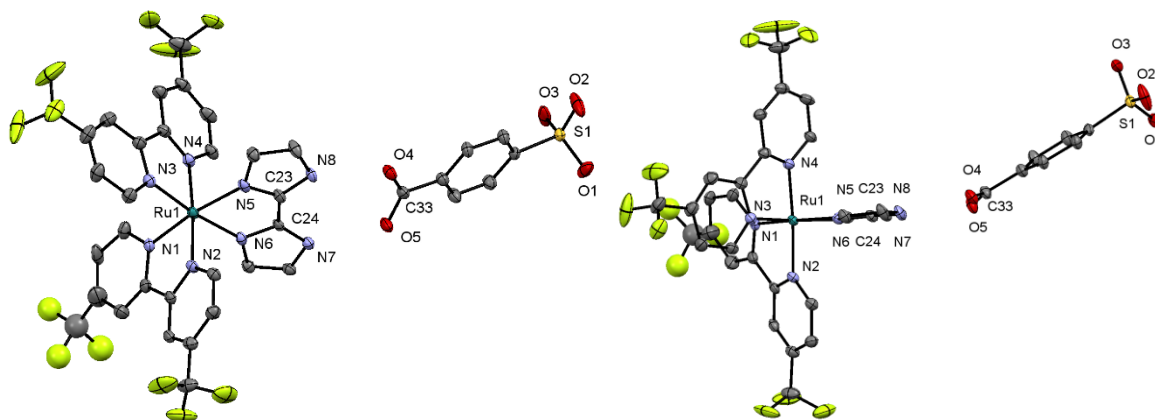
Figure 4-5 The hydrogen bonded adduct in crystals of [Ru((CF$_3$)$_2$-bpy)$_2$biimH$_2$](CO$_2$PhSO$_3$) · H$_2$O · 2 C$_3$H$_6$O from two perspectives at 123 K. Thermal ellipsoids are drawn at the 30% probability level. Hydrogen atoms and solvent molecules are not shown.

[Ru((CF$_3$)$_2$-bpy)$_2$biimH$_2$]$^{2+}$ and the counter ion (CO$_2$PhSO$_3$)$^{2-}$ crystallize in the monoclinic space group Pc as hydrogen bonded 1:1 adduct as represented in Figure 4-5. The unit cell consists of two asymmetric units and each asymmetric unit consists of one [Ru((CF$_3$)-bpy)$_2$biimH$_2$]-(CO$_2$PhSO$_3$) pair, one water and two acetone molecules. The unit cell parameters of this structure at 123 K are:

a 11.4686(10) **b** 11.6843(11) **c** 18.0917(16) and **α** 90 **β** 95.541(4) **γ** 90.

Ru-N distances for bipyridine donor atoms vary between 2.030 Å and 2.047 Å which is slightly shorter, than the Ru-N^{bpy} distances in [Ru(bpy)$_3$](PF$_6$)$_2$.[76] The distances of Ru to the N-donor atoms of the biimidazole ligand are 2.099 Å and 2.091 Å, which is slightly more unsymmetrical compared to the solvent-free [Ru(^{t}Bu$_2$-bpy)$_2$biimH$_2$](CO$_2$PhSO$_3$) structure. The carboxylate exhibits slightly unsymmetrical C-O bond lengths of 1.234 Å and 1.291 Å, comparable to crystalline benzoic acid (1.252 and 1.281 Å).[80] The N···O distances in the hydrogen bonded adduct are 2.620 Å and 2.650 Å. The N^{biimH2}-O-C^{CO2} angles are 122.64° and 128.02°, and the C^{biimH2}-N^{biimH2}-O angles are 124.19° and 129.41°. The carboxylate plane is bent by 27.00° compared to the biimidazole plane, which is even stronger bent than in the

[Ru(^{t}Bu$_2$-bpy)$_2$biimH$_2$](CO$_2$PhSO$_3$) · 2 H$_2$O · 2 C$_3$H$_6$O structure. Solvent effect on the geometry of the structure cannot be assigned, because solvent molecules are highly disordered and were eliminated from the refinement with the Squeeze procedure when solving the structure. However, several close-contact interactions were found in the crystal structure between the sulfoxide group and carbon bound hydrogen atoms and carbons of neighboring bpy and biimH$_2$ ligands as well as between the carboxylate oxygen O4 and hydrogen atoms of neighboring bpy ligands and several interactions with fluorine atoms: F1-N8^{biimH2}, F9-C8^{bpy}, F12-C11^{bpy}, F12-H211$^{CH-biimH2}$.

4.3.1.4 [Ru((CF$_3$)$_2$-bpy)$_2$biimH$_2$](CO$_2$PhSO$_3$)

Isomer 1:
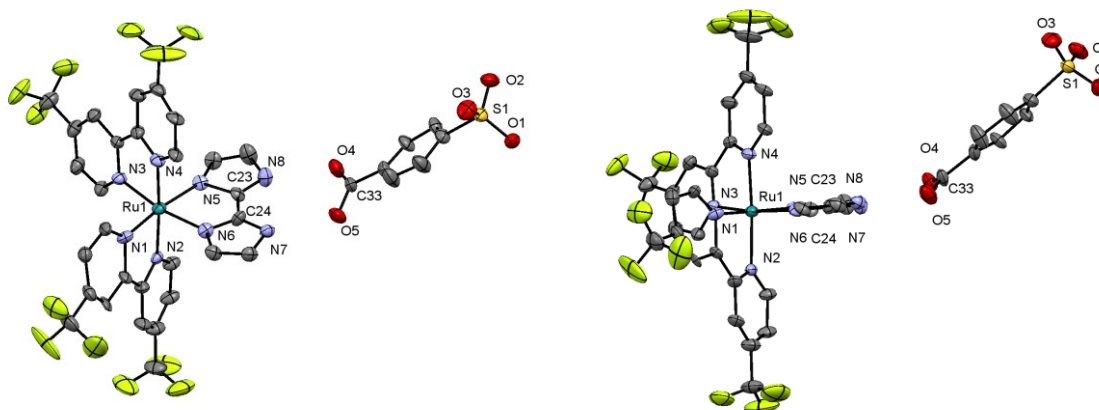
Isomer 2:
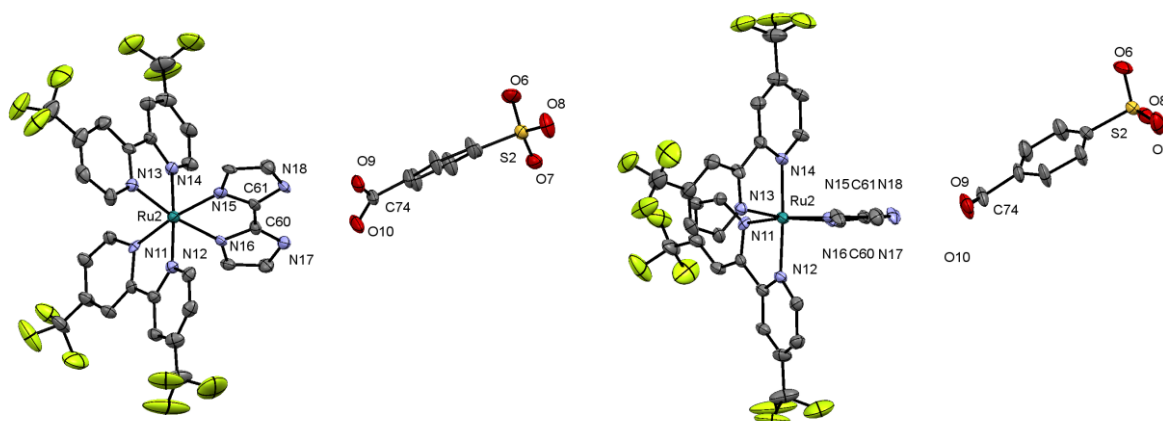
Figure 4-6 Hydrogen bonded adducts in the crystal structure of [Ru((CF$_3$)$_2$-bpy)$_2$biimH$_2$]-(CO$_2$PhSO$_3$) from two perspectives at 300 K. Thermal ellipsoids are drawn at the 50% probability level. Hydrogen atoms are omitted.

Crystals of $[Ru((CF_3)_2$-bpy$)_2$biimH$_2](CO_2PhSO_3)$, that were stored outside the mother liquor, are found in the triclinic space group P 1. The unit cell consists of two $[Ru((CF_3)_2$-bpy$)_2$biimH$_2]$-(CO_2PhSO_3) pairs and has the following unit cell parameters at 300K:

a 11.0765(6) **b** 11.1214(6) **c** 18.3747(9) and α 92.487(3) β 93.933(3) γ 93.919(3).

Due to solvent loss, a phase change from monoclinic to triclinic takes place and the a and b axes are shorter by approximately 0.5 Å compared to $[Ru((CF_3)_2$-bpy$)_2$biimH$_2](CO_2PhSO_3)$ · H_2O · 2 C_3H_6O. The c axis is longer by approximately 0.3 Å due to higher temperature.

Ru-N distances for bipyridine donor atoms vary between 1.99 Å and 2.08 Å which is quite unsymmetrical compared to the other $[Ru(R_2$-bpy$)_2$biimH$_2](CO_2PhSO_3)$ structures.[76] The distances of Ru to the N-donor atoms of the biimidazole ligand are even more unsymmetrical than the solvent containing analogue. Isomer 1 exhibits Ru-N^{biimH2} distances of 2.02 Å and 2.08 Å, which are 2.10 Å and 2.076 Å in isomer 2. Especially in isomer 1 the Ru-N^{biimH2} distances are very short compared to all other structures in this study and compared to a reported structure of hydrogen bonded $[Ru(bpy)_2biimH_2]^{2+}$ (2.075 Å).[69]

The N$\cdots$O distances in the hydrogen bonded adduct in isomer 1 are 2.58 Å and 2.68 Å which is even more unsymmetrical than in the solvent containing analogue. Isomer 2 seems to be more symmetrical with its N$\cdots$O distances being 2.61 Å and 2.62 Å.

In the unsymmetrical isomer 1, the carboxylate C-O bond lengths are at 1.23 Å and 1.28 Å which is comparable to the solvent containing structure and C-O bond lengths in crystalline benzoic acid (1.252 and 1.281 Å).[80] The carboxylate C-O bond lengths of the more symmetrical isomer 2 range around 1.26 Å.

In isomer 1, the N^{biimH2}-O-C^{CO2} and C^{biimH2}-N^{biimH2}-O angles are around 125° and 126°, indicating a symmetric arrangement of the hydrogen bonded adduct despite of unsymmetrical N$\cdots$O distances and C-O bond length. The arrangement in isomer 2 is slightly distorted with N^{biimH2}-O-C^{CO2} angles of 126° and 131° and C^{biimH2}-N^{biimH2}-O angles of 123.4° and 127.8°.

The carboxylate plane of isomer 1 is bent by 34.7° with respect to the biimidazole plane, which is even stronger bent than in the respective, solvent containing structure. The same angle in isomer 2 is 26.1° and therefore comparable to the solvent containing structure.

No solvent molecules are found after evaporation, therefore their influence on the geometry of hydrogen bonded adduct is limited to preorganization during crystallization. Close-contact interactions, as described in section for $[Ru((CF_3)_2$-bpy$)_2$biimH$_2](CO_2PhSO_3)$ · H_2O · 2 C_3H_6O were also found in the solvent-free structure and might strongly influence the geometry in the crystal.

No clear statement on the protonation grade of the biimidazole ligands and the carboxylates can be made. Only one N-H bond per ruthenium complex was found on the electron density map, whereas the exact position of the second hydrogen atom in the hydrogen bonded adduct remains unclear. Nevertheless, it must be located between the respective N and O atom because these atoms are in hydrogen bonding distance and they would be further apart in absence of this proton. It is possible, that this proton is delocalized in the hydrogen bond.

4.3.1.5 Tables on Structural Data of Single Crystals

Table 4-2 Selected distances and angles of $[Ru(^tBu_2\text{-}bpy)_2biimH_2](CO_2PhSO_3)$ and $[Ru(^tBu_2\text{-}bpy)_2biimH_2](CO_2PhSO_3) \cdot 2\ H_2O \cdot 2\ C_3H_6O$.

R = ^{t}Bu	$[Ru(^tBu_2\text{-}bpy)_2biimH_2]\text{-}(CO_2PhSO_3)$	$[Ru(^tBu_2\text{-}bpy)_2biimH_2]\text{-}(CO_2PhSO_3) \cdot 2\ H_2O \cdot 2\ C_3H_6O$
identification	AP2_300K	BIlmH2tBu_ac_123K
temperature	300 K	123 K
bond	**length [Å]**	**length [Å]**
Ru1-N5 (bpy)	2.046 (2)	2.050 (4)
Ru1-N6 (bpy)	2.029 (2)	2.034 (4)
Ru1-N7 (bpy)	2.055 (2)	2.046 (4)
Ru1-N8 (bpy)	2.051 (2)	2.039 (4)
Ru1-N1 (biimH$_2$)	2.087 (2)	2.103 (4)
Ru1-N2 (biimH$_2$)	2.091 (2)	2.089 (4)
N4-O5	2.674 (3)	2.711 (5)
N3-O4	2.643 (2)	2.664 (5)
C43-O4	1.247 (3)	1.253 (6)
C43-O5	1.251 (3)	1.262 (5)
angle	**angle [°]**	**angle [°]**
C49-O4-N3	128.7 (2)	121.1 (3)
C49-O5-N4	128.5 (2)	132.3 (3)
C3-N4-O5	125.8 (1)	122.1 (3)
C4-N3-O4	126.8 (1)	131.4 (3)
[C49O4O5]-biiimH$_2$	12.44	19.49

Table 4-3 Selected distances and angles of the monocrystalline [Ru((CF$_3$)$_2$-bpy)$_2$biimH$_2$](CO$_2$PhSO$_3$) · H$_2$O · 2 C$_3$H$_6$O and [Ru((CF$_3$)$_2$-bpy)$_2$biimH$_2$](CO$_2$PhSO$_3$).

R = CF$_3$	[Ru((CF$_3$)$_2$-bpy)$_2$biimH$_2$]-(CO$_2$PhSO$_3$) · H$_2$O · 2 C$_3$H$_6$O	[Ru((CF$_3$)$_2$-bpy)$_2$biimH$_2$](CO$_2$PhSO$_3$)		
identification	BILMH2CF3_123K	AP_CF3_300K		
temperature	123 K	300 K		
bond	**length [Å]**	**length [Å] isomer 1**	**length [Å] isomer 2**	**bond isomer 2**
Ru1-N1	2.030 (6)	1.99(1)	1.96(1)	Ru2-N11
Ru1-N2	2.047 (4)	2.08(1)	2.06(1)	Ru2-N12
Ru1-N3	2.042 (4)	2.04(1)	2.052(9)	Ru2-N13
Ru1-N4	2.030 (4)	2.05(1)	2.03(1)	Ru2-N14
Ru1-N5(biimH$_2$)	2.099 (4)	2.02(1)	2.10(1)	Ru2-N15(biimH$_2$)
Ru1-N6(biimH$_2$)	2.091 (4)	2.08(1)	2.076(9)	Ru2-N16(biimH$_2$)
N7-O5	2.620 (5)	2.58(2)	2.61(2)	N17-O10
N8-O4	2.650 (5)	2.68(2)	2.62(2)	N18-O9
C33-O4	1.234 (6)	1.23(2)	1.26(2)	C74-O9
C33-O5	1.291 (6)	1.28(2)	1.26(2)	C74-O10
angle	**angle [°]**	**angle [°] isomer 1**	**angle [°] isomer 2**	**angle isomer 2**
C33-O4-N8	122.6 (3)	125(1)	126(1)	C74-O9-N18
C33-O5-N7	128.0 (3)	126(1)	131(1)	C74-O10-N17
C24-N7-O5	124.2 (3)	126.0(9)	123.4(8)	C60-N17-O10
C23-N8-O4	129.4 (3)	125(1)	127.8(8)	C61-N18-O9
[C33O4O5]-biiimH$_2$	27.00	34.7	26.1	[C74O9O10]-biiimH$_2$

Table 4-4 Crystallographic data of [Ru(^{t}Bu$_2$-bpy)$_2$biimH$_2$](CO$_2$PhSO$_3$) and [Ru(^{t}Bu$_2$-bpy)$_2$-biimH$_2$](CO$_2$PhSO$_3$) · 2 H$_2$O · 2 C$_3$H$_6$O.

R = ^{t}Bu	[Ru(^{t}Bu$_2$-bpy)$_2$biimH$_2$]-(CO$_2$PhSO$_3$)	[Ru(^{t}Bu$_2$-bpy)$_2$biimH$_2$]-(CO$_2$PhSO$_3$) · 2 H$_2$O · 2 C$_3$H$_6$O
identification	AP2_300K	BIlmH2tBu_ac_123K
formula	C$_{49}$H$_{58}$N$_8$O$_5$Ru$_1$S$_1$	C$_{55}$H$_{74}$N$_8$O$_9$Ru$_1$S$_1$
moiety formula	C$_{42}$ H$_{54}$ N$_8$ Ru, C$_7$ H$_4$ O$_5$ S	C$_{42}$ H$_{54}$ N$_8$ Ru, C$_7$ H$_4$ O$_5$ S, 2(C$_3$ H$_6$ O), 2(H$_2$ O)
formula weight	972.19	1124.38
Z	4	4
calc. density[Mg m^{-3}]	1.164	1.312
F(000)	2032	2368
description + size of crystal [mm^3]	red block (0.050 · 0.080 · 0.100)	red block (0.090 · 0.120 · 0.130)
abs. coeff. [mm^{-1}]	3.017	3.063
min/max transmission	0.72 / 0.86	0.49 / 0.76
T [K]	300	123
radiation [Å]	Cu Kα (λ = 1.54178)	Cu Kα (λ = 1.54178)
crystal system	monoclinic	monoclinic
space group	P 1 21/c 1	P 1 21/c 1
a [Å]	11.5811(3)	11.2577(8)
b [Å]	20.0963(6)	21.9487(16)
c [Å]	23.8732(7)	23.1222(13)
α [°]	90	90
β [°]	93.6399(11)	95.020(3)
γ [°]	90	90
V [Å^3]	5545.0(3)	5691.4(7)
min/max Θ	3.710 / 70.048	3.838 / 70.085
collected refl.	43147	35192
indep. refl.	10105	10254
merging r	0.031	0.085
obs. refl.	10006 (I>2.0σ(I))	10220 (I>2.0σ(I))
ref. param.	577	667
R	0.0494	0.0605
rW	0.0813	0.1647
gof	1.2066	0.9212

Table 4-5 Crystallographic data of [Ru((CF$_3$)$_2$-bpy)$_2$biimH$_2$](CO$_2$PhSO$_3$) · H$_2$O · 2 C$_3$H$_6$O and [Ru((CF$_3$)$_2$-bpy)$_2$biimH$_2$](CO$_2$PhSO$_3$).

R = CF$_3$	[Ru((CF$_3$)$_2$-bpy)$_2$biimH$_2$]-(CO$_2$PhSO$_3$) · H$_2$O · 2 C$_3$H$_6$O	[Ru((CF$_3$)$_2$-bpy)$_2$biimH$_2$]-(CO$_2$PhSO$_3$)
identification	BILMH2CF3_123K	AP_CF3_300K
formula	C$_{43}$H$_{36}$F$_{12}$N$_8$O$_8$Ru$_1$S$_1$	C$_{37}$H$_{22}$F$_{12}$N$_8$O$_5$Ru$_1$S$_1$
moiety formula	C$_{30}$ H$_{18}$ F$_{12}$ N$_8$ Ru, C$_7$ H$_4$O$_5$ S, 2(C$_3$ H$_6$ O), H$_2$ O	C$_{30}$ H$_{18}$ F$_{12}$ N$_8$ Ru, C$_7$ H$_4$O$_5$ S
formula weight	1153.92	1019.74
Z	2	2
calc. density [Mg m^{-3}]	1.59	1.503
F(000)	1016	1016
description + size of crystal [mm^3]	orange block (0.080 · 0.080 · 0.100)	red block (0.060 · 0.060 · 0.110)
abs. coeff. [mm^{-1}]	3.991	4.150
min/max transmission	0.50 / 0.73	0.58 / 0.78
T [K]	123	300
radiation [Å]	Cu Kα (λ = 1.54180)	Cu Kα (λ = 1.54178 Å)
crystal system	monoclinic	triclinic
space group	P 1 c 1	P 1
a [Å]	11.4686(10)	11.0765(6)
b [Å]	11.6843(11)	11.1214(6)
c [Å]	18.0917(16)	18.3747(9)
α [°]	90	92.487(3)
β [°]	95.541(4)	93.933(3)
γ [°]	90	93.919(3)
V [Å^3]	2413.0(4)	2250.3(2)
min/max Θ	3.783/ 66.618	2.413/ 69.645
collected refl.	24248	11105
indep. refl.	6599	11105
merging r	0.025	0.053
obs. refl.	6534 (I>2.0σ(I))	11078 (I>2.0σ(I))
ref. param.	558	1154
R	0.0450	0.0917
rW	0.1171	0.2505
gof	0.9166	1.0321

4.3.2 DFT calculations

Energy levels of molecular orbitals (MO) were calculated in the gas phase with DFT for the cationic complexes $[Ru(^tBu_2\text{-bpy})_2biimH_2]^{2+}$ and $[Ru((CF_3)_2\text{-bpy})_2biimH_2]^{2+}$ without counter-anions. Ground-state geometry optimization was carried out using the geometrical parameters of the cationic species in the single crystal structures of $[Ru(^tBu_2\text{-bpy})_2biimH_2](CO_2PhSO_3) \cdot 2$ $H_2O \cdot 2$ C_3H_6O (identification: BIlmH2tBu_ac_123K) and $[Ru((CF_3)_2\text{-bpy})_2biimH_2](CO_2PhSO_3) \cdot H_2O \cdot 2$ C_3H_6O (identification: BILMH2CF3_123K). This optimization was done with the hybrid exchange-correlation functional PBE1PBE[81] along with the relativistic basis set Lanl2dz[82] with effective core potentials. Optimized Ru-N distances are listed in Table 4-6. The energy level diagram and respective MO characteristics of $[Ru(^tBu_2\text{-bpy})_2biimH_2]^{2+}$ and $[Ru((CF_3)_2\text{-bpy})_2biimH_2]^{2+}$ are illustrated in Figure 4-7 and Table 4-7.

For the DFT calculations of MO energies of deprotonated complexes, one proton was removed from the biimidazole ligand, yielding the negatively charged, electron-rich biimH⁻ ligand and the complexes $[Ru(^tBu_2\text{-bpy})_2biimH]^+$ and $[Ru((CF_3)_2\text{-bpy})_2biimH]^+$.

Table 4-6 DFT calculated Ru-N bond lengths for the two $[Ru(R_2\text{-bpy})_2biimH_2]^{2+}$ complexes $(R = CF_3 \text{ and } R = {}^tBu)$.

R	bond	Bond Lengths [Å]	
		crystal structure	PBE1PBE/ Lanl2dz (Gas-Phase)
^{t}**Bu**	Ru-N^{bpy}	2.046(4)	2.070
		2.039(4)	2.061
		2.034(4)	2.061
		2.050(4)	2.069
	Ru-N^{biimH2}	2.103(4)	2.089
		2.089(4)	2.089
CF₃	Ru-N^{bpy}	2.030(4)	2.066
		2.031(6)	2.061
		2.041(4)	2.061
		2.048(4)	2.066
	Ru-N^{biimH2}	2.092(4)	2.094
		2.099(4)	2.094

$[Ru(^tBu_2\text{-bpy})_2biimH_2]^{2+}$ and $[Ru((CF_3)_2\text{-bpy})_2biimH_2]^{2+}$ show the HOMO mainly metal-centered with contributions of ligand associated π^* orbitals, illustrated in Figure 4-7. The LUMO of both complexes is mainly composed of π^* orbitals of the ligands. For $[Ru(^tBu_2\text{-bpy})_2biimH_2]^{2+}$ the LUMO exhibits equal contribution by all ligands, whereas the LUMO of

$[Ru((CF_3)_2\text{-bpy})_2biimH_2]^{2+}$ has only contributions from $(CF_3)_2$-bpy based π^* orbitals and from the metal-based d-orbital. Basically, no contribution of the $biimH_2$ π^* orbital is found in the MO calculation for the LUMO as well as for the energetically similar LUMO+1. LUMO+2 is the lowest excited state MO with $biimH_2$ contribution for $[Ru((CF_3)_2\text{-bpy})_2biimH_2]^{2+}$. It is approximately 6000 cm^{-1} higher in energy than the LUMO. This is similar to the $[Ru(bpy)_2pyimH]^{2+}$ where the bpy π^* orbitals also contribute to the energetically similar LUMO and LUMO+1, whereas LUMO+2 is significantly higher in energy and has pyimH π^* contributions.[83]

In $[Ru(^tBu_2\text{-bpy})_2biimH_2]^{2+}$ the orbitals LUMO, LUMO+1 and LUMO+2 are energetically close and exhibit major contribution of $biimH_2$ π^* orbital, except for LUMO+1, which is mainly bpy and metal centered. In total, the three lowest excited state MOs of $[Ru(^tBu_2\text{-bpy})_2biimH_2]^{2+}$ are higher in energy than those in $[Ru((CF_3)_2\text{-bpy})_2biimH_2]^{2+}$, predicting higher energy luminescence of $[Ru(^tBu_2\text{-bpy})_2biimH_2]^{2+}$ compared to $[Ru((CF_3)_2\text{-bpy})_2biimH_2]^{2+}$. This trend is due to lower $(CF_3)_2$-bpy π^* orbitals compared to $^tBu_2$-bpy and $biimH_2$ in these complexes.

In both biimidazole complexes the HOMO-LUMO transitions are comparable to classical MLCT transition of $[Ru(bpy)_3]^{2+}$ and $[Ru(bpy)_2pyimH]^{2+}$,[83,84] but with non-negligible LLCT character due to the contributions of $biimH_2$ π^*-orbitals to the HOMO, especially for $[Ru((CF_3)_2\text{-bpy})_2biimH_2]^{2+}$.

Upon deprotonation, this LLCT character is further enhanced in both complexes. In both cases, their HOMO is mostly located on metal centered d-orbitals and π^*-orbitals of the biimH$^-$ ligand. The lowest lying excited state orbitals are in both complexes bpy and metal centered as shown in Figure 4-8, Figure 4-9, Table 4-8 and Table 4-9. This effect is similar to the deprotonated $[Ru(bpy)_2pyimH]^{2+}$ complex.[83] The involvement of deprotonated imidazolyl ligands in the electronic properties is also known for ruthenium complexes with pyimH, $biimH_2$ and bibenzimidazole complexes. In all cases, the increased π-donor strength of the deprotonated ligand leads to increased HOMO energy compared to the fully protonated respective $biimH_2$ ligand. This effect results in a lower oxidation potential of the respective metal complex and decreases the energy difference between HOMO and LUMO, which results in a red shift in the absorption spectrum of the MLCT and LLCT and luminescence maximum, as shown in the following sections.[83,85,86]
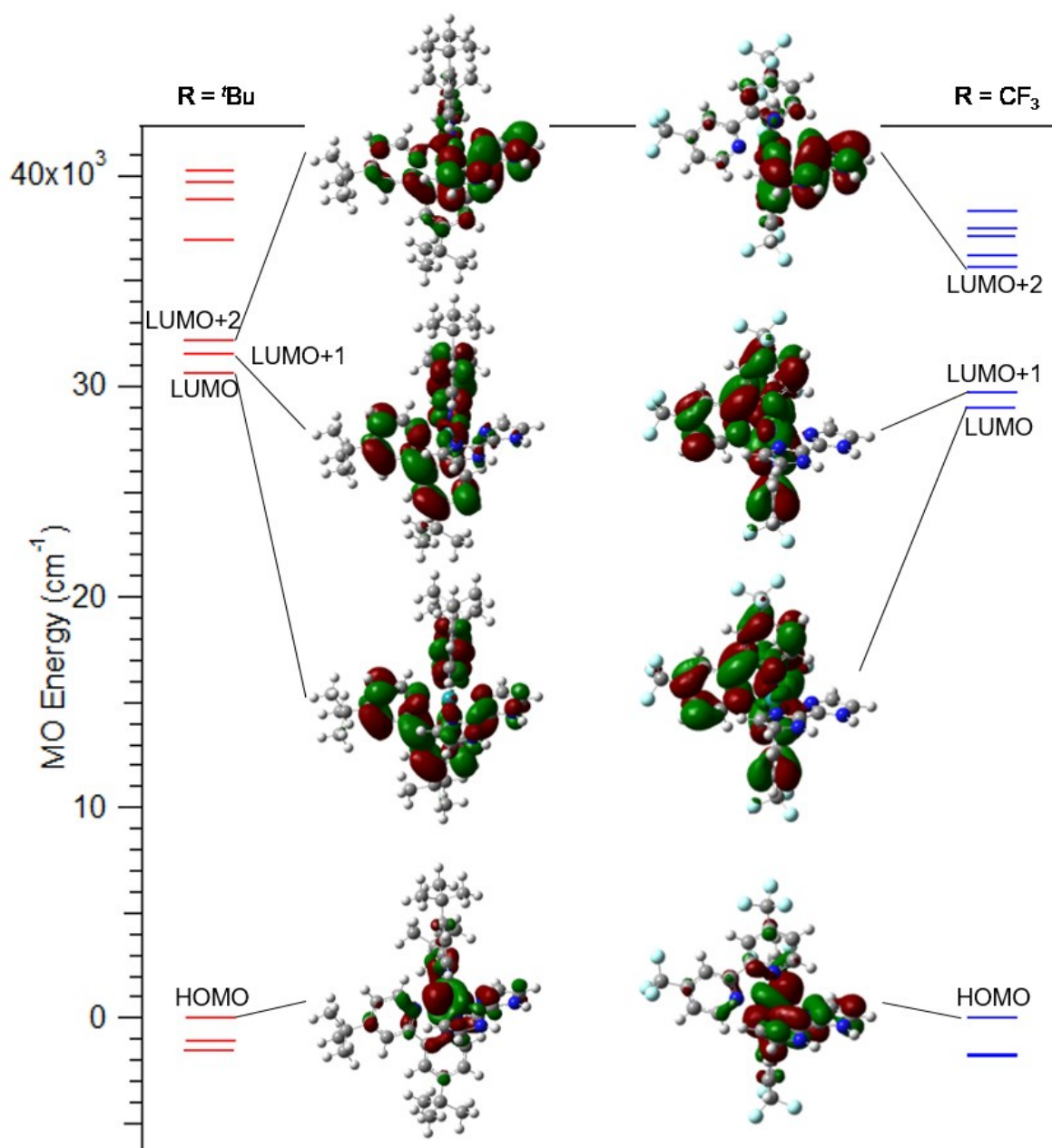
Figure 4-7 Molecular orbital energy for $[Ru(^tBu_2\text{-bpy})_2biimH_2]^{2+}$ (left) and $[Ru((CF_3)_2\text{-bpy})_2biimH_2]^{2+}$ (right) calculated in gas phase.

Table 4-7 MO contributions for $[Ru(R_2\text{-bpy})_2biimH_2]^{2+}$, minor contributions are in brackets.

	R = ^tBu	E [10^3 cm^{-1}]	R = CF$_3$	E [10^3 cm^{-1}]
LUMO+2	Ru-d, biimH$_2$ (bpy)	32.2	Ru-d, biimH$_2$, (bpy)	35.7
LUMO+1	Ru-d, bpy (biimH$_2$)	31.5	Ru-d, bpy	29.7
LUMO	bpy, biimH$_2$	30.6	Ru-d, bpy	29.0
HOMO	Ru-d (bpy, biimH$_2$)	0	Ru-d, biimH$_2$, (bpy)	0
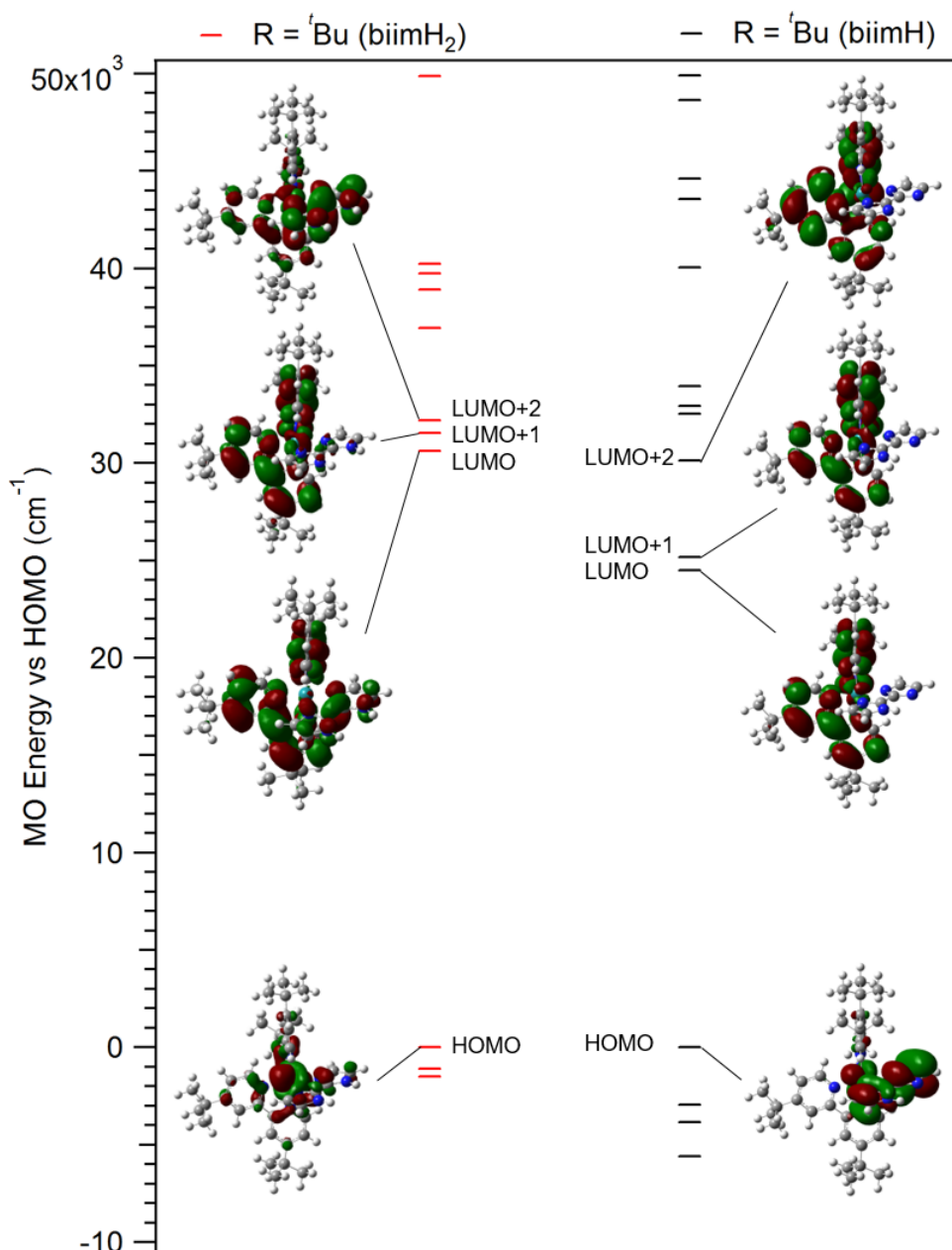
Figure 4-8 Effect of protonation state of the biimH$_2$ ligand on molecular orbital energy for [Ru(^{t}Bu$_2$-bpy)$_2$biimH$_2$]$^{2+}$ (left) and [Ru(^{t}Bu$_2$-bpy)$_2$biimH]$^+$ (right), calculated in gas phase.

Table 4-8 MO contributions for [Ru(^{t}Bu$_2$-bpy)$_2$biimH$_2$]$^{2+}$ in comparison to [Ru(^{t}Bu$_2$-bpy)$_2$biimH]$^+$, minor contributions are in brackets.

R = ^{t}Bu	biimH$_2$	E [10^3 cm^{-1}]	biimH	E [10^3 cm^{-1}]
LUMO+2	Ru-d, biimH$_2$ (bpy)	32.2	Ru-d, bpy	30.1
LUMO+1	Ru-d, bpy (biimH$_2$)	31.5	Ru-d, bpy	25.2
LUMO	bpy, biimH$_2$	30.6	Ru-d, bpy	24.5
HOMO	Ru-d (bpy, biimH$_2$)	0	Ru-d, biimH (bpy)	0
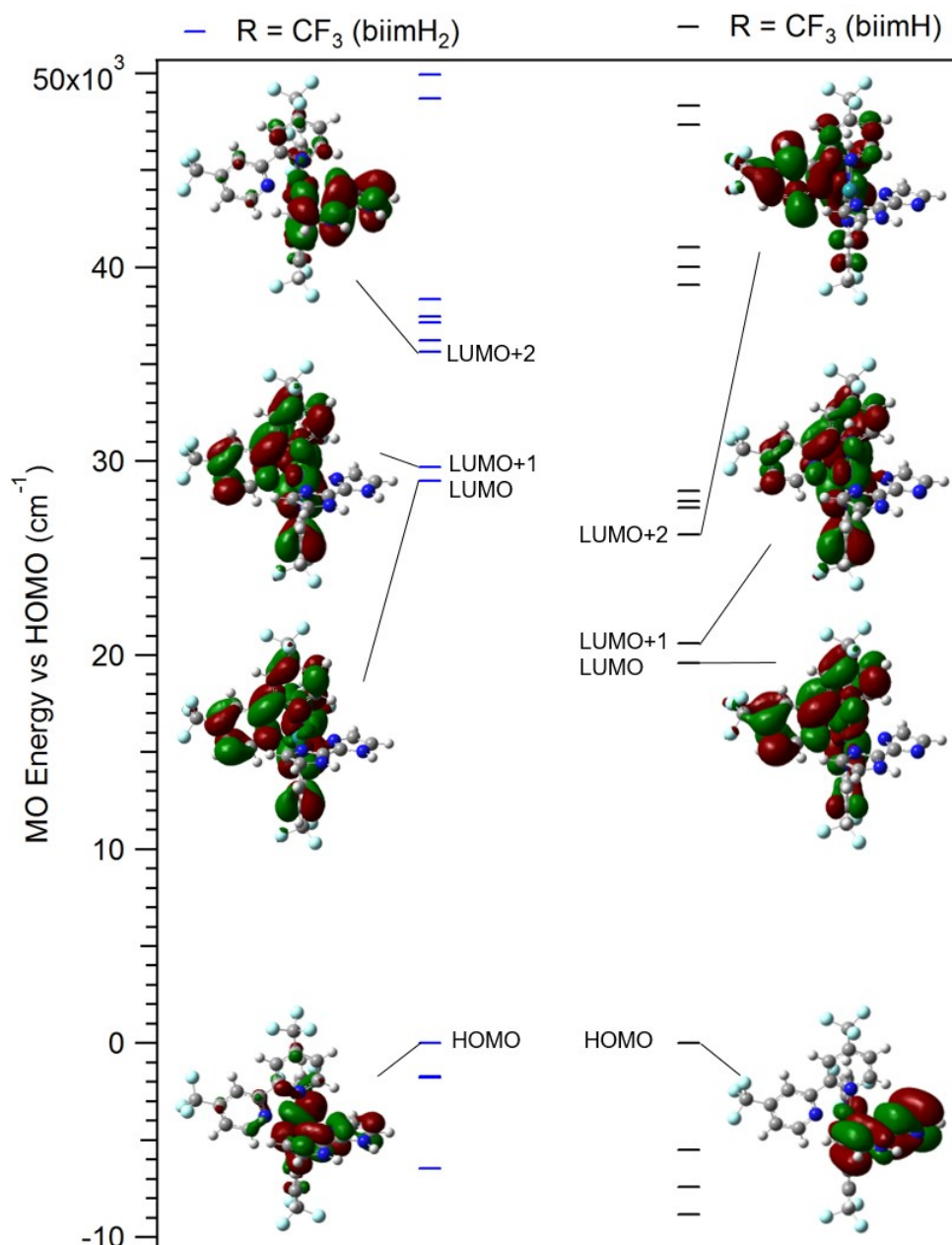
Figure 4-9 Effect of protonation state of the biimH$_2$ ligand on molecular orbital energy for [Ru((CF$_3$)$_2$-bpy)$_2$biimH$_2$]$^{2+}$ (left) and [Ru((CF$_3$)$_2$-bpy)$_2$biimH]$^+$ (right), calculated in gas phase.

Table 4-9 MOs contributions for [Ru((CF$_3$)$_2$-bpy)$_2$biimH$_2$]$^{2+}$ in comparison to [Ru((CF$_3$)$_2$-bpy)$_2$biimH]$^+$, minor contributions are in brackets.

R = CF$_3$	biimH$_2$	E [10^3 cm^{-1}]	biimH	E [10^3 cm^{-1}]
LUMO+2	Ru-d, biimH$_2$, (bpy)	35.7	bpy	26.2
LUMO+1	Ru-d, bpy	29.7	Ru-d, bpy	20.6
LUMO	Ru-d, bpy	29.0	Ru-d, bpy	19.6
HOMO	Ru-d, biimH$_2$, (bpy)	0	Ru-d, biimH	0

4.3.3 UV-vis Absorption Spectra in Solution
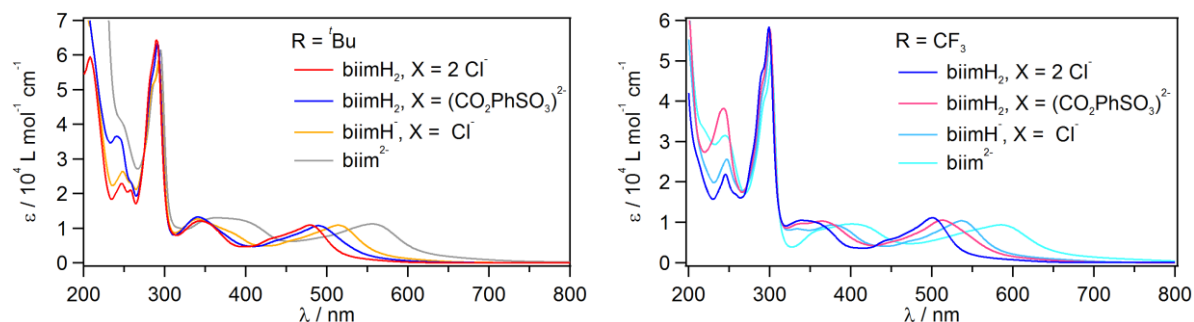
Figure 4-10 UV-vis absorption spectra of [Ru(R_2-bpy)$_2$biimH$_2$]X in MeCN with different protonation states of the biimH$_2$ ligand. Absorption of [Ru(R_2-bpy)$_2$biimH$_2$]Cl$_2$ was measured in presence of excess acid to ensure protonation. Deprotonation occurred by addition of TBAOH in MeCN. An attempt to capture the hydrogen bonding effect was made by dissolving crystalline [Ru(R_2-bpy)$_2$biimH$_2$](CO$_2$PhSO$_3$) in MeCN.

Absorption spectra in solution are similar for both [Ru(R_2-bpy)$_2$biimH$_2$]$^{2+}$ complexes and also similar to the absorption spectrum of [Ru(bpy)$_3$]$^{2+}$,[87] as seen in Figure 4-10. The band at around 20000 cm^{-1} (500 nm) in the absorption spectra with a molar absorptivity of 10000 M^{-1}cm^{-1} is assigned to an ensemble of MLCT and LLCT transitions, as identified with DFT calculations in section 4.3.2. Compared to [Ru(bpy)$_3$]$^{2+}$ the maximum of the MLCT absorption is at longer wavelength for the heteroleptic biimH$_2$ complexes, as seen in Table 3. The slightly longer wavelengths are due to the stronger π-donor properties of biimH$_2$ compared to bpy.[85] Upon deprotonation of the biimH$_2$ ligand, the absorption spectrum of both complexes shifts to the red by approximately 1400 cm^{-1} per deprotonation step.

Electron-withdrawing CF$_3$ substituents on the bpy ligands lower the π^* orbitals and therefore the energy of the bpy-localized MLCT excited states, as shown in DFT calculations in section 4.3.2 which explains that absorption of [Ru((CF$_3$)$_2$-bpy)$_2$biimH$_2$]$^{2+}$ is red-shifted by approximately 1000 cm^{-1} compared to [Ru(^{t}Bu$_2$-bpy)$_2$biimH$_2$]$^{2+}$.

A general red-shift of 400 cm^{-1} and 300 cm^{-1} upon hydrogen bonding is found for both complexes. This red-shift is typical for this type of complex upon hydrogen bonding or deprotonation.[69,83,85,88] The red-shift in both hydrogen bonded compounds does not correlate with isosbestic points that are found for deprotonation of the respective complexes. It therefore implies that the complexes are hydrogen bound to (CO$_2$PhSO$_3$)$^{2-}$ in acetonitrile solution. Upon hydrogen bonding, the biimidazole ligand becomes more electron rich as proton density is removed from the N-H bond. This leads to increased π donor strength of the biimidazole and therefore to an increase in HOMO energy. The resulting narrowing of HOMO and LUMO

orbitals, manifests in a red-shift in absorption. This effect is further increased by deprotonation of the biimH$_2$ ligand by external base, increasing the HOMO energy, as described in section 4.3.2.

Table 4-10 UV-vis absorption maxima of [Ru(R$_2$-bpy)$_2$biimH$_2$]X in MeCN with different protonation states of the biimH$_2$ ligand. [Ru(R$_2$-bpy)$_2$biimH$_2$]Cl$_2$ was measured in presence of excess acid to ensure protonation. Deprotonation occurred by addition of TBAOH in MeCN. The hydrogen bonding effect was captured by dissolving crystalline [Ru(R$_2$-bpy)$_2$biimH$_2$](CO$_2$PhSO$_3$) in MeCN.

R	ligand protonation state	X	E$_{max}$ in solution of MeCN [cm^{-1}] (λ_{max} in nm)
^{t}Bu	biimH$_2$	(CO$_2$PhSO$_3$)$^{2-}$	20410 (490)
	biimH$_2$	2 Cl$^-$	20830 (480)
	biimH$^-$	Cl$^-$	19460 (514)
	biim^{2-}		17990 (556)
CF$_3$	biimH$_2$	(CO$_2$PhSO$_3$)$^{2-}$	19490 (513)
	biimH$_2$	2 Cl$^-$	20000 (500)
	biimH$^-$	Cl$^-$	18622 (537)
	biim^{2-}		17090 (585)
[Ru(bpy)$_3$]$^{2+}$			22000 (455)[b]

4.3.4 Luminescence Spectroscopy at Ambient Pressure and Room Temperature

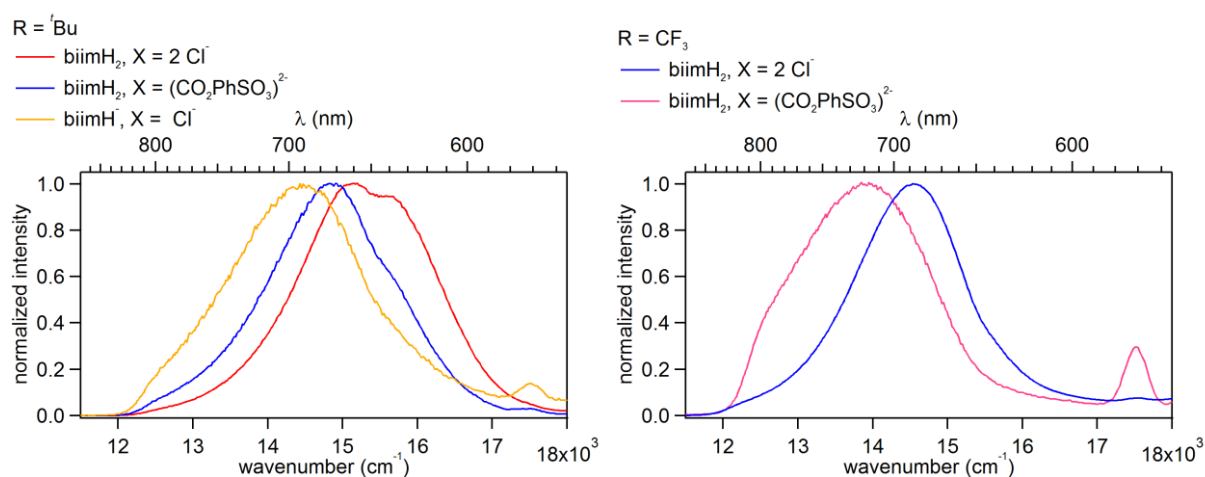**Figure 4-11** Luminescence spectra of $[Ru(R_2\text{-bpy})_2biimH_2]^{2+}$ in MeCN after excitation at 488 nm with different protonation states of the $biimH_2$ ligand. Deprotonation occurred by addition of TBAOH in MeCN. Luminescence of $[Ru(R_2\text{-bpy})_2biimH_2]Cl_2$ was measured in presence of excess acid to ensure protonation and the hydrogen bonding effect was attempted to be captured by dissolving crystalline $[Ru(R_2\text{-bpy})_2biimH_2](CO_2PhSO_3)$ in MeCN. The spectral feature at 650 nm is an instrumental artefact.

Luminescence spectra of the complexes at room temperature in acetonitrile solution have maxima at 15150 cm^{-1} (660 nm, R=^{t}Bu) and 14560 cm^{-1} (687 nm, R= CF$_3$) for fully protonated bimimidazole ligands. This is at lower energy compared to $[Ru(bpy)_3]^{2+}$ due to the π donor strength of the biimidazole ligand compared to bpy as discussed in previous sections. Hydrogen bonding to $(CO_2PhSO_3)^{2-}$ in solution results in red-shift of luminescence by 200 cm^{-1} and 300 cm^{-1} which is also observed in the respective absorption spectra. Single deprotonation of $[Ru(^tBu_2\text{-bpy})_2biimH_2]^{2+}$ leads to a red shift of luminescence maximum by 660 cm^{-1} to 14490 cm^{-1} (690 nm). The twofold deprotonated complex exhibits very weak luminescence intensity around 13000 cm^{-1} (760 nm), which is not shown in the spectrum, due to low signal-to noise resolution. Deprotonation of $[Ru(CF_3)_2\text{-bpy})_2biimH_2]^{2+}$ leads to disappearance of luminescence. Reduced intensity and depletion of luminescence upon deprotonation can be explained by a small energy difference between HOMO and LUMO upon deprotonation and therefore enhanced vibrational relaxation. In addition, the involvement of metal and ligand centered orbitals in HOMO and LUMO might further increase nonradiative deactivation pathways in the deprotonated, excited state complexes in solution. On the other hand, hydrogen bonding of the $biimH_2$ complex does not reduce luminescence significantly, because the hydrogen bond reduces N-H vibrations and therefore nonradiative decay pathways associated with N-H vibrations of the biimidazole ligand.[69,89]

In the solid state, the luminescence maxima of the hydrogen bonded complexes [Ru(^{t}Bu$_2$-bpy)$_2$biimH$_2$](CO$_2$PhSO$_3$) and [Ru((CF$_3$)$_2$-bpy)$_2$biimH$_2$](CO$_2$PhSO$_3$) are very similar to solution luminescence, as summarized in Table 4-11 and shown in Figure 4-12. The maximal difference between solution and solid state spectrum is 350 cm^{-1}, which contrasts with the blue-shift of the luminescence spectrum of [Ru(bpy)$_3$]$^{2+}$ by 950 cm^{-1} when going from solution to solid state.[87] A possible explanation for the small change in luminescence might be the LLCT character of the excited state opposed to the clear MLCT character of [Ru(bpy)$_3$]$^{2+}$ luminescence.

Solid state luminescence of [Ru(^{t}Bu$_2$-bpy)$_2$biimH$_2$]$^{2+}$ with Cl$^-$ counter ions differs from luminescence in solution and is red-shifted by 350 cm^{-1} compared to solution. The respective spectra of solid samples are shown in the following chapters. [Ru((CF$_3$)$_2$-bpy)$_2$biimH$_2$]Cl$_2$ is not further investigated in the solid state, because relevant effects at variable pressure and temperature are only observed in [Ru(^{t}Bu$_2$-bpy)$_2$biimH$_2$]$^{2+}$ which is therefore the focus of this study.

Table 4-11 Luminescence maxima at room temperature of [Ru(R$_2$-bpy)$_2$biimH$_2$]X in solution of MeCN and solid state. Solution luminescence spectra of [Ru(R$_2$-bpy)$_2$biimH$_2$]Cl$_2$ were measured in presence of excess acid to ensure protonation. Solution spectra of [Ru(R$_2$-bpy)$_2$biimH$_2$](CO$_2$PhSO$_3$) were recorded from crystalline samples, dissolved in MeCN. ^{a} From reference,[87] ^{b} From reference.[73]

Complex	E$_{max}$ in solution of MeCN [cm^{-1}] (λ_{max} in nm)	E$_{max}$ in solid state [cm^{-1}] (λ_{max} in nm)
[Ru(^{t}Bu$_2$-bpy)$_2$biimH$_2$](CO$_2$PhSO$_3$)	14860 (673)	14900 (671)
[Ru(^{t}Bu$_2$-bpy)$_2$biimH$_2$]Cl$_2$	15150 (660)	14800 (676)
[Ru(^{t}Bu$_2$-bpy)$_2$biimH]Cl	14490 (690)	
[Ru(CF$_3$)$_2$-bpy)$_2$biimH$_2$](CO$_2$PhSO$_3$)	13890 (720)	13800 (725)
[Ru(CF$_3$)$_2$-bpy)$_2$biimH$_2$]Cl$_2$	14560 (687)	-
[Ru(bpy)$_3$]$^{2+}$	16400 (610)^a	17350 (576)^b

4.3.5 Temperature Effects
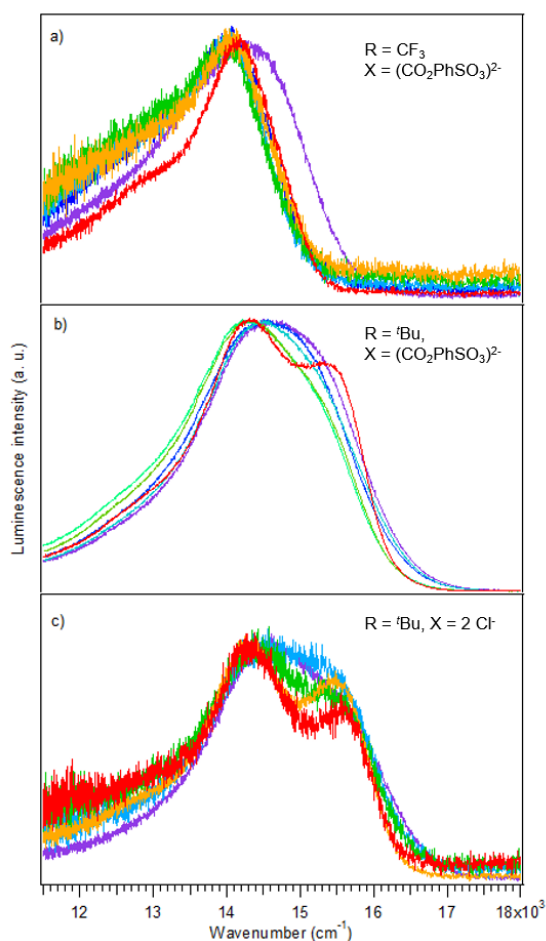
Figure 4-12 Normalized luminescence spectra of solid samples of a) [Ru((CF$_3$)$_2$-bpy)$_2$biimH$_2$](CO$_2$PhSO$_3$) at 80 (red), 100, 123, 180, 230 and 293 K (purple), b) [Ru(^{t}Bu$_2$-bpy)$_2$biimH$_2$](CO$_2$PhSO$_3$) at 80 (red), 123, 180, 230, 293, 303 and 313 K (purple), c) [Ru(^{t}Bu$_2$-bpy)$_2$biimH$_2$]Cl$_2$ at 80 (red), 123, 180, 230 and 293 K (purple).[90]

Luminescence spectra at temperatures between 80 K and 293 K of crystalline [Ru((CF$_3$)$_2$-bpy)$_2$biimH$_2$](CO$_2$PhSO$_3$), crystalline [Ru(^{t}Bu$_2$-bpy)$_2$biimH$_2$](CO$_2$PhSO$_3$) and powdered [Ru(^{t}Bu$_2$-bpy)$_2$biimH$_2$]Cl$_2$ are shown in Figure 4-12. Respective luminescence maxima at room temperature are summarized in Table 4-11. As general trend, band sharpening upon cooling is observed because vibrations are reduced at low temperature.

The band maximum of [Ru((CF$_3$)$_2$-bpy)$_2$biimH$_2$](CO$_2$PhSO$_3$) is at 14150 cm^{-1} and does not change significantly at different temperatures as presented in Figure 4-12a. A weak feature at 12800 cm^{-1} is resolved in the spectrum at 80 K and assigned to a vibrational side band.

Upon cooling of [Ru(^{t}Bu$_2$-bpy)$_2$biimH$_2$]$^{2+}$ the broad band at around 14900 cm^{-1} resolves into two maxima as shown in Figure 4-12b and Figure 4-12c. For the hydrogen bonded adduct [Ru(^{t}Bu$_2$-bpy)$_2$biimH$_2$](CO$_2$PhSO$_3$) the new band resolves only at very low temperature (80 K)

at 14300 cm^{-1} and 15300 cm^{-1}. The energy difference between maxima is 1000 cm^{-1} at 80 K, a value smaller than the expected energy separation for vibrational satellites. Regarding the shape of the band above 80 K, the higher energy maximum appears to blue-shift as temperature decreases, whereas the lower-energy maximum at 14300 cm^{-1} appears to be temperature independent, therefore temperature effects on the region lower than 14000 cm^{-1} are small.

For [Ru(^{t}Bu$_2$-bpy)$_2$biimH$_2$]$^{2+}$ with Cl$^-$ counterions (Figure 4-12c) the two peaks are resolved at 123 K, with maxima at 14300 cm^{-1} and 15500 cm^{-1}, corresponding to an energy difference of 1200 cm^{-1}. Qualitatively this is very similar to [Ru(^{t}Bu$_2$-bpy)$_2$biimH$_2$](CO$_2$PhSO$_3$) in Figure 4-12b.

The double maximum at low temperature is attributed to two different luminescent transitions, supported by the DFT calculations (see section 4.3.2). Multi-state emission from ruthenium(II) complexes with mixed ligands has been previously reported. [91,92]

It is noted that, apart from crystallinity, the main structural difference between the two investigated [Ru(^{t}Bu$_2$-bpy)$_2$biimH$_2$]$^{2+}$ compounds (X = Cl- and X = (CO$_2$PhSO$_3$)$^{2-}$) is the hydrogen bond at the biimidazole ligand which seems to affect the high-energy band of the luminescence. The hydrogen bonded complex exhibits this band 200 cm^{-1} more red-shifted compared to the non-hydrogen bonded powder sample of [Ru(^{t}Bu$_2$-bpy)$_2$biimH$_2$]Cl$_2$. This spectral observation is in line with performed DFT calculations, predicting that the LUMO, LUMO+1 and LUMO+2 orbitals compose of biimidazole dependent and biimidazole independent MOs, because the hydrogen bond can primarily influence the biimH$_2$ ligand orbitals, and not the bpy orbitals.

4.3.6   **Acidities**

Deprotonation of the biimH$_2$ ligand by the weakly basic (CO$_2$PhSO$_3$)$^{2-}$ counterion is in principle possible and evaluated for ground and excited state of [Ru(^{t}Bu$_2$-bpy)$_2$biimH$_2$]$^{2+}$ and [Ru((CF$_3$)$_2$-bpy)$_2$biimH$_2$]$^{2+}$ in the following section. It is noted that the following approximations are based on thermochemistry and luminescence in solution, which is only to limited extent applicable to the solid state. However, some trends are anticipated to hold true throughout any solvent and aggregation state, as described in the following.

Acidity constants of the ruthenium complexes were estimated, based on available values for [Ru(bpy)$_2$biimH$_2$]$^{2+}$ in water[85,93] and trends observed in structurally related [Ru(R$_2$-bpy)$_2$-pyimH]$^{2+}$ complexes with variable bpy spectator ligands as observed in chapter 2.[94]

The complex with R = ^{t}Bu is expected to be similarly acidic as the complex with unsubstituted bpy-spectator ligand which was shown for structurally related [Ru(R$_2$-bpy)$_2$pyimH]$^{2+}$ complexes.[94] The first deprotonation of the biimidazole ligand in the complex with R = ^{t}Bu is therefore expected to occur at pK$_{a1}$ = 7.2 ± 0.5 in aqueous solution.[85,93] The second deprotonation of the biimidazole ligand is expected at pK$_{a2}$ = 12.1 ± 0.5.[85,93]

The excited state acidity constant (pK$_a{}^*$) is estimated using the Förster equation with Planck's constant (h), the gas constant (R), temperature (T) and the wavenumbers ν_1 and ν_2 of the excited state energies of acid and conjugated base as described in section 1.4.[22]

$$pK_a{}^* = pK_a - \frac{h\nu_1 - h\nu_2}{2.3\ RT} \qquad (4\text{-}1)$$

Luminescence maxima from acetonitrile solution were inserted for ν_1 (fully protonated complex with biimH$_2$ ligand) and ν_2 (singly deprotonated complex with biimH$^-$ ligand), resulting in pK$_{a1}{}^*$ = 5.8 ± 1.

In the ground state, the biimidazole complex with R = CF$_3$ is expected to be more acidic than the complex with R = ^{t}Bu.[94] As a crude approximation the acidity constant is one pH unit lower than the complex with R = ^{t}Bu, yielding pK$_{a1}$ = 6.3 ± 1 and pK$_{a1}{}^*$ = 4.7 ± 1.

To evaluate acid-base equilibria between the complexes and the counterion, the acidity constant of the counterion's conjugated acid in water is assumed as pK$_a$ = 4.11.[95]

Table 4-12 [a] from reference,[95] [b] estimation from references as described in the text. [85,93,94] [c] calculated with the Förster equation as described in the text.

	pK$_a$	**pK$_a{}^*$**
(CO$_2$HPhSO$_3$)$^-$	4.11 [a]	
R = ^{t}Bu	7.2 ± 0.5 [b]	5.8 ± 1 [b, c]
R = CF$_3$	6.3 ± 1 [b]	4.7 ± 1 [b]

Based on estimated acidity constants in solution, the $[Ru(R_2\text{-bpy})_2\text{biimH}_2]^{2+}$ complexes are not deprotonated by $(CO_2PhSO_3)^{2-}$ at 1:1 concentration ratio in solution in the ground state. This was shown by absorption spectroscopy in acetonitrile solution.

Deprotonation at 1:1 molar ratio in the excited state also seems unlikely for the $[Ru(^tBu_2\text{-bpy})_2\text{biimH}_2]^{2+}$. However, regarding the approximated error ranges, the pK_a^* value of $[Ru((CF_3)_2\text{-bpy})_2\text{biimH}_2]^{2+}$ is close to the pK_a of the conjugated acid of the counterion.

The performed calculations are based on approximations for aqueous solution that are not necessarily correct for the crystalline state. The only trend that is expected to be applicable in the solid state is that the complex with R = CF_3 should be more acidic than the complex with R = ^tBu. This trend is supported by DFT calculations. The lowest LUMOs in $[Ru((CF_3)_2\text{-bpy})_2\text{biimH}_2]^{2+}$ are localized on the $(CF_3)_2$-bpy ligands which equals a charge transfer from ruthenium to the $(CF_3)_2$-bpy ligands and decreases electron density at the ruthenium and biimH$_2$ ligand in the excited state. The decrease in electron density at the ruthenium and biimH$_2$ ligand makes the biimH$_2$ ligand more acidic compared to the ground state. In contrast, the lowest excited state MOs of $[Ru(^tBu_2\text{-bpy})_2\text{biimH}_2]^{2+}$ are localized on the $^tBu_2$-bpy ligands *and* the biimH$_2$ ligand. This is expected to decrease the pK_a^* as well, because the metal center is formally oxidized. Due to biimH$_2$ ligand involvement in the lowest excited state MOs, the excited state of $[Ru(^tBu_2\text{-bpy})_2\text{biimH}_2]^{2+}$ is expected to be less acidic compared to $[Ru((CF_3)_2\text{-bpy})_2\text{biimH}_2]^{2+}$.

4.3.7 **Pressure Effects**

In the previous sections, it was shown that hydrogen bonds at the biimH$_2$ influence absorption and excited state properties in solution. It was also discussed that the excited state is influenced by the substituents on the bpy ligands, and, potentially, by acid-base chemistry. This section will reveal the effect of pressure-induced structure compression on the luminescence properties of these complexes with biimidazole ligands with and without hydrogen bonds.

Hydrostatic pressure was applied as described in the experimental section. Pressure-dependent X-ray diffraction on single crystals of [Ru(^{t}Bu$_2$-bpy)$_2$biimH$_2$](CO$_2$PhSO$_3$) revealed a phase transition from monoclinic at ambient pressure to triclinic at 2.1 kbar, whereas [Ru((CF$_3$)$_2$-bpy)$_2$biimH$_2$](CO$_2$PhSO$_3$) is in a triclinic unit ccell already at ambient pressure and undergoes a phase transition to monoclinic at around 12 kbar. The contraction of the unit cell volume upon pressure in these complexes is similar, namely -0.72 %kbar^{-1} and -0.84 %kbar^{-1} as listed in Table 4-13 and Table 4-14. It is noteworthy that the unit cell parameters at small pressure are already significantly reduced compared to ambient pressure. This might be due to a high compressibility of voids at low pressure. After the voids are minimized, compression becomes more difficult, because other structural features such as hydrogen bonds and metal-ligand bonds have to be shrinked.

Table 4-13 Pressure-induced change of unit cell parameters of [Ru(^{t}Bu$_2$-bpy)$_2$biimH$_2$]-(CO$_2$PhSO$_3$) single crystals.

^{t}Bu	p [kbar]	a [Å]	b [Å]	c [Å]	α [°]	β [°]	γ [°]	V [Å^3]
	2.1	11.254 (6)	18.005 (7)	24.161 (1)	87.20 (5)	83.46 (7)	85.04 (3)	4841.9
	12.0	10.993 (6)	17.814 (7)	23.299 (1)	86.74 (5)	82.07 (8)	85.31 (4)	4499.1
difference Δ	9.9	-0.262	-0.191	-0.862	-0.455	-1.393	0.261	-342.9
relative difference Δ [%]		-2.3	-1.1	-3.6	-0.5	-1.7	0.3	-7.1
ΔV / Δp [%kbar^{-1}]								-0.72

Table 4-14 Pressure-induced change of unit cell parameters of [Ru((CF$_3$)$_2$-bpy)$_2$biimH$_2$]-(CO$_2$PhSO$_3$) single crystals.

CF$_3$	p [kbar]	a [Å]	b [Å]	c [Å]	α [°]	β [°]	γ [°]	V [Å^3]
	5.8	10.739 (2)	10.926 (5)	17.861 (3)	92.68 (2)	96.77 (2)	95.12 (3)	2069.3
	12.8	10.241 (6)	10.839 (2)	17.989 (1)	90.00 (0)	102.80 (6)	90.00 (0)	1947.2
difference Δ	7.0	-0.498	-0.087	0.127	-2.68	6.03	-5.12	-122.1
relative difference Δ [%]		-4.6	-0.8	0.7	-2.9	6.2	-5.4	-5.9
ΔV / Δp [%kbar^{-1}]								-0.84

The pressure setup for optical spectroscopy allowed the measurement of luminescence and Raman spectra at identical samples and pressure. Raman spectra are presented in section 4.6. They show no significant changes in the respective pressure range, indicating that the complexes stay intact over the entire explored pressure range. The luminescence of the complexes was monitored in the pressure range between 0 and 55 kbar. Respective luminescence spectra and the shift of their maxima is presented in Figure 4-13.

The luminescence spectra of [Ru((CF$_3$)$_2$-bpy)$_2$biimH$_2$](CO$_2$PhSO$_3$) at pressures between 0 and 38 kbar remain similar in shape over the entire pressure range. The luminescence maximum shifts by $\Delta E_{max}/\Delta p$ = +3 ± 1 cm^{-1}kbar^{-1}, as seen with the green trace in Figure 4-13a. This indicates that pressure has a minor influence on the transition energy in this particular complex over the entire pressure range. This is similar to the minor luminescence shift of -2 cm^{-1}kbar^{-1}of [Ru(bpy)$_3$](PF$_6$)$_2$ at pressures below 20 kbar.[73] It also supports the DFT calculations from section 4.3.2 indicating that luminescence in this complex involves mainly the bpy based LUMO and LUMO+1 for the fully protonated and singly deprotonated complex. The metal contribution to the LUMOs and biimidazole contribution to the HOMO might lead to the slight deviation from ideal ^{3}MLCT behavior at high pressure as found in [Ru(bpy)$_3$](PF$_6$)$_2$.[73]
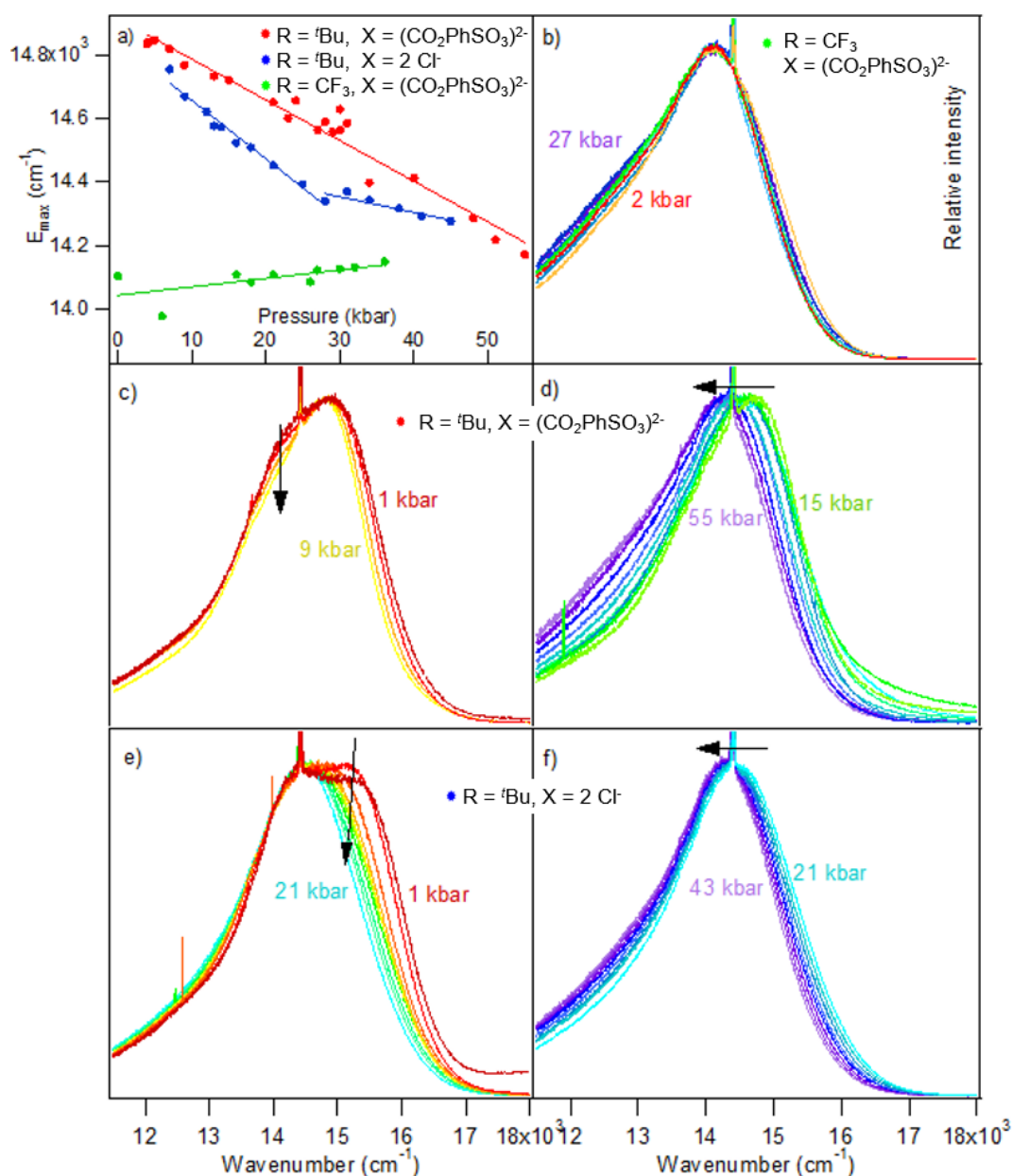
Figure 4-13 Changes in solid state luminescence with pressure of $[Ru(R_2\text{-bpy})_2biimH_2]X$. a) Evolution of maxima for all complexes with following slopes: -13 ± 1 cm^{-1}kbar^{-1} (red, R= ^{t}Bu, X = $(CO_2PhSO_3)^{2-}$), -18 ± 1 cm^{-1}kbar^{-1}and -5 ± 1 cm^{-1}kbar^{-1} (blue, R= ^{t}Bu, X = 2 Cl$^-$), $+3 \pm 1$ cm^{-1}kbar^{-1} (green, R= CF$_3$, X = $(CO_2PhSO_3)^{2-}$). (b-f) luminescence spectra at various pressures: (b) $[Ru((CF_3)_2\text{-bpy})_2biimH_2](CO_2PhSO_3)$ (c, d) $[Ru(^tBu_2\text{-bpy})_2biimH_2](CO_2PhSO_3)$ from 1 to 9 kbar (d) and from 15 to 55 kbar (e,f) $[Ru(^tBu_2\text{-bpy})_2biimH_2]Cl_2$ from 1 to 21 kbar (f) and from 21 to 43 kbar (f). Selected pressure ranges are chosen to show decrease of intensity on the side of the spectra (left) and the shift of the luminescence spectra (right).[90]
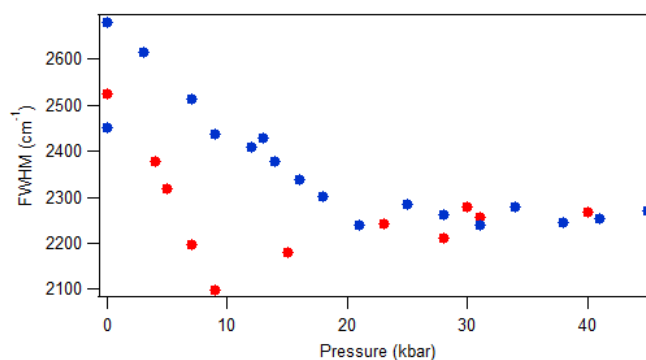
Figure 4-14 FWHM of luminescence bands of crystalline [Ru(^{t}Bu$_2$-bpy)$_2$biimH$_2$](CO$_2$PhSO$_3$) (red) and powdered [Ru(^{t}Bu$_2$-bpy)$_2$biimH$_2$]Cl$_2$ (blue) as a function of pressure.

For the complexes with ^{t}Bu substituents, stronger luminescence shifts are observed. For the ^{t}Bu complex with the hydrogen bonded (CO$_2$PhSO$_3$)$^{2-}$ counter ion, the pressure-induced shift $\Delta E_{max}/\Delta p$ is -13 ± 1 cm^{-1}kbar^{-1} over the entire pressure range (red trace in Figure 4-13a), which is distinctly more negative than the -2 cm^{-1}kbar^{-1} reported for [Ru(bpy)$_3$](PF$_6$)$_2$.[73] When comparing this broad luminescence band at ambient pressure with the low temperature spectra of this complex, it consists of two overlapping bands. The low energy band at 14300 cm^{-1} seems to vanish, while the high-energy band shifts to the red. Between 9 kbar and 55 kbar the high-energy band shifts uniformly with the same slope as before. The change of shape of the luminescence band was captured in a plot of full-width at half maximum (FWHM) vs. pressure in Figure 4-14 (red). The two bands can be assigned to transitions, involving the energetically similar LUMO and LUMO+1 or LUMO+2 of the fully protonated complex, described with the DFT calculations in section 4.3.2.

In the [Ru(^{t}Bu$_2$-bpy)$_2$biimH$_2$]$^{2+}$ complex with Cl$^-$ counter ions no hydrogen bonds with (CO$_2$PhSO$_3$)$^{2-}$ are present. A shift of luminescence maximum of -18 ± 1 cm^{-1}kbar^{-1} is found between ambient pressure and 28 kbar as shown in the blue trace in Figure 4-13a. A very strong change in shape is observed in this pressure range as well (Figure 4-13e). The high-energy band seems to lose intensity, which induces the relatively strong net-shift of the maximum by -18 ± 1 cm^{-1} kbar^{-1} and sharpening of the band, which also manifests in the FWHM vs. pressure plot in Figure 4-14 (blue). At pressures above 21 kbar, the band shape remains constant and the maximum shifts with a minor slope of -5 ± 1 cm^{-1} kbar^{-1}, which is, again, similar to luminescence shift of [Ru(bpy)$_3$](PF$_6$)$_2$ in this pressure range.[73]

4.3.8   **Discussion of Proton Transfer vs. LUMO Effects**

During the course of this study two possible explanations for the difference in pressure dependent luminescence between [Ru(^{t}Bu$_2$-bpy)$_2$biimH$_2$](CO$_2$PhSO$_3$) and [Ru((CF$_3$)$_2$-bpy)$_2$-biimH$_2$](CO$_2$PhSO$_3$) were found.

The first theory is based on a shift in acid-base equilibrium in [Ru(^{t}Bu$_2$-bpy)$_2$biimH$_2$](CO$_2$PhSO$_3$) at higher pressure towards deprotonation of the biimH$_2$ ligand by (CO$_2$PhSO$_3$)$^{2-}$. In solution, the luminescence of deprotonated [Ru(R$_2$-bpy)$_2$biimH$_2$]$^{2+}$ is strongly reduced or depleted. However, crystallinity and hydrogen bonds in such adducts usually decrease nonradiative vibrational relaxation pathways and therefore increase luminescence intensity.[69,89] The excited state of the complex is anticipated to be more acidic compared to the ground state, the acid-base equilibrium shift is expected rather in the excited state than in the ground state. In both electronic states, deprotonation leads to increased HOMO energy due to enhanced π-donor strength of the biimH$^-$-ligand (see section 4.3.2). Such a shift in the acid-base equilibrium would lead to a red-shift in luminescence. This is indeed observed for both compounds of [Ru(^{t}Bu$_2$-bpy)$_2$biimH$_2$]$^{2+}$. This red-shift could also be explained by strengthening of the hydrogen bonds with increased proton-affinity of the carboxylate compared to the biimidazole at low pressure. Proton transfer and strengthened hydrogen bonding in the solid state at high pressure was observed previously in amino acids and between the 1:1 adduct of 4,4'-bipyridinium and squaric acid in the ground state.[96,97]

In the luminescence spectra, it was observed that one luminescence band vanishes at pressure above 9 kbar. Vanishing of one band in the luminescence spectrum of [Ru(^{t}Bu$_2$-bpy)$_2$biimH$_2$](CO$_2$PhSO$_3$) at high pressure can be explained by a changeover in the character of the lowest excited state MOs. In the singly deprotonated state complex, LUMO, LUMO+1 and LUMO+2 are ^{t}Bu$_2$-bpy and metal centered and no contribution of the biimidazole ligand is found, unlike in the fully protonated form. Therefore, the biimH$_2$-contribution to the LUMO is anticipated to vanish as pressure increases. At the same time, the biimH$^-$ contribution to the HOMO increases, reducing the HOMO-LUMO gap.

For [Ru((CF$_3$)$_2$-bpy)$_2$biimH$_2$](CO$_2$PhSO$_3$) no such luminescence shift was observed at increased pressure. The hydrogen bond between the biimidazole and the carboxylate is already strong in the ground state, as revealed by very short N⋯O distances in the solvent-free structure in section 4.3.1. Based on the argumentation about acidities in section 4.3.5, it is conceivable that the acid base equilibrium in this hydrogen-bonded adduct is shifted towards the deprotonated complex and protonated counterion in the hydrogen bonded adduct in the excited state at ambient pressure.
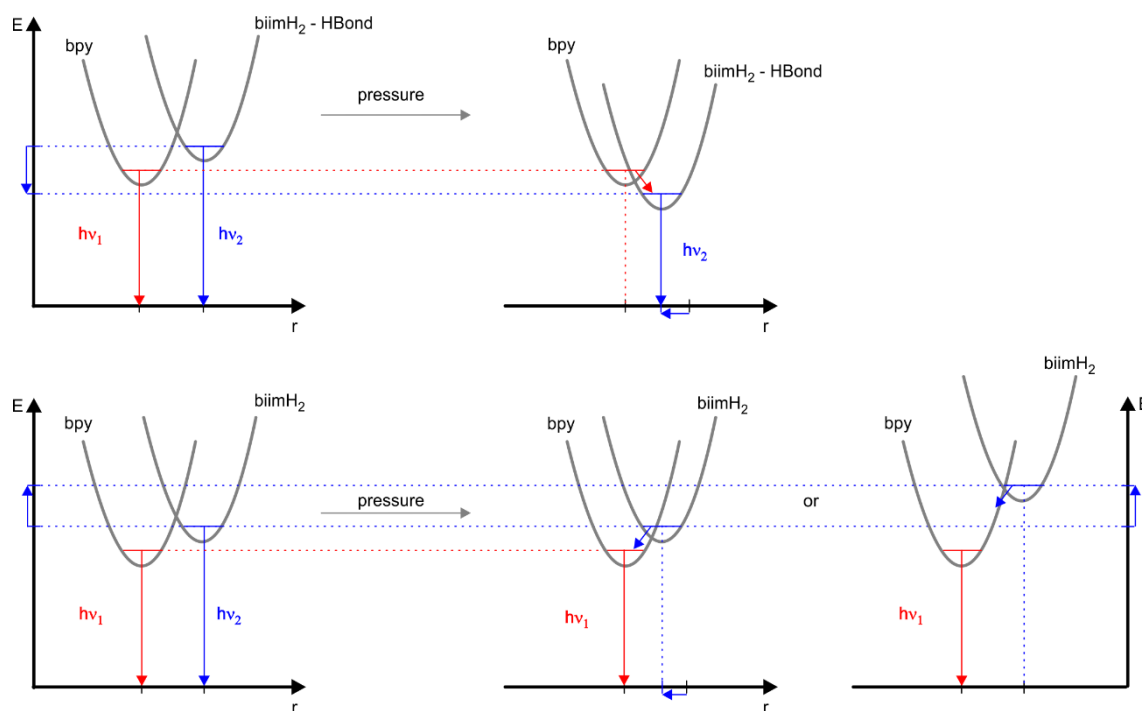
Figure 4-15 Schematic representation of changes of LUMO energies relative to HOMO energy at high pressure for top) the hydrogen bonded adduct $[Ru({}^tBu_2\text{-}bpy)_2biimH_2](CO_2PhSO_3)$ and bottom) $[Ru({}^tBu_2\text{-}bpy)_2biimH_2]Cl_2$.

In the second theory, the acid-base equlibrium remains constant over the entire pressure range with the $biimH_2$ ligands maintaining the proton at the N-donors. This implies that the HOMO energy remain approximately constant . The red-shift of luminescence maximum in the complexes with R = ${}^tBu_2$ would then be due to the shift of a biimidazole based LUMO-orbital, because bpy based LUMOs would result in a small shifting, as observed for $[Ru((CF_3)_2\text{-}bpy)_2\text{-}biimH_2](CO_2PhSO_3)$ and $[Ru(bpy)_3](PF_6)_2$ and in the high pressure range of $[Ru({}^tBu_2\text{-}bpy)_2biimH_2]Cl_2$.[73]

A qualitative representation of the observed luminescence change in crystalline $[Ru({}^tBu_2\text{-}bpy)_2biimH_2](CO_2PhSO_3)$ is sketched in Figure 4-15(top): The bpy-based LUMO stays constant in energy and the $biimH_2$-involved LUMO shifts red. Because of vibrational interactions between both energy levels, the bpy based LUMO is depopulated and converts into the $bimH_2$ based orbital as the pressure increases. For $[Ru({}^tBu_2\text{-}bpy)_2biimH_2]Cl_2$ Figure 4-15 (bottom) a different behavior is concluded because luminescence from the bpy based LUMO is observed, as described previously. This suggests that at high pressure, the bpy based LUMO dominates the spectroscopy and the $biimH_2$ based luminescence vanishes (Figure 4-13e). This might be due to enhanced internal conversion from the $biimH_2$ based MO into the bpy based

MO because of vibrational overlap of these two energy levels at high pressure. This might be induced by either narrowing of both energy levels or energetic destabilization of the biimH$_2$-based MO relative to the HOMO. Both possibilities are sketched in Figure 4-15 (bottom).

The open question within this theory is: Why is the hydrogen bonded biimH$_2$-involved LUMO shifted to lower energy at higher pressure? A red-shift is usually associated with either an up-shift of HOMO energy, or a down-shift of LUMO energy or a combination of both. If the HOMO-energy was shifted up, this would also manifest in a red-shift of the bpy-based luminescence bands for all investigated complexes. But since no red-shift of bpy-based luminescence in neither [Ru((CF$_3$)$_2$-bpy)$_2$biimH$_2$](CO$_2$PhSO$_3$), nor the high pressure range of [Ru(^{t}Bu$_2$-bpy)$_2$biimH$_2$]Cl$_2$ was found, it is concluded that the HOMO does not shift. Therefore, the red-shift is associated with stabilization of the biimH$_2$-involved MO. Stabilization of this MO is normally associated with decreased net-electron density in this orbital. By contrast, the hydrogen bond in this N-H$\cdots$O motif increases net-electron density at the biimH$_2$ ligand as it partially delocalizes the N-H proton into the hydrogen bond. On the other hand, approaching of the dianion towards the biimH$_2$ ligand would also increase electron density at the biimH$_2$. Other hypotheses are the following:

- Stabilization of the LUMO might be induced by increased proton density at the biimidazole upon increased pressure. This would mean that the carboxylate pushes the protons within the hydrogen bond closer to the N-donor, therefore acting like a piston.

- Another possible explanation is that compression in the structure increases the interactions between the dianionic (CO$_2$PhSO$_3$)$^{2-}$ and the bpy ligands, therefore rendering them more electron rich and favoring the biimH$_2$ involved MOs. This theory is in conflict with the conclusion that bpy-based MOs do not shift significantly.

- A third possibility is the increased interaction of the positively charged metal center with the biimH$_2$ involved MO as it is already predicted for ambient pressure in LUMO+2. This would stabilize the biimH$_2$-involved MO. The drawback of this theory is that it would probably enhance nonradiative decays via d-d interactions at the metal center.

4.4   Conclusions

The secondary coordination sphere effects on the electronic excited state was investigated for $[Ru(R_2\text{-bpy})_2biimH_2]^{2+}$ that can form hydrogen bonds between the $biimH_2$ ligand and the carboxylate function of the dianion $(CO_2PhSO_3)^{2-}$. The pressure induced red-shift in the complex with R = ^{t}Bu can be explained by either a shift in the excited state acid-base equilibrium within the hydrogen bond, or pressure-induced stabilization of hydrogen bonded $biimH_2$ based LUMOs. Stabilization of $biimH_2$ based LUMOs would take place via pushing the protons within the hydrogen bond closer to the N-donor. In the complex with R = CF_3 luminescence is only slightly affected by pressure, either because deprotonation occurs already at ambient pressure, or because its LUMO orbitals are bpy based and therefore not sensitive to pressure effects.

4.5   Experimental Section

4.5.1   Synthesis and Crystallization

All commercially available chemicals were used as received. The following materials were synthesized as described previously: [Ru((CF_3)$_2$-bpy)$_2$Cl$_2$],[98] 2,2'-biimidazole,[68] and [Ru(^{t}Bu$_2$-bpy)$_2$Cl$_2$].[99] An aqueous 0.76 M Na,K(CO$_2$PhSO$_3$) solution was prepared by dissolving commercially available 4-sulfobenzoic acid potassium salt (K(CO$_2$HPhSO$_3$)) (1.83 g, 7.6 mmol) in 0.76 M NaOH (10 mL, 7.6 mmol), yielding 0.76 M Na,K(CO$_2$PhSO$_3$) solution.

4.5.1.1   [Ru(^{t}Bu$_2$-bpy)$_2$biimH$_2$]Cl$_2$

[Ru(^{t}Bu$_2$-bpy)$_2$Cl$_2$] (100 mg, 141 µmol, 1.00 eq.) and biimidazole (24.0 mg, 176 µmol, 1.25 eq.) were heated in a degassed mixture of water (5 mL) and dichloromethane (5 mL) at reflux for 16 h. The solvent was removed and the remaining solid was taken up in 10 mL acetone. The insoluble ligand was removed by filtration. The red filtrate was dried in vacuo, yielding [Ru(^{t}Bu$_2$-bpy)$_2$biimH$_2$]Cl$_2$·3.5 H$_2$O as a red solid (118 mg, 141 µmol, quant.).

^{1}H NMR (400 MHz, CD$_3$CN): δ (ppm) = 8.42 (dd, J = 4.7, 2.0 Hz, 4H), 7.85 (dd, J = 6.0, 0.6 Hz, 2H), 7.69 (dd, J = 6.0, 0.6 Hz, 2H), 7.45 (dd, J = 6.0, 2.1 Hz, 2H), 7.31 (dd, J = 6.1, 2.1 Hz, 2H), 7.27 (d, J = 1.5 Hz, 2H), 6.36 (d, J = 1.5 Hz, 2H), 1.43 (s, 18H), 1.39 (s, 18H).

EA: (%) calculated for C$_{42}$H$_{54}$Cl$_2$N$_8$Ru · 3.5 H$_2$O: C 55.68, H 6.79, N 12.37; found: C 55.29, H 6.70, N 12.81.

ESI-HRMS: (m/z) calculated for C$_{42}$H$_{54}$N$_8$Ru: 386.1757; found: 386.1763 [M]$^{2+}$; calculated for C$_{42}$H$_{53}$N$_8$Ru: 771.3442; found: 771.3445 [M-H]$^+$.

4.5.1.2   [Ru(^{t}Bu$_2$-bpy)$_2$biimH$_2$](CO$_2$PhSO$_3$)

Single crystals were obtained by slow diffusion of equimolar amounts of [Ru(^{t}Bu$_2$-bpy)$_2$biimH$_2$]Cl$_2$ in acetone into a layer of 0.74 M aqueous Na,K(CO$_2$PhSO$_3$) with equimolar amounts of [Ru(^{t}Bu$_2$-bpy)$_2$biimH$_2$]Cl$_2$. To achieve slow diffusion, the aqueous layer was preloaded into an NMR tube and frozen via ice-cooling. The organic phase was cooled to 0° C and layered cautiously over the frozen aqueous phase. The loaded tube was then stored at +5°C. After several days, the tube was removed from the fridge and stored at room temperature, which yielded single crystals.

^{1}H NMR (400 MHz, CD$_3$CN): δ (ppm) = 8.44 – 8.37 (m, 4H), 8.00 (d, J = 8.5 Hz, 2H), 7.88 (d, J = 6.1 Hz, 2H), 7.75 (d, J = 8.4 Hz, 2H), 7.71 (d, J = 6.0 Hz, 2H), 7.45 (dd, J = 6.0,

2.0 Hz, 2H), 7.32 (dd, J = 6.1, 2.0 Hz, 2H), 7.27 (d, J = 1.4 Hz, 2H), 6.34 (d, J = 1.4 Hz, 2H), 1.42 (s, 18H), 1.40 (s, 18H).

4.5.1.3 [Ru((CF₃)₂-bpy)₂biimH₂]Cl₂[98]

[Ru((CF$_3$)$_2$-bpy)$_2$Cl$_2$] (71 mg, 93 µmol, 1.00 eq.) and biimidazole (24.1 mg, 180 µmol, 1.90 eq.) were heated in a degassed mixture of water (5 mL) and ethanol (5 mL) at reflux for 16 h. After cooling to room temperature 0.5 mL concentrated HCl were added. The solvent was removed and the remaining solid was taken up in 10 mL acetone. The insoluble ligand was removed by filtration. The red filtrate was dried in vacuo, yielding [Ru((CF$_3$)$_2$-bpy)$_2$biimH$_2$]Cl$_2$ as a red solid (62.8 mg, 76.6 µmol, 83 %).

¹H NMR (400 MHz, CD₃CN): δ 8.89 (d, J = 10.1 Hz, 4H), 8.21 (d, J = 6.1 Hz, 2H), 8.09 (d, J = 5.8 Hz, 2H), 7.76 (dd, J = 6.1, 1.1 Hz, 2H), 7.60 (dd, J = 6.0, 1.3 Hz, 2H), 7.31 (d, J = 1.5 Hz, 2H), 6.46 (d, J = 1.5 Hz, 2H).

EA: (%) calculated for $C_{30}H_{18}Cl_2F_{12}N_8Ru$ · 3 H_2O: C 38.15, H 2.56, N 11.86; found: C 38.55, H 2.94, N 12.14.

ESI-HRMS: (m/z) calculated for $C_{30}H_{18}F_{12}N_8Ru^{2+}$: 410.0251; found: 410.0253 [M]$^{2+}$; calculated for $C_{30}H_{17}F_{12}N_8Ru$: 819.0430, found: 819.0412 [M-H]$^+$.

4.5.1.4 [Ru((CF₃)₂-bpy)₂biimH₂](CO₂PhSO₃)

[Ru((CF$_3$)$_2$-bpy)$_2$biimH$_2$]Cl$_2$ (20 mg, 24.3 µmol, 1.00 eq.) and aqueous 0.74 M Na,K(CO$_2$PhSO$_3$) (24.3 µmol, 1.00 eq.) were combined in a mixture of acetone and water. Single crystals were grown by diethyl ether diffusion at 5 °C.

¹H NMR (400 MHz, CD₃CN): δ 8.91 – 8.84 (m, 4H), 8.22 (d, J = 5.9 Hz, 2H), 8.13 – 8.06 (m, 2H), 8.01 (d, J = 8.1 Hz, 2H), 7.75 (dt, J = 6.4, 1.3 Hz, 4H), 7.60 (ddd, J = 6.0, 2.0, 0.8 Hz, 2H), 7.29 (s, 2H), 6.42 (d, J = 1.4 Hz, 2H).

EA: (%) calculated for $C_{37}H_{22}F_{12}N_8O_5RuS$: C 42.46, H 2.41, N 10.70; found: C 49.32, H 2.63, N 10.99.

ESI-HRMS: (m/z) calculated for $C_{30}H_{18}F_{12}N_8Ru^{2+}$: 410.0251; found: 410.0252 [M]$^{2+}$; calculated for $C_{30}H_{17}F_{12}N_8Ru$: 819.0430, found: 819.0415 [M-H]$^+$, calculated for $C_7H_5O_5S^-$: 200.9863; found: 200.9866 [CO$_2$PhSO$_3$+H]$^-$.

4.5.2 Crystallography

Single crystals were removed from the mother liquor and selected for diffraction using the oil Paratone 8006. Single crystals were measured on a Bruker Kappa Apex2 diffractometer at 123 K using graphite-monochromated Cu-Kα radiation with λ = 1.5418 Å. The Apex software was used for data collection and integration. The structures were solved by the charge-flipping method using the program Superflip. [100] Least-squares refinement against F^2 using all reflections was carried out on all non-hydrogen atoms using the program Crystals.[101] SQUEEZE[102] procedure was used to treat the solvent region of $[Ru((CF_3)_2\text{-bpy})_2biimH_2]$-$(CO_2PhSO_3) \cdot H_2O \cdot 2\,C_3H_6O$ (identification: BILMH2CF3_123K). Plots were produced using Mercury.[103] Crystallography at high pressure was conducted with the setup described in section 4.5.5 and in literature.[96]

4.5.3 Computational Details

All DFT calculations, unless otherwise stated, were performed with the Gaussian 09 software package (Revision D.01, Gaussian Inc.)[104] using methods as implemented in the mentioned revision. Both compounds were modeled as cationic complexes without any counter ion in the isolated molecule approximation (gas-phase). First of all, a ground-state geometry optimization was carried out using the crystal structure geometrical parameters (bond lengths, angles and dihedral angles) of the crystal structures $[Ru(^tBu_2\text{-bpy})_2biimH_2](CO_2PhSO_3) \cdot 2\,H_2O \cdot 2\,C_3H_6O$ (identification: BIlmH2tBu_ac_123K) and $[Ru((CF_3)_2\text{-bpy})_2biimH_2](CO_2PhSO_3) \cdot H_2O \cdot 2\,C_3H_6O$ (identification: BILMH2CF3_123K) respectively as starting parameters. This optimization was done with the hybrid exchange-correlation functional PBE1PBE[81] along with the relativistic basis set Lanl2dz[82] with effective core potentials. A frequency calculation was undertaken at the same level of theory on the obtained optimized structures and revealed no imaginary frequencies. Molecular orbitals were also calculated for these optimized structures and were visualized with the 5.09 release of the GaussView software (Gaussian Inc.)[104] with an isovalue of 0.02 atomic units.

4.5.4 Spectroscopy

Electronic absorption measurements in solution were performed in HPLC grade acetonitrile solution on a Cary 5000 instrument from Varian. Luminescence spectra in acetonitrile solution were performed on a Fluorolog-3 apparatus from Horiba Jobin-Yvon. Samples were excited at

488 nm. Full protonation of $[Ru(R_2\text{-bpy})_2biimH_2]Cl_2$ was ensured by addition of 10 µL concentrated aq. HCl to the 2 mL sample volume in the cuvette. Deprotonation occurred by addition of TBAOH solution in acetonitrile.

Luminescence and Raman spectra of the crystalline form of $[Ru((CF_3)_2\text{-bpy})_2biimH_2]^{2+}$, $[Ru(^tBu_2\text{-bpy})_2biimH_2]^{2+}$ with Cl^- counter ions and $[Ru((CF_3)_2\text{-bpy})_2biimH_2]^{2+}$ with $(CO_2PhSO_3)^{2-}$ counter ions were measured with Renishaw Invia imaging microscope. An argon ion laser with a wavelength of 488 nm was used for all luminescence spectra. Raman spectra were measured with an excitation wavelength of 785 nm. For measurements at variable temperature, a Linkam gas-flow microcryostat system was used. For measurements at variable pressure, a gasgeted diamond-anvil cell (DAC, High-pressure Diamond Optics) was used, with Nujol as a medium to induce hydrostatic pressure. To calibrate the pressure, a small ruby crystal was added in the measurement cell.[105] Calibration of the system's response was performed with a tungsten lamp.

4.5.5 Experimental Setup for Spectroscopy and Crystallography at High Pressure
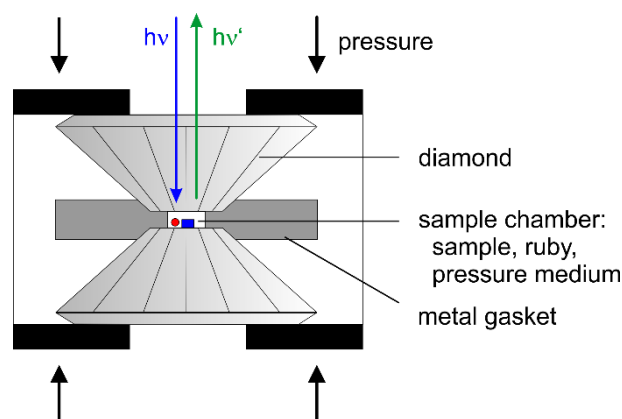
Figure 4-16 Anvil cell for spectroscopy at high pressure.

Spectroscopy at high pressure can be conducted in a so-called anvil cell. This cell consists of two diamonds and a metal gasket as depicted in Figure 4-16. The diamonds are facing each other with the planar polished sides. They clamp a metal plate with a small cylindric hole in the middle that can be seen from the opposite side of the diamond. The cylindric hole forms the sample compartment. It is closed by from each side by diamonds. It is loaded with the sample, a small ruby for measurement of pressure and a pressure medium. The medium is a liquid that fills up the sample chamber and induces hydrostatic pressure. The entire anvil is placed in a sample holder that, upon tightening screws, increases pressure uniformly on the assembly.

Spectroscopic measurements can be conducted through the top and bottom side of the diamond anvils. The incident light can enter from the top ($h\nu$ in Figure 4-16). For most optical measurements like luminescence and Raman spectroscopy, the resulting spectrum is collected on the same side of the anvil ($h\nu'$ in Figure 4-16). For spectroscopic methods, such as X-ray diffraction, the light beam exits the cell on the opposite side of the incident beam and is detected there.

For the determination of the pressure inside the sample compartment, the R_1 line of the ruby is monitored. At ambient pressure this line is at 694.18 nm and shifts red at increased pressure (p). The following calibration was used for pressure determination in crystallographic experiments. The wavelength of the R_1 line (λ) is entered in nm.[106]

$$p = \frac{190.4\text{kbar}}{7.665} \left[\left(\frac{\lambda}{694.18\text{nm}} \right)^{7.665} - 1 \right] \tag{4-2}$$

A similar equation was applied for luminescence and Raman spectroscopy at various pressure, using the wavelength of the ruby R_1 line at ambient pressure (λ_0) and the band shift $\Delta\lambda$:[105]

$$p = 3803 \text{ kbar} \left[\left(\frac{\lambda_0 + \Delta\lambda}{\lambda_0} \right)^5 - 1 \right] \tag{4-3}$$

4.6   Supplementary Tables and Spectra

4.6.1   Raman and Resonance Raman Spectra
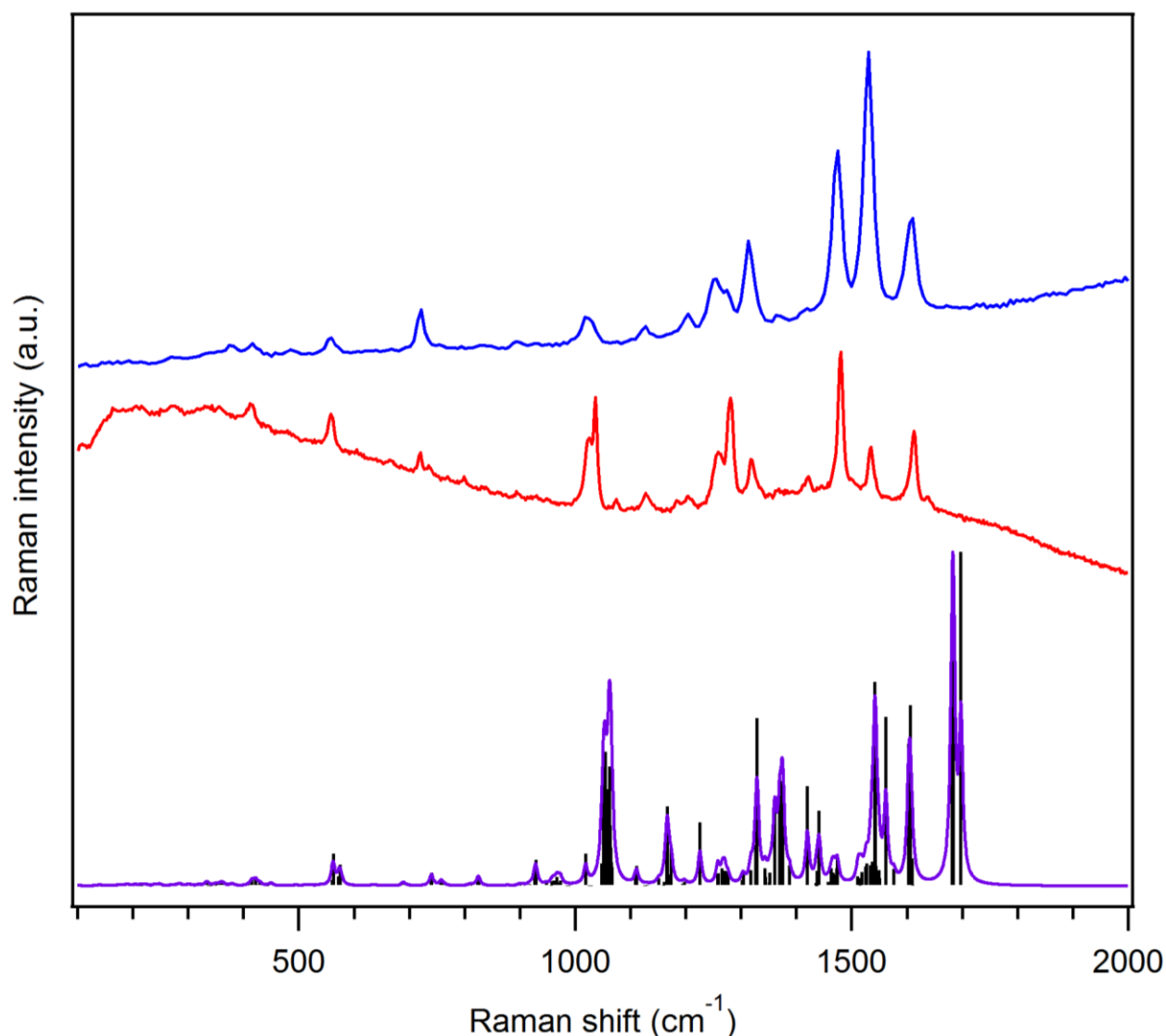
Figure S 4-1 Comparison between the experimental Raman spectra of [Ru(^{t}Bu$_2$-bpy)$_2$biimH$_2$]-(CO$_2$PhSO$_3$) counter ions measured at 293 K with a excitation at 488 nm (top), at 785 nm (middle) and the DFT-calculated spectrum for the cationic complex [Ru(^{t}Bu$_2$-bpy)$_2$biimH$_2$]$^{2+}$ in the gas-phase (bottom, PBE1PBE/Lanl2dz). The vertical black lines represent the calculated frequencies. Their full-width-at-half-maximum was set to 4 cm^{-1} to yield the bottom spectrum. The spectra were normalized and offset along the y-axis for clarity.[90]
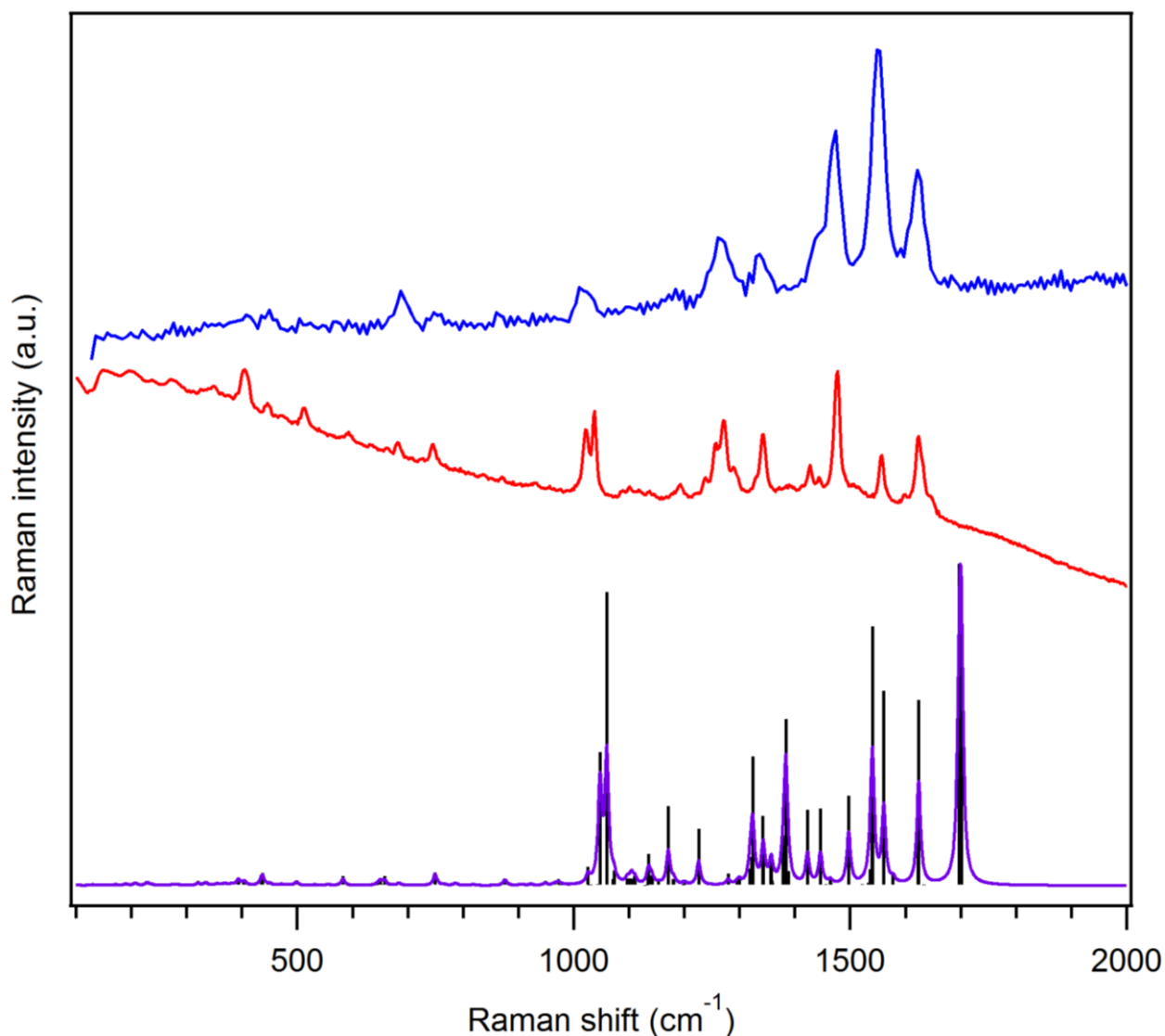
Figure S 4-2 Comparison between the experimental Raman spectra [Ru((CF$_3$)$_2$-bpy)$_2$biimH$_2$]-(CO$_2$PhSO$_3$) counter ions measured at 293 K with excitation at 488 nm (top), at 785 nm (middle) and the DFT-calculated spectrum for the cationic complex [Ru((CF$_3$)$_2$-bpy)$_2$biimH$_2$]$^{2+}$ in the gas-phase (bottom, PBE1PBE/Lanl2dz). The vertical black lines represent the calculated frequencies. Their full-width-at-half-maximum was set to 4 cm^{-1} to yield the bottom spectrum. The spectra were normalized and offset along the y-axis for clarity.[90]

4.6.2   Resonance Raman Spectra at Various Temperature
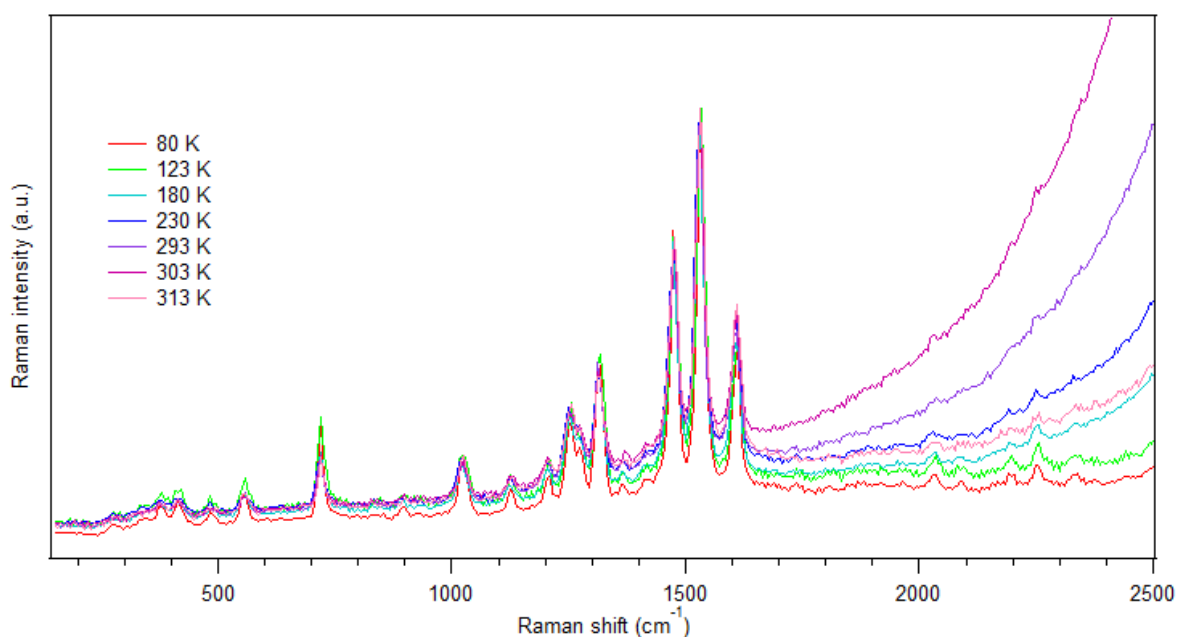
Figure S 4-3 Resonance Raman spectra at variable temperature for [Ru(^{t}Bu$_2$-bpy)$_2$biimH$_2$]-(CO$_2$PhSO$_3$) from 80 K (red) to 313 K (pink). Excitation with a 488 nm laser exalts deformation modes in bipyridine ligands at 1530 cm^{-1}.[90]
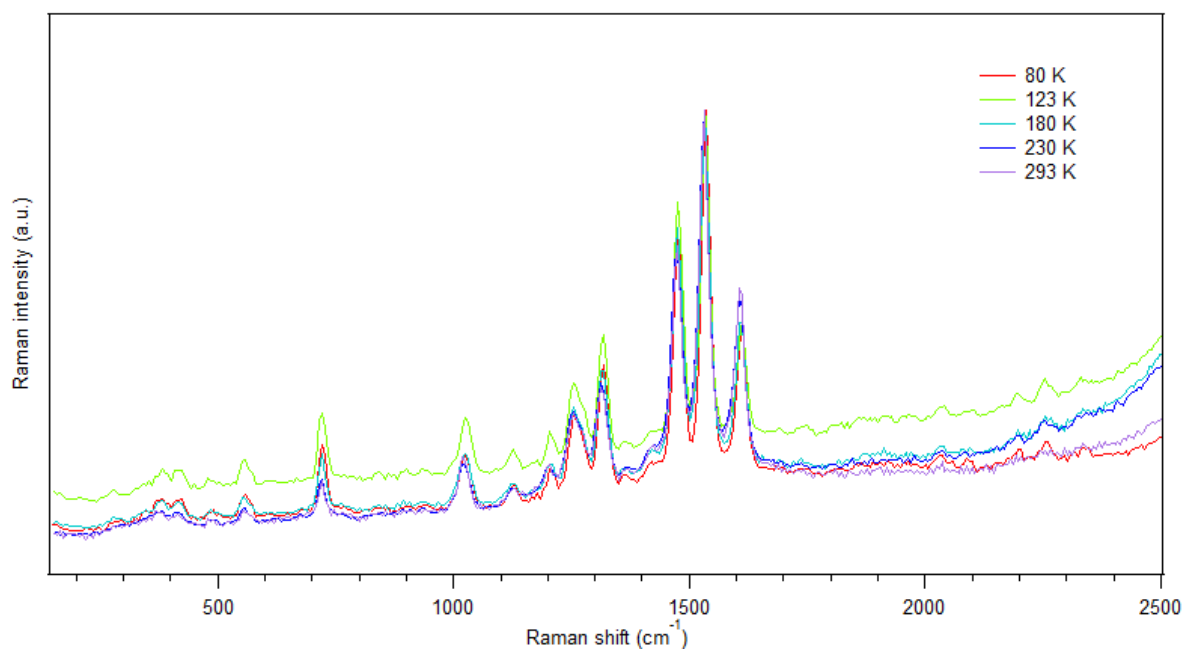
Figure S 4-4 Resonance Raman spectra at variable temperature for [Ru(^{t}Bu$_2$-bpy)$_2$biimH$_2$]Cl$_2$ from 80 K (red) to 293 K (purple). Excitation with a 488 nm laser exalts deformation modes in bipyridine ligands at 1530 cm^{-1}.[90]
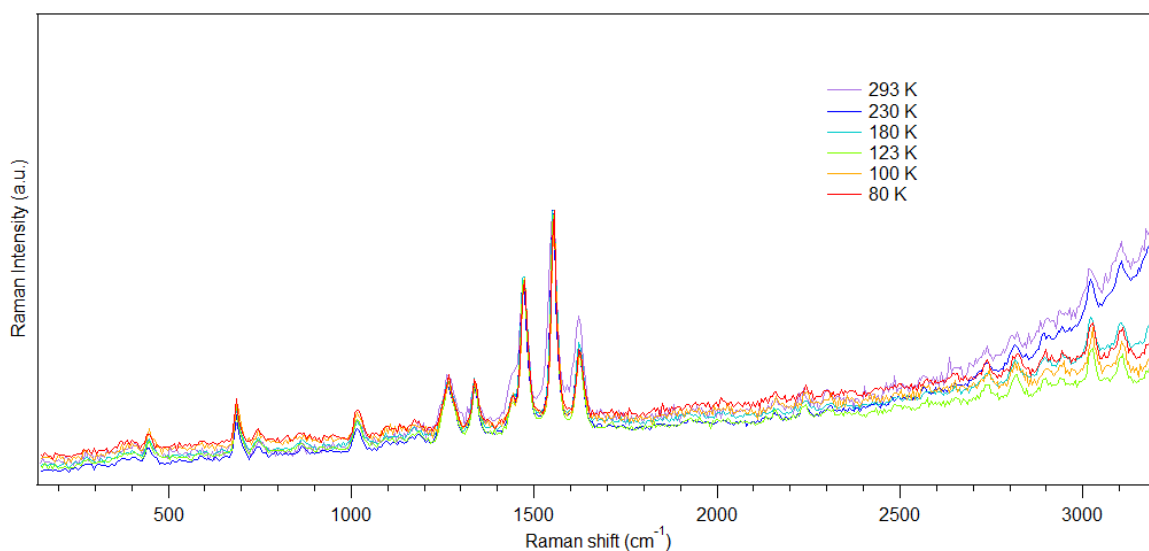
Figure S 4-5 Resonance Raman spectra at variable temperature for $[Ru((CF_3)_2\text{-bpy})_2biimH_2]$-$(CO_2PhSO_3)$ from 80 K (red) to 293 K (purple). Excitation with a 488 nm laser exalts deformation modes in bipyridine ligands at 1530 cm^{-1}.[90]

4.6.3 Raman Spectra at Various Pressure
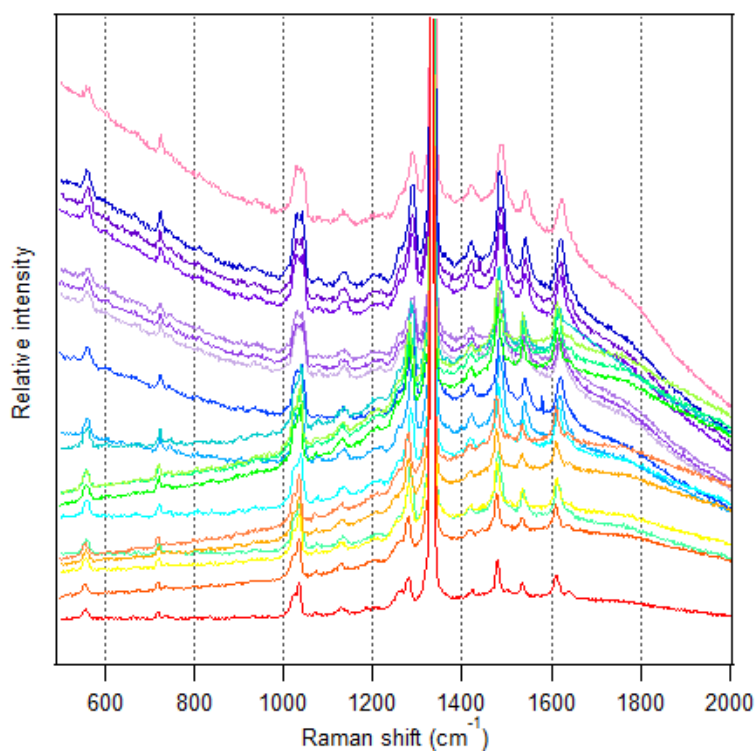
Figure S 4-6 Raman spectra at variable pressure for $[Ru(^tBu_2\text{-bpy})_2biimH_2](CO_2PhSO_3)$ from 4 kbar (red) to 35 kbar (pink).[90]
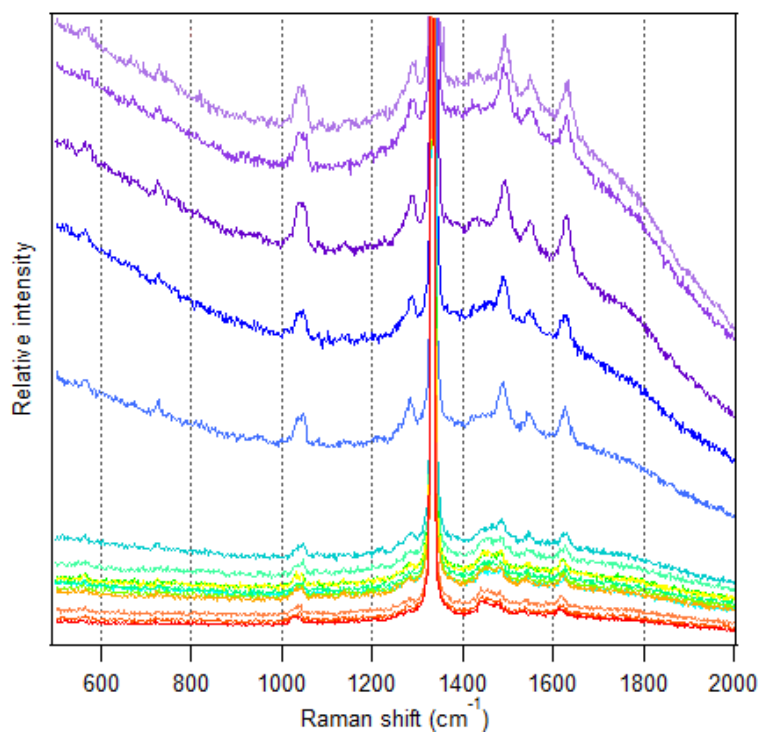
Figure S 4-7 Raman spectra at variable pressure for [Ru(^{t}Bu$_2$-bpy)$_2$biimH$_2$]Cl$_2$ from 0 kbar (red) to 45 kbar (purple).[90]
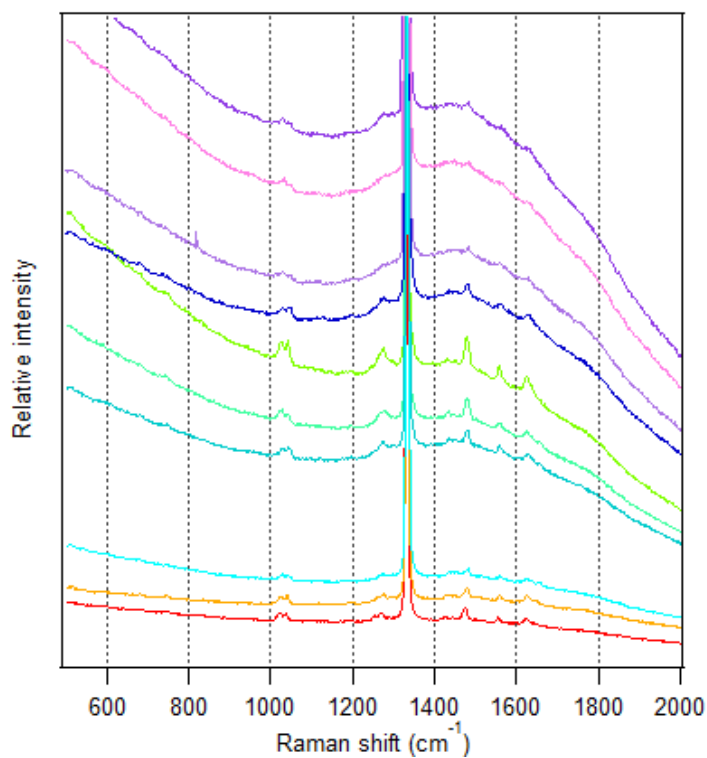
Figure S 4-8 Raman spectra at variable pressure for [Ru((CF$_3$)$_2$-bpy)$_2$biimH$_2$] (CO$_2$PhSO$_3$) from 6 kbar (red) to 44 kbar (pink).[90]

4.6.4   NMR
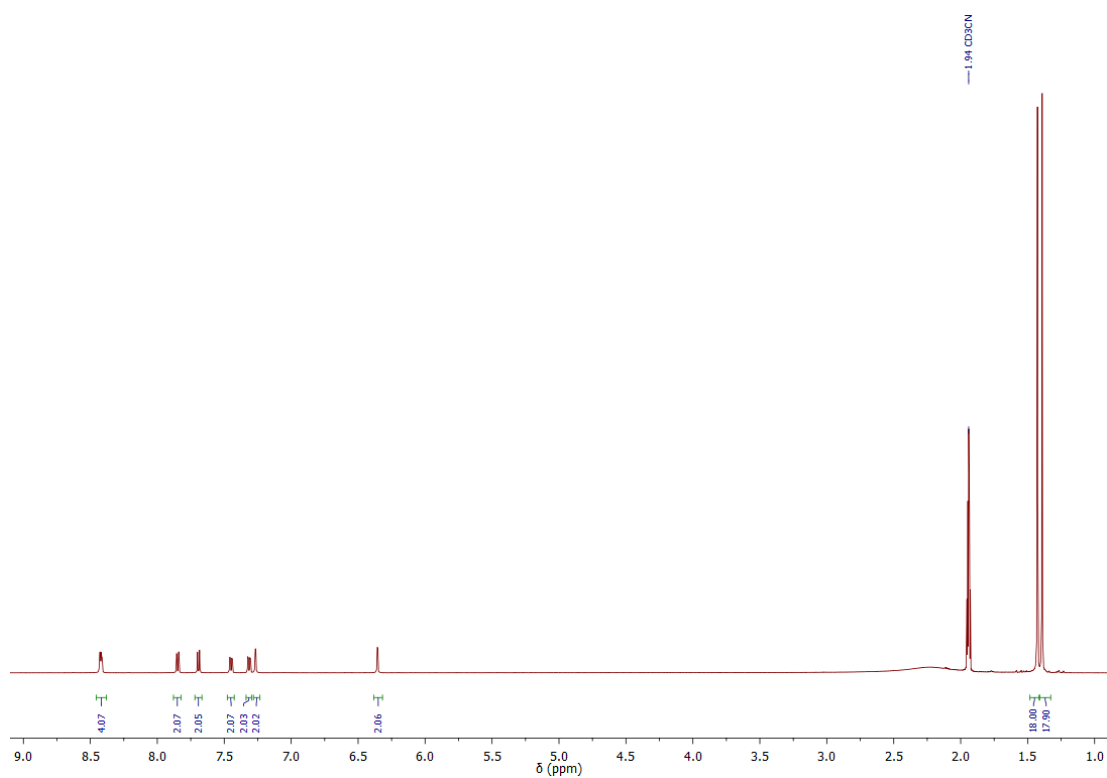
Figure S 4-9 ^{1}H NMR spectrum of [Ru(^{t}Bu$_2$-bpy)$_2$biimH$_2$]Cl$_2$ in CD$_3$CN.
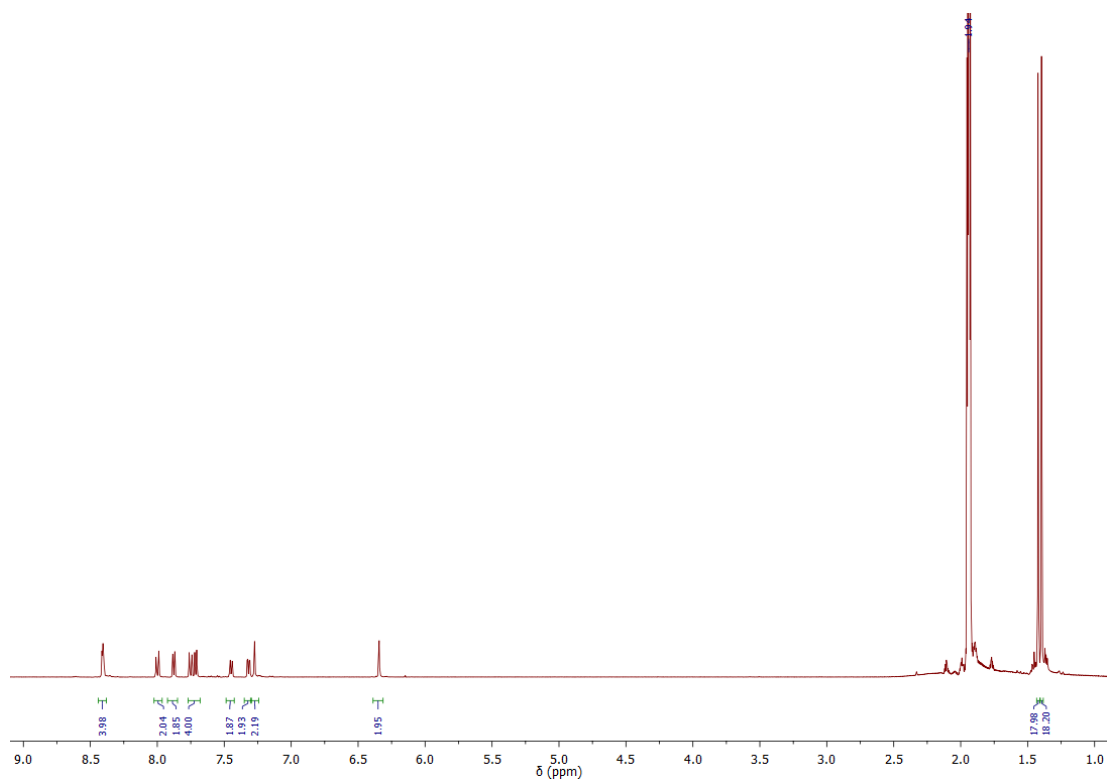
Figure S 4-10 ^{1}H NMR spectrum of [Ru(^{t}Bu$_2$-bpy)$_2$biimH$_2$](CO$_2$PhSO$_3$) in CD$_3$CN.
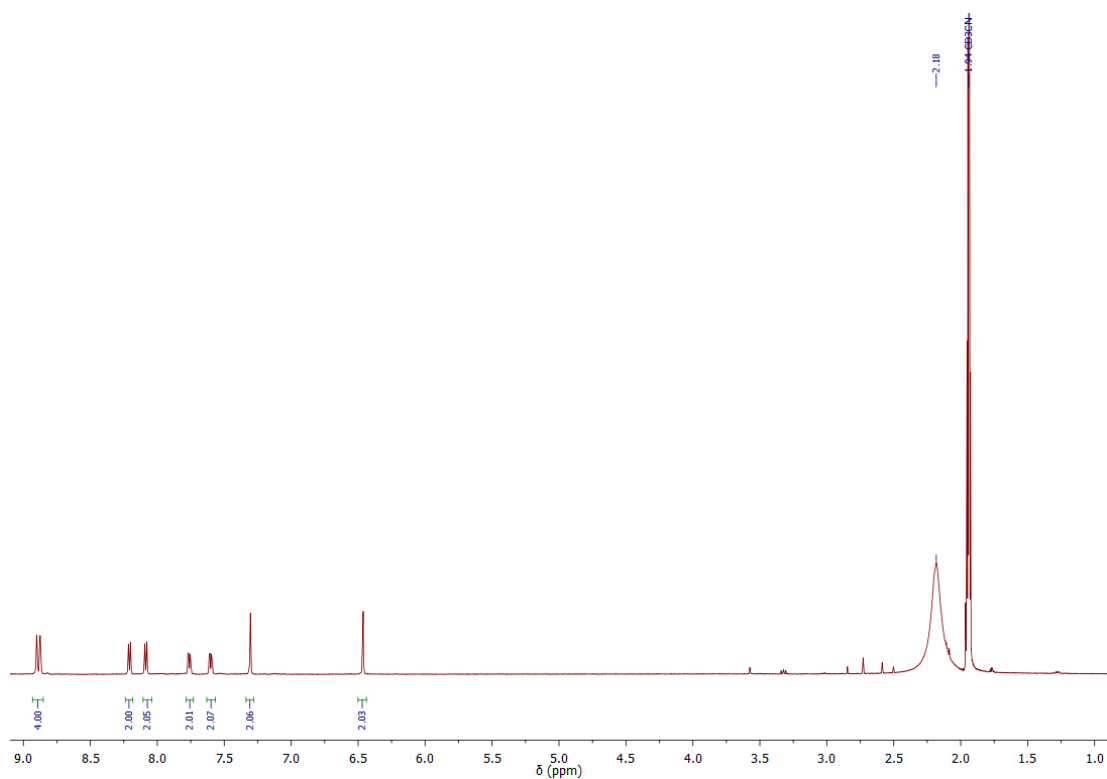
Figure S 4-11 ^{1}H NMR spectrum of [Ru((CF$_3$)$_2$-bpy)$_2$biimH$_2$]Cl$_2$ in CD$_3$CN.
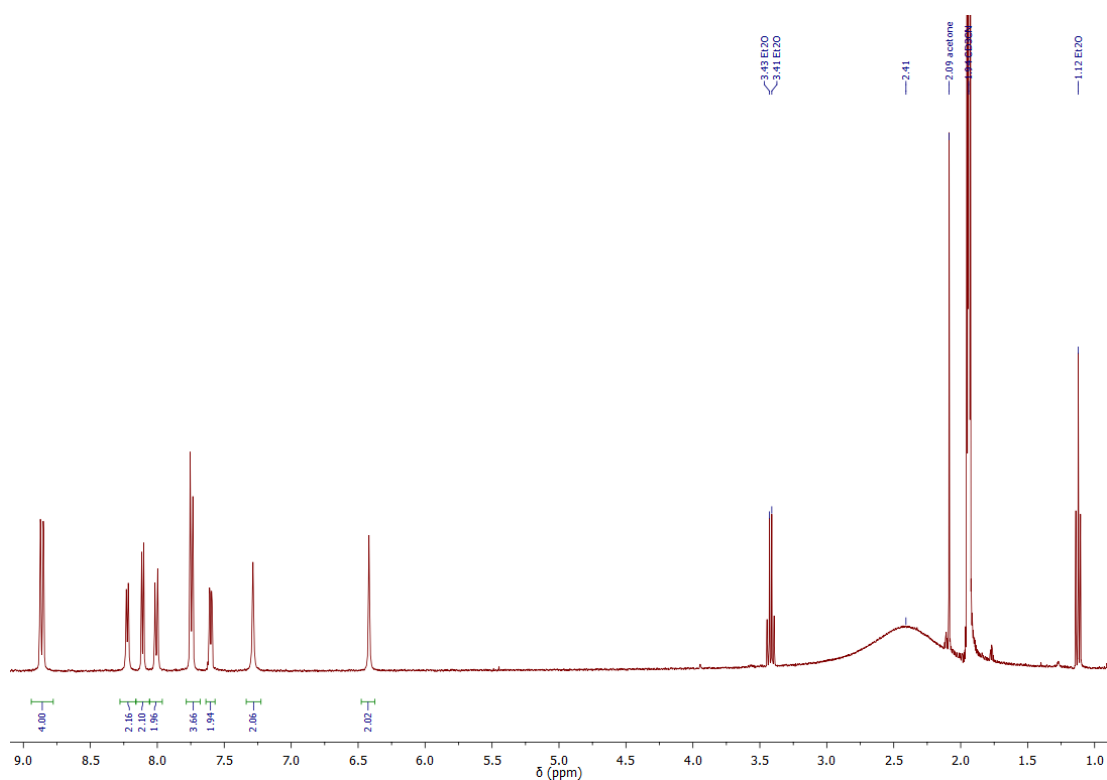
Figure S 4-12 ^{1}H NMR spectrum of [Ru((CF$_3$)$_2$-bpy)$_2$biimH$_2$](CO$_2$PhSO$_3$) in CD$_3$CN.

5 References

[1]   OECD, *OECD Environmental Outlook to 2050: The Consequences of Inaction*, OECD Publishing, **2012**.

[2]   United-Nations, "United Nations Framework on Climate Change," can be found under http://unfccc.int/resource/climateaction2020/index.html, **1997**.

[3]   "2000-Watt-Gesellschaft," can be found under http://www.2000watt.ch/, **2017**.

[4]   Bundesregierung Deutschland, "Bundesregierung - Energiewende," can be found under https://www.bundesregierung.de/Webs/Breg/DE/Themen/Energiewende/_node.html, **2016**.

[5]   D. Gust, T. A. Moore, A. L. Moore, *Acc. Chem. Res.* **2009**, *42*, 1890–1898.

[6]   N. S. Lewis, D. G. Nocera, *Proc. Natl. Acad. Sci. U. S. A.* **2006**, *103*, 15729–15735.

[7]   R. E. Blankenship, *Molecular Mechanisms of Photosynthesis*, Wiley Blackwell, **2014**.

[8]   N. Nelson, C. F. Yocum, *Annu. Rev. Plant Biol.* **2006**, *57*, 521–565.

[9]   B. Kok, B. Forbush, M. McGlion, *Photochem. Photobiol.* **1970**, *11*, 457–475.

[10]   J. J. Warren, T. A. Tronic, J. M. Mayer, *Chem. Rev.* **2010**, *110*, 6961–7001.

[11]   J. M. Mayer, D. A. Hrovat, J. L. Thomas, W. T. Borden, *J. Am. Chem. Soc.* **2002**, *124*, 11142–11147.

[12]   E. S. Wiedner, M. B. Chambers, C. L. Pitman, R. M. Bullock, A. J. M. Miller, A. M. Appel, *Chem. Rev.* **2016**, *116*, 8655–8692.

[13]   A. Weller, *Zeitschrift für Phys. Chemie* **1982**, *133*, 93–98.

[14]   B. D. McCarthy, J. L. Dempsey, *Inorg. Chem.* **2017**, *45*, 1225–1231.

[15]   E. C. Gentry, R. R. Knowles, *Acc. Chem. Res.* **2016**, *49*, 1546–1556.

[16]   P. Gilli, L. Pretto, V. Bertolasi, G. Gilli, *Acc. Chem. Res.* **2009**, *42*, 33–44.

[17]   M. Sjödin, T. Irebo, J. E. Utas, J. Lind, G. Merényi, B. Åkermark, L. Hammarström, *J. Am. Chem. Soc.* **2006**, *128*, 13076–13083.

[18]   E. R. Young, J. Rosenthal, J. M. Hodgkiss, D. G. Nocera, *J. Am. Chem. Soc.* **2009**, *131*, 7678–7684.

[19]   J. Nomrowski, O. S. Wenger, *Inorg. Chem.* **2015**, *54*, 3680–3687.

[20]   L. A. Clare, A. T. Pham, F. Magdaleno, J. Acosta, J. E. Woods, A. L. Cooksy, D. K. Smith, *J. Am. Chem. Soc.* **2013**, *135*, 18930–18941.

[21]   H. Yersin, W. Humbs, J. Strasser, *Top. Curr. Chem.* **1997**, *191*, 153–249.

[22]   L. M. Tolbert, K. M. Solntsev, *Acc. Chem. Res.* **2002**, *35*, 19–27.

[23]   Z. R. Grabowski, W. Rubaszewska, *J. Chem. Soc. Faraday Trans. 1 Phys. Chem.*

Condens. Phases **1977**, *73*, 11–28.

[24]   T. T. Eisenhart, J. L. Dempsey, *J. Am. Chem. Soc.* **2014**, *136*, 12221–12224.

[25]   M. J. Field, S. Sinha, J. J. Warren, *Phys. Chem. Chem. Phys.* **2016**, *18*, 30907–30911.

[26]   L. Hammarström, S. Styring, *Energy Environ. Sci.* **2011**, *4*, 2379–2388.

[27]   D. L. Jenson, B. A. Barry, *J. Am. Chem. Soc.* **2009**, *131*, 10567–10573.

[28]   Y. Umena, K. Kawakami, J.-R. Shen, N. Kamiya, *Nature* **2011**, *473*, 55–60.

[29]   M. R. Wasielewski, *Acc. Chem. Res.* **2009**, *42*, 1910–1921.

[30]   A. A. Pizano, J. L. Yang, D. G. Nocera, *Chem. Sci.* **2012**, *3*, 2457–2461.

[31]   S. D. Glover, C. Jorge, L. Liang, K. G. Valentine, L. Hammarström, C. Tommos, *J. Am. Chem. Soc.* **2014**, *136*, 14039–51.

[32]   C. Bronner, O. S. Wenger, *Phys. Chem. Chem. Phys.* **2014**, *16*, 3617–3622.

[33]   J. D. Megiatto, D. D. Méndez-Hernández, M. E. Tejeda-Ferrari, A.-L. Teillout, M. J. Llansola-Portolés, G. Kodis, O. G. Poluektov, T. Rajh, V. Mujica, T. L. Groy, et al., *Nat. Chem.* **2014**, *6*, 423–8.

[34]   M. Kuss-Petermann, O. S. Wenger, *J. Phys. Chem. A* **2013**, *117*, 5726–5733.

[35]   J. Chen, M. Kuss-Petermann, O. S. Wenger, *J. Phys. Chem. B* **2015**, *119*, 2263−2273.

[36]   J. Chen, M. Kuss-Petermann, O. S. Wenger, *Chem. Eur. J.* **2014**, *20*, 4098–4104.

[37]   P. Dongare, S. Maji, L. Hammarström, *J. Am. Chem. Soc.* **2016**, *138*, 2194–2199.

[38]   G. F. Manbeck, E. Fujita, J. J. Concepcion, *J. Am. Chem. Soc.* **2016**, *138*, 11536–11549.

[39]   M. Kuss-Petermann, O. S. Wenger, *Angew. Chem., Int. Ed.* **2016**, *55*, 815–819.

[40]   G. A. Parada, T. F. Markle, S. D. Glover, L. Hammarström, S. Ott, B. Zietz, *Chem. Eur. J.* **2015**, *21*, 6362–6366.

[41]   G. F. Moore, M. Hambourger, M. Gervaldo, O. G. Poluektov, T. Rajh, D. Gust, T. A. Moore, A. L. Moore, *J. Am. Chem. Soc.* **2008**, *130*, 10466–10467.

[42]   W. Herzog, C. Bronner, S. Löffler, B. He, D. Kratzert, D. Stalke, A. Hauser, O. S. Wenger, *ChemPhysChem* **2013**, *14*, 1168–1176.

[43]   T. F. Markle, I. J. Rhile, J. M. Mayer, *J. Am. Chem. Soc.* **2011**, *133*, 17341–17352.

[44]   C. Costentin, M. Robert, J.-M. Savéant, C. Tard, *Phys. Chem. Chem. Phys.* **2011**, *13*, 5353–5358.

[45]   J. N. Schrauben, M. Cattaneo, T. C. Day, A. L. Tenderholt, J. M. Mayer, *J. Am. Chem. Soc.* **2012**, *134*, 16635–16645.

[46]   P. S. Braterman, J. I. Song, *J. Org. Chem.* **1991**, *56*, 4678–4682.

[47]   A. Harriman, G. R. Millward, P. Neta, M. C. Richoux, J. M. Thomas, *J. Phys. Chem.* **1988**, *92*, 1286–1290.

[48]   A. Pannwitz, O. S. Wenger, *Phys. Chem. Chem. Phys.* **2016**, *18*, 11374–11382.

[49]   V. W. Manner, T. F. Markle, J. H. Freudenthal, J. P. Roth, J. M. Mayer, *Chem. Comm.* **2008**, *246*, 256–258.

[50]   P. K. Das, M. V. Encinas, S. Steenken, J. C. Scaiano, *J. Am. Chem. Soc.* **1981**, *103*, 4162–4166.

[51]   R. Lomoth, T. Häupl, O. Johansson, L. Hammarström, *Chem. Eur. J.* **2002**, *8*, 102–110.

[52]   J. D. Henrich, H. Y. Zhang, P. K. Dutta, B. Kohler, *J. Phys. Chem. B* **2010**, *114*, 14679–14688.

[53]   E. H. Yonemoto, G. B. Saupe, R. H. Schmehl, S. M. Hubig, R. L. Riley, B. L. Iverson, T. E. Mallouk, *J. Am. Chem. Soc.* **1994**, *116*, 4786–4795.

[54]   L. A. Kelly, M. A. J. Rodgers, *J. Phys. Chem.* **1995**, *99*, 13132–13140.

[55]   S. L. Mecklenburg, B. M. Peek, J. R. Schoonover, D. G. McCafferty, C. G. Wall, B. W. Erickson, T. J. Meyer, *J. Am. Chem. Soc.* **1993**, *115*, 5479–5495.

[56]   J. Hankache, O. S. Wenger, *Chem. Comm.* **2011**, *47*, 10145–10147.

[57]   D. M. Roundhill, *Photochemistry and Photophysics of Metal Complexes*, Plenum Press, New York, **1994**.

[58]   W. J. Park, Y. Kim, C. Lee, *Bull. Korean Chem. Soc.* **1994**, *15*, 896–900.

[59]   M. Kuss-Petermann, O. S. Wenger, *J. Phys. Chem. Lett.* **2013**, *4*, 2535–2539.

[60]   W. M. Haynes, T. J. Bruno, D. R. Lide, *Handbook of Chemistry and Physics*, CRC Press, Taylor & Francis Group, Boca Raton London New York, **2015**.

[61]   M. Kuss-Petermann, H. Wolf, D. Stalke, O. S. Wenger, *J. Am. Chem. Soc.* **2012**, *134*, 12844–12854.

[62]   S.-J. Liu, Q. Zhao, R.-F. Chen, Y. Deng, Q.-L. Fan, F.-Y. Li, L.-H. Wang, C.-H. Huang, W. Huang, *Chem. Eur. J.* **2006**, *12*, 4351–4361.

[63]   B. P. Sullivan, D. J. Salmon, T. J. Meyer, *Inorg. Chem.* **1978**, *17*, 3334–3341.

[64]   S. Y. Reece, D. G. Nocera, *Annu. Rev. Biochem.* **2009**, *78*, 673–699.

[65]   S. Sahu, L. R. Widger, M. G. Quesne, S. P. de Visser, H. Matsumura, P. Moënne-Loccoz, M. A. Siegler, D. P. Goldberg, *J. Am. Chem. Soc.* **2013**, *135*, 10590–10593.

[66]   S. A. Cook, A. S. Borovik, *Acc. Chem. Res.* **2015**, *48*, 2407–2414.

[67]   G.-J. Zhao, K.-L. Han, *Acc. Chem. Res.* **2012**, *45*, 404–413.

[68]   J. C. Freys, G. Bernardinelli, O. S. Wenger, *Chem. Comm.* **2008**, 4267–4269.

[69]   S. Derossi, H. Adams, M. D. Ward, *Dalton Trans.* **2007**, 33–36.

[70]   S. Poirier, R. J. Roberts, D. Le, D. B. Leznoff, C. Reber, *Inorg. Chem.* **2015**, *54*, 3728–3735.

[71] S. Poirier, L. Czympiel, N. Bélanger-Desmarais, S. Mathur, C. Reber, *Dalton Trans.* **2016**, *45*, 6574–6581.

[72] S. Poirier, E. Tailleur, H. Lynn, C. Reber, *Dalton Trans.* **2016**, *45*, 10883–10886.

[73] H. Yersin, E. Gallhuber, *Inorg. Chem.* **1984**, *23*, 3745–3748.

[74] Q. Sun, S. Mosquera-Vazquez, Y. Suffren, J. Hankache, N. Amstutz, L. M. Lawson Daku, E. Vauthey, A. Hauser, *Coord. Chem. Rev.* **2015**, *282–283*, 87–99.

[75] S. A. Rommel, D. Sorsche, S. Rau, *Dalton Trans.* **2016**, *45*, 74–77.

[76] M. Biner, H. B. Buergi, A. Ludi, C. Roehr, *J. Am. Chem. Soc.* **1992**, *114*, 5197–5203.

[77] M. A. M. Lorente, F. Dahan, V. Petrouleas, A. Bousseksou, J.-P. Tuchagues, *Inorg. Chem.* **1995**, *34*, 5346–5357.

[78] B.-H. Ye, F. Xue, G.-Q. Xue, L.-N. Ji, T. C. . Mak, *Polyhedron* **1999**, *18*, 1785–1790.

[79] B. H. Ye, B. B. Ding, Y. Q. Weng, X. M. Chen, *Inorg. Chem.* **2004**, *43*, 6866–6868.

[80] **n.d.**, DOI 10.5517/ccvfcxj.

[81] C. Adamo, V. Barone, *J. Chem. Phys.* **1999**, *110*, 6158–6170.

[82] P. J. Hay, W. R. Wadt, *J. Chem. Phys.* **1985**, *82*, 299–310.

[83] K. M. Lancaster, J. B. Gerken, A. C. Durrell, J. H. Palmer, H. B. Gray, *Coord. Chem. Rev.* **2010**, *254*, 1803–1811.

[84] M. Buchs, C. Daul, *CHIMIA* **1998**, *52*, 163–166.

[85] M.-A. Haga, *Inorg. Chim. Acta* **1983**, *75*, 29–35.

[86] M. Haga, M. M. Ali, S. Koseki, K. Fujimoto, A. Yoshimura, K. Nozaki, T. Ohno, K. Nakajima, D. J. Stufkens, *Inorg. Chem.* **1996**, *35*, 3335–3347.

[87] A. Juris, V. Balzani, F. Barigelletti, S. Campagna, P. Belser, A. von Zelewsky, *Coord. Chem. Rev.* **1988**, *84*, 85–277.

[88] Y. Cui, H. J. Mo, J. C. Chen, Y. L. Niu, Y. R. Zhong, K. C. Zheng, B. H. Ye, *Inorg. Chem.* **2007**, *46*, 6427–6436.

[89] J. C. Freys, O. S. Wenger, *Eur. J. Inorg. Chem.* **2010**, *2*, 5509–5516.

[90] S. Poirier, N. Bélanger-Desmarais, **2017**.

[91] M. L. Myrick, M. K. De Armond, R. L. Blakley, *Inorg. Chem.* **1989**, *28*, 4077–4084.

[92] C. V Kumar, J. K. Barton, I. R. Gould, N. J. Turro, J. Van Houten, *Inorg. Chem.* **1988**, *27*, 648–651.

[93] D. P. Rillema, R. Sahai, P. Matthews, A. K. Edwards, R. J. Shaver, L. Morgan, *Inorg. Chem.* **1990**, *29*, 167–175.

[94] A. Pannwitz, A. Prescimone, O. S. Wenger, *Eur. J. Inorg. Chem.* **2017**, *2017*, 609–615.

[95] E. A. Braude, F. C. Nachod, *Determination of Organic Structures by Physical Methods*,

Academic Press, New York, **1955**.

[96] S. A. Moggach, S. Parsons, P. A. Wood, *Crystallogr. Rev.* **2008**, *14*, 143–184.

[97] D. M. S. Martins, D. S. Middlemiss, C. R. Pulham, C. C. Wilson, M. T. Weller, P. F. Henry, N. Shankland, K. Shankland, W. G. Marshall, R. M. Ibberson, et al., *J. Am. Chem. Soc.* **2009**, *131*, 3884–3893.

[98] R. Hönes, M. Kuss-Petermann, O. S. Wenger, *Photochem. Photobiol. Sci.* **2013**, *12*, 254–261.

[99] T. Ben Hadda, H. Le Bozec, *Polyhedron* **1988**, *7*, 575–577.

[100] L. Palatinus, G. Chapuis, *J. Appl. Crystallogr.* **2007**, *40*, 786–790.

[101] P. W. Betteridge, J. R. Carruthers, R. I. Cooper, K. Prout, D. J. Watkin, *J. Appl. Crystallogr.* **2003**, *36*, 1487–1487.

[102] A. L. Spek, *Acta Crystallogr. Sect. C Struct. Chem.* **2015**, *71*, 9–18.

[103] C. F. Macrae, I. J. Bruno, J. A. Chisholm, P. R. Edgington, P. McCabe, E. Pidcock, L. Rodriguez-Monge, R. Taylor, J. Van De Streek, P. A. Wood, *J. Appl. Crystallogr.* **2008**, *41*, 466–470.

[104] M. J. Frisch, G. W. Trucks, H. B. Schlegel, G. E. Scuseria, M. A. Robb, J. R. Cheeseman, G. Scalmani, V. Barone, B. Mennucci, G. A. Petersson, et al., **2009**.

[105] H. K. Mao, P. M. Bell, J. W. Shaner, D. J. Steinberg, *J. Appl. Phys.* **1978**, *49*, 3276–3283.

[106] H. K. Mao, J. Xu, P. M. Bell, *J. Geophys. Res.* **1986**, *91*, 4673–4676.

Abbreviations

BDE	bond dissociation enthalpy
BDFE	bond dissociation free energy
biimH$_2$	2,2'-biimidazole
bpy	2,2'-bipyridine
ET	electron transfer
eq.	equation
FWHM	full width at half maximum
HAT	hydrogen atom transfer
HOMO	highest occupied orbital
LLCT	ligand to ligand charge transfer
LUMO	lowest unoccupied orbital
MLCT	metal to ligand charge transfer
MO	molecular orbital
MQ$^+$	monoquat (N-methyl-4,4'-bipyridinium)
MV^{2+}	methyl viologen (N,N'-dimethyl-4,4'-bipyridinium)
NO$_x$	nitrogen oxides
PC	plastocyanine
PCET	proton-coupled electron transfer
Pheo a	pheophytin a
PhOH	phenol
PS I	photosystem I
PS II	photosystem II
pyimH	2-(2'-pyridyl)imidazole
QA	Plastoquinone A
QB	Plastoquinone B
TBAOH	tetrabutylammonium hydroxide
xy	xylene

Acknowledgements

And finally, I want to thank my family and friends. Some of you were involved with my work in the last years and I acknowledge you for motivation, education, technical support, synthesis approval, and bananas. But most importantly, I am grateful that you are my family and friends and I want to thank you for all joint activities such as climbing, cycling, running, hiking, board games, travelling, movies, home brewing, discussions, poetry, music, cooking and eating together.

CURRICULUM VITAE

PERSONAL INFORMATION

Name: Andrea Pannwitz

Birth: March 17, 1989 in Jena, Germany

ORCID: 0000-0001-9633-0730

EDUCATION

06/2013 – present   PhD candidate in the Group of Prof. Dr. Oliver S. Wenger, Chemistry Department University of Basel (CH)

11/2012 – 05/2013   Master thesis in Inorganic Chemistry at Georg-August-University Göttingen (D) in the group of Prof. Dr. Franc Meyer:

„Immobilisierung von Ruthenium-basierten Katalysatoren zur Wasseroxidation auf oxidischen Oberflächen" („Immobilization of Ruthenium Based Water Oxidation Catalysts on Oxide Surfaces")

09/2010 – 05/2013   Master studies in Chemistry, Georg-August-University Göttingen (D), (M.Sc.)

02 – 07/2011   ERASMUS semester: master studies in environmental sciences, University of Geneva (CH)

10/2007 – 09/2010   Bachelor studies in chemistry, Georg-August-University Göttingen (D), (B.Sc.)

07/1999 – 05/2007   Carl-Zeiss-Gymnasium Jena (D), (Abitur)

Languages: German (native), English (fluent), French (advanced), Russian (basics), Swiss-German (good understanding)

AWARDS AND FELLOWSHIPS

01/2016   Best Talk: Swiss Snow Symposium, Saas-Fee (CH)

12/2015   Poster Prize: Basel Chemistry Christmas Symposium 2015 (CH)

02 – 07/2011   ERASMUS fellowship for one semester in master studies in environmental sciences at University of Geneva (CH)

OTHER CONTRIBUTIONS TO SCIENCE

02/2014 – 07/2016 Active member of the organization board of the PhD Chemistry Community (PCC) Basel (CH), organization of research seminars, symposia and networking events at the University of Basel

09/2011 Co-organization of the student's conference „Summer School on Green Chemistry" in Göttingen (D)

PUBLICATIONS IN PEER-REVIEWED SCIENTIFIC JOURNALS

[4] J. Odrobina, J. Scholz, A. Pannwitz, L. Francàs, S. Dechert, A. Llobet, C. Jooss, F. Meyer *"Backbone Immobilization of the Bis(bipyridyl)pyrazolate Diruthenium Catalyst for Electrochemical Water Oxidation"*, *ACS Catalysis* **2017**, *7,* 2116-2125. (DOI: 10.1021/acscatal.6b02860)

[3] A. Pannwitz, A. Prescimone, O. S. Wenger, *"Ruthenium(II)–Pyridylimidazole Complexes as Photoreductants and PCET Reagents"*, *European Journal of Inorganic Chemistry* **2017**, *2017*, 609–615. (DOI: 10.1002/ejic.201601403)

[2] S. G. Keller, A. Pannwitz, F. Schwizer, J. Klehr, O. S. Wenger, T. R. Ward, „*Light-driven electron injection from a biotinylated triarylamine donor to* $[Ru(diimine)_3]^{2+}$*-labeled streptavidin*", *Organic and Biomolecular Chemistry* **2016**, *14*, 7197–7201. (DOI: 10.1039/C6OB01273F)

[1] A. Pannwitz, O. S. Wenger, „*Proton coupled electron transfer from the excited state of a ruthenium(II) pyridylimidazole complex*", *Physical Chemistry Chemical Physics* **2016**, *18*, 11374–11382. (DOI: 10.1039/C6CP00437G)

OTHER PUBLICATIONS

[b] A. Pannwitz, S. Rigo, L. Bannwart, L. Bizzini, S. Malzkuhn, T. Müntener, C. Laupheimer, *"Basel Chemistry Christmas Symposium 2015"*, *CHIMIA*, **2016**, *70*, 295–295. (DOI: 10.2533/chimia.2016.295)

[a] C. Daeppen, D. Bachmann, A. Pannwitz, I. Kerschgens, C. Laupheimer, M. Rother, L. Jundt, M. Rickhaus, M. Gantenbein, I. Bodoky, *"Basel Chemistry Symposium 2014 In Memory of Prof. T. Reichstein"* *CHIMIA*, **2015**, *69*, 63–64. (DOI: 10.2533/chimia.2015.63)

ORAL CONTRIBUTIONS TO CONFERENCES

11/2016   Research Seminar of the PhD Chemistry Community (PCC), University of Basel (CH), „*Electrons - catch them if you can! - How to trap a long lived charge separated state*"

09/2016   6th EuCheMS Chemistry Congress, Sevilla (ES),
„*Light Energy Conversion - Excited State Proton-Coupled Electron Transfer (PCET) as Promising Pathway*"

02/2016   Inorganic Chemistry Research Seminar, University of Montreal (CA),
„*Light Driven Hydrogen Atom Release from a Ruthenium Complex*"

01/2016   Swiss Snow Symposium, Saas Fee (CH),
„*Light Driven Hydrogen Atom Release from a Ruthenium Complex*"

03/2014   COST Action CM1202 Training School: Young Researcher Meeting on Current Challenges in Supramolecular Artificial Photosynthesis, Jena (D),
„*Light Induced Long Range Electron Transfer Coupled to Two Proton Transfers*"

POSTER CONTRIBUTIONS TO CONFERENCES

01/2017   26th Winter I-APS Conference, Sarasota, Florida (USA) "*Double-PCET in a Molecular Triad*"

07/2016   42nd International Conference on Coordination Chemistry 2016 (ICCC), Brest (F)
„*Light Driven Hydrogen Atom Release from a Ruthenium Complex*"

04/2015   1st International Solar Fuels Conference (ISF-1), Uppsala, Sweden 2015 „*Strong Excited State H-Atom Donors via Unidirectional PCET*"

09/2014   SCS Fall Meeting 2014, Zürich (CH) „*Light-Induced Long-Range Electron Transfer Coupled to Two Proton Transfers*"

07/2014   XXV IUPAC Symposium on Photochemistry 2014, Bordeaux, (F)
„*Light-Induced Long-Range Electron Transfer Coupled to Two Proton Transfers*"

03/2014   COST Action CM1202 Meeting: Current Challenges in Supramolecular Artificial Photosynthesis, Jena (D) „*Light Induced Long Range Electron Transfer Coupled to Two Proton Transfers*"